

Spin-2 Resonances in Vector Boson Fusion Processes at the LHC

Diplomarbeit von
Jessica Frank

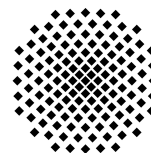
07. März 2011

Hauptberichter: Prof. Dr. D. Zeppenfeld
(Karlsruhe Institute of Technology)

Mitberichter: Prof. Dr. G. Wunner
(Universität Stuttgart)



Institut für Theoretische Physik
Karlsruhe Institute of Technology



1. Institut für Theoretische Physik
Universität Stuttgart

Ehrenwörtliche Erklärung

Ich versichere, dass ich diese Arbeit selbstständig verfasst und keine anderen als die angegebenen Quellen und Hilfsmittel benutzt habe.

Jessica Frank
Karlsruhe, den 07. März 2011

Contents

1	Introduction	7
2	Theoretical background	9
2.1	The Standard Model of Elementary Particle Physics	9
2.1.1	Gauge groups and interactions	9
2.1.2	Spontaneous symmetry breaking: The Higgs mechanism	11
2.2	Calculating Feynman Rules from a given Lagrangian	14
2.3	Effective field theories	16
2.3.1	Example: The Fermi theory	17
3	Lagrangian and Feynman Rules for the interaction of a Spin-2 particle with electroweak bosons	19
3.1	Spin-2 singlet	19
3.1.1	Lagrangian	19
3.1.2	Feynman Rules	21
3.2	Spin-2 triplet	23
3.2.1	Lagrangian	23
3.2.2	Feynman Rules	24
4	Implementation into VBFNLO	27
4.1	Vector Boson Fusion and the program VBFNLO	27
4.2	Overview of the implementation of the Spin-2 model into VBFNLO	31
4.3	New HELAS routines and extension of the leptonic tensors	31
4.4	The different processes: New Feynman diagrams and implementation	34
4.4.1	200: $VV \rightarrow e^+ \nu_e \mu^- \bar{\nu}_\mu$	35
4.4.2	210: $VV \rightarrow e^+ e^- \mu^+ \mu^-$	36
4.4.3	211: $VV \rightarrow e^+ e^- \nu_\mu \bar{\nu}_\mu$	37
4.4.4	220: $VV \rightarrow e^+ \nu_e \mu^+ \mu^-$	38
4.4.5	230: $VV \rightarrow e^- \bar{\nu}_e \mu^+ \mu^-$	39
4.4.6	240: $VV \rightarrow \gamma\gamma$	39
4.5	Input parameters and selection cuts	41
4.5.1	Input parameters	41
4.5.2	Selection cuts	42
5	Results	45
5.1	Unitarity violation and formfactor in longitudinal WW scattering	45

5.2	Photon pair-production in Vector Boson Fusion via Higgs and Spin-2 resonances	51
5.2.1	Cross sections	53
5.2.2	p_T distributions and formfactor	55
5.2.3	Resonance peak, width and branching ratio	58
5.2.4	Angular distributions	59
5.2.5	Summary of photon pair-production in VBF via Higgs and Spin-2 resonances	71
5.3	Heavy Spin-2 resonances in four-charged-lepton production via the VBF process $pp \rightarrow VV jj \rightarrow e^+ e^- \mu^+ \mu^- jj$	72
5.3.1	Cross sections	73
5.3.2	Invariant mass distribution of the four final state leptons	74
5.3.3	Transverse momentum and angular distributions	76
5.4	Heavy Spin-2 resonances in other VBF processes with four leptons in the final state	85
5.4.1	Process 211: $pp \rightarrow VV jj \rightarrow e^+ e^- \nu_\mu \bar{\nu}_\mu jj$	85
5.4.2	Process 200: $pp \rightarrow VV jj \rightarrow e^+ \nu_e \mu^- \bar{\nu}_\mu jj$	87
5.4.3	Process 220: $pp \rightarrow VV jj \rightarrow e^+ \nu_e \mu^+ \mu^- jj$ and process 230: $pp \rightarrow VV jj \rightarrow e^- \bar{\nu}_e \mu^+ \mu^- jj$	89
5.4.4	Summary of heavy Spin-2 resonances in VBF processes with four leptons in the final state	91
6	Summary	93
A	Spin-2 field and propagator	97
A.1	Spin-2 field	97
A.2	Spin-2 propagator	98
B	Decay widths of the Spin-2 singlet and triplet particles	99
B.1	Singlet	99
B.2	Triplet	101
C	Some VBFNLO files	103
C.1	vbfno.dat	103
C.2	cuts.dat	104
C.3	spin2coupl.dat	105
D	Relevant frames and transformations	106
E	Wigner d-functions	108
	Bibliography	111

1 Introduction

With the recent start of the Large Hadron Collider (LHC) at CERN, a new exciting era of particle physics has begun. As it provides energies which are high enough to cover the expected mass range of the Higgs boson, one of the main tasks of the LHC is the discovery or exclusion of the Higgs boson. This is a crucial test for the Standard Model of Elementary Particle Physics (SM) [1-3], as the Higgs boson [4, 5] is its only particle which has not been discovered yet.

There are several possible channels for the detection of the Higgs. One of them is a vector boson fusion process with two photons in the final state. For a definite detection of a Higgs resonance, all its features have to be identified. One of these features is the spin, which has to be zero for the Higgs, but whereas a spin-1 resonance is forbidden for this channel due to the Landau-Yang theorem [6], a spin-2 resonance is also possible.

So the distinction of a spin-0 and a spin-2 resonance is an important task for the Higgs detection in this channel. In order to find the characteristic features of both kinds of resonances, several distributions, like the invariant mass of the two final state photons and transverse momentum distributions, are investigated within this thesis. However, the analysis focuses on angular correlations, as they are known as a powerful tool to study the spin of a resonance.

Due to the high energies which can be achieved with the LHC, it might also be possible to detect some new, heavy resonances, which are manifestations of physics beyond the Standard Model, in vector boson fusion processes. For these resonances, a spin determination is also needed. Whereas heavy spin-1 resonances were already studied extensively (see e.g [7]), this thesis shall reveal the characteristics of heavy spin-2 resonances. Thereby, the focus is on angular distributions as well.

So the features of spin-2 resonances in vector boson fusion are studied within this thesis for two cases: Light, Higgs-like resonances in the photon pair-production channel and heavy resonances in processes with different four-lepton final states. These are $e^+ e^- \mu^+ \mu^-$, $e^+ e^- \nu_\mu \bar{\nu}_\mu$, $e^+ \nu_e \mu^- \bar{\nu}_\mu$, $e^+ \nu_e \mu^+ \mu^-$ and $e^- \bar{\nu}_e \mu^+ \mu^-$, from which the first one will be studied in most detail, since a final state which does not contain any neutrinos allows for a full reconstruction of a resonance.

After a short overview of some theoretical background in chapter 2, a model of spin-2 particles which can only interact with electroweak bosons

is developed in chapter 3. An effective Lagrangian is constructed and the corresponding Feynman rules are calculated. This is done for two different scenarios: a spin-2 state which behaves as a singlet under $SU(2)$ transformations and a spin-2 triplet in the adjoint representation.

For the simulation of spin-2 resonances in vector boson fusion processes at the LHC, the Monte Carlo program VBFNLO [8] is used. Chapter 4 illustrates the general procedure of a VBFNLO calculation as well as the implementation of the spin-2 model into VBFNLO.

The results of the analysis of spin-2 resonances are presented in chapter 5. First, unitarity constraints are investigated on the basis of longitudinal WW scattering. Afterwards, the features of spin-2 resonances are studied for the different kinds of processes.

Finally, chapter 6 gives a summary.

Some additional information can be found in the appendix. It contains the formulae of a general spin-2 field and its propagator, decay widths of the spin-2 particles, some VBFNLO files, the Wigner d-functions and details about frames and transformations which are relevant for the analysis.

2 Theoretical background

2.1 The Standard Model of Elementary Particle Physics

The Standard Model of Elementary Particle Physics (SM) [1-3] is a relativistic quantum field theory which describes the fundamental constituents of matter - the quarks and leptons, which are fermions with spin $\frac{1}{2}$ - and three of the four fundamental interactions: the strong, weak and electromagnetic interaction, but not gravity. These interactions result from the exchange of force mediating particles, which are vector bosons with spin 1.

2.1.1 Gauge groups and interactions

An important feature of the Standard Model is the principle of local gauge invariance. The corresponding gauge group is $SU(3)_C \times SU(2)_L \times U(1)_Y$.

$SU(3)_C$ is the gauge group of the strong interaction, which is described by QCD (quantum chromodynamics). The corresponding quantum number is colour (C). There are three different colours, sometimes called red, green and blue, and their corresponding anticolours.

A gauge group $SU(N)$ has $N^2 - 1$ generators, so $SU(3)$ has 8 generators. Therefore, there are eight gauge bosons which mediate the strong interaction: the eight massless gluons. Gluons couple to all particles which carry colour. As fermions these are quarks (antiquarks). Since the gluons also carry colour, the exchange of a gluon changes the colour of the quarks. Furthermore, this means that the gluons can also interact with each other, which leads to an interesting feature of QCD: The strong coupling decreases with increasing energy and therefore becomes small at small distances. This feature is called *asymptotic freedom* [9,10].

$SU(2)_L \times U(1)_Y$ is the gauge group of the electroweak interaction.

$SU(2)_L$ corresponds to the weak isospin, $U(1)_Y$ to the hypercharge Y, which is a combination of the electric charge Q and the third component of the weak isospin, I_3 : $Y = 2(Q - I_3)$.

As $SU(2)_L$ has three generators, there are three gauge bosons: W^1, W^2 and W^3 , whereas $U(1)_Y$ has only one gauge boson, B , corresponding to one generator.

The Lagrangian for these gauge bosons is:

$$\mathcal{L} = -\frac{1}{4}W_{\mu\nu}^i W_i^{\mu\nu} - \frac{1}{4}B_{\mu\nu}B^{\mu\nu}; \quad (2.1)$$

where $W_{\mu\nu}^i$ and $B_{\mu\nu}$ are the field strength tensors of the fields W_μ^i and B_μ :

$$W_{\mu\nu}^i = \partial_\mu W_\nu^i - \partial_\nu W_\mu^i + g\epsilon^{ijk}W_{j,\mu}W_{k,\nu} \quad (2.2)$$

$$B_{\mu\nu} = \partial_\mu B_\nu - \partial_\nu B_\mu. \quad (2.3)$$

g is the gauge coupling of $SU(2)_L$, whereas the gauge coupling of $U(1)_Y$ is denoted as g' .

The quarks and leptons are realized as left-handed isospin doublets

$$\begin{pmatrix} \nu_e \\ e^- \end{pmatrix}_L, \begin{pmatrix} \nu_\mu \\ \mu^- \end{pmatrix}_L, \begin{pmatrix} \nu_\tau \\ \tau^- \end{pmatrix}_L, \begin{pmatrix} u \\ d \end{pmatrix}_L, \begin{pmatrix} c \\ s \end{pmatrix}_L, \begin{pmatrix} t \\ b \end{pmatrix}_L$$

and right-handed isospin singlets $e_R^-, \mu_R^-, \tau_R^-, u_R, d_R, c_R, s_R, t_R, b_R$.

These fermions couple to the gauge bosons via the covariant derivative

$$D^\mu = \partial^\mu - igW_\mu^i \frac{\sigma^i}{2} - ig'Y_\Phi B^\mu \quad (2.4)$$

where σ^i are the Pauli matrices.

Only the left-handed fermions can interact with $SU(2)_L$ gauge bosons, so the charged current weak interactions, mediated by W^\pm (eq. 2.11, 2.12), violate parity maximally.

The principle of gauge invariance does not allow mass terms like $\frac{1}{2}m_w^2 W_\mu^i W_i^\mu$ in the Lagrangian. But experiments have shown that the physical force mediating bosons of the weak interaction are massive, whereas the photon, which mediates the electromagnetic interaction, is massless.

The gauge bosons can obtain masses via the Higgs mechanism [4,5,11].

2.1.2 Spontaneous symmetry breaking: The Higgs mechanism

In order to give masses to the gauge bosons, a complex scalar $SU(2)$ doublet field with four degrees of freedom is introduced:

$$\Phi = \begin{pmatrix} \phi_1 + i\phi_2 \\ \phi_3 + i\phi_4 \end{pmatrix} \quad (2.5)$$

Its Lagrangian is given by

$$\mathcal{L}_{Higgs} = (D_\mu \Phi)^\dagger (D^\mu \Phi) - V(\Phi^\dagger \Phi) \quad (2.6)$$

with the Higgs potential

$$V(\Phi^\dagger \Phi) = V_0 - \mu^2 \Phi^\dagger \Phi + \lambda (\Phi^\dagger \Phi)^2 \quad , \quad \mu^2, \lambda > 0 \quad (2.7)$$

and the covariant derivative D^μ (eq. 2.4).

If $\mu^2 < 0$, there would be only one trivial minimum and the gauge bosons would remain massless. But for $\mu^2 > 0$, there is a non-trivial minimum, which is defined as

$$|\Phi_0| = \sqrt{\frac{\mu^2}{2\lambda}} = \frac{v}{\sqrt{2}} \quad (2.8)$$

There are many possible ground states Φ_0 . If one of them is chosen arbitrarily, the symmetry of the theory is not a symmetry of its ground state any more, since the Lagrangian (2.6) is invariant under rotation, but the ground state is not. This fact is called spontaneous symmetry breaking.

Expanding Φ around the minimum yields, in a common parametrization

$$\Phi = \frac{1}{\sqrt{2}} e^{i\sigma_i \theta^i(x)/v} \begin{pmatrix} 0 \\ v + H(x) \end{pmatrix} \quad (2.9)$$

The excitations of the physical Higgs field are described by $H(x)$. $\theta^i(x)$ are Goldstone fields.

With the following gauge transformation, called *unitary gauge*,

$$\Phi(x) \rightarrow \Phi'(x) = U(x)\Phi(x) = e^{-i\sigma_i \theta^i(x)/v} \Phi(x) = \frac{1}{\sqrt{2}} \begin{pmatrix} 0 \\ v + H(x) \end{pmatrix} \quad (2.10)$$

the three Goldstone fields $\theta^i(x)$ can be rotated away. They turn into longitudinal degrees of freedom of the massive gauge bosons.

From the kinetic term of the Higgs Lagrangian, one can see how the gauge bosons acquire masses.

With new linear combinations of W^i and B and the Weinberg angle θ_W :

$$W_\mu^+ = \frac{1}{\sqrt{2}}(W_\mu^1 - iW_\mu^2) \quad (2.11)$$

$$W_\mu^- = \frac{1}{\sqrt{2}}(W_\mu^1 + iW_\mu^2) \quad (2.12)$$

$$Z_\mu = \frac{gW_\mu^3 - g'B_\mu}{\sqrt{g^2 + g'^2}} = W_\mu^3 \cos \theta_W - B_\mu \sin \theta_W \quad (2.13)$$

$$A_\mu = \frac{g'W_\mu^3 + gB_\mu}{\sqrt{g^2 + g'^2}} = W_\mu^3 \sin \theta_W + B_\mu \cos \theta_W \quad (2.14)$$

one obtains:

$$\begin{aligned} D^\mu \Phi &= (\partial^\mu - igW_i^\mu \frac{\sigma^i}{2} - ig' \frac{1}{2} B^\mu) \frac{1}{\sqrt{2}} \begin{pmatrix} 0 \\ v + H(x) \end{pmatrix} \\ &= \frac{1}{\sqrt{2}} \left[\begin{pmatrix} 0 \\ \partial^\mu H \end{pmatrix} - \frac{i}{2} (v + H) \begin{pmatrix} g(W_1^\mu - iW_2^\mu) \\ -gW_3^\mu + g'B^\mu \end{pmatrix} \right] \\ &= \frac{1}{\sqrt{2}} \begin{pmatrix} 0 \\ \partial^\mu H \end{pmatrix} - \frac{i}{2} \left(1 + \frac{H}{v}\right) \begin{pmatrix} gvW^{\mu+} \\ -\sqrt{\frac{g^2 + g'^2}{2}} v Z^\mu \end{pmatrix} \end{aligned} \quad (2.15)$$

and

$$(D_\mu \Phi)^\dagger (D^\mu \Phi) = \frac{1}{2} \partial^\mu H \partial_\mu H + \left[\left(\frac{gv}{2}\right)^2 W^{\mu+} W_\mu^- + \frac{1}{2} \frac{(g^2 + g'^2)v^2}{4} Z^\mu Z_\mu \right] \left(1 + \frac{H}{v}\right)^2 \quad (2.16)$$

So the W^\pm and Z bosons acquire the masses

$$m_W = \frac{gv}{2} \quad , \quad m_Z = \frac{\sqrt{g^2 + g'^2}v}{2} \quad (2.17)$$

and the photon stays massless.

The measured value of the Fermi constant G_F yields

$$v = \sqrt{\frac{1}{\sqrt{2}G_F}} \approx 246,22 \text{ GeV.}$$

From the $\frac{2H}{v}$ term in (2.16), one can obtain the HWW and HZZ couplings, which are proportional to the masses of W^\pm and Z .

With the Higgs mechanism, also fermion mass terms can be generated. Terms like $-m\bar{\Psi}\Psi$ are not gauge invariant, but a Yukawa coupling of the fermions to the scalar field leads to fermion masses corresponding to gauge invariant mass terms. Further details about fermion mass terms are not needed here, because fermion masses are neglected in this thesis.

2.2 Calculating Feynman Rules from a given Lagrangian

In order to give theoretical predictions for elementary particle processes, one has to calculate physical quantities like cross sections or decay widths. Therefore it is essential to know the Feynman rules of the corresponding theory.

If the Lagrangian of a theory is known, the Feynman rules can be calculated with the following procedure [12]:

Let \mathcal{L} be a sum of terms which contain several fields. Each group of fields will form a vertex with external lines of these fields and with corresponding Feynman rules.

1. Take all the terms in $i\mathcal{L}$ which contain exactly the fields of the vertex you want to calculate. If the fields contain upper and lower indices (also if one field has an upper and another field has a lower index), rewrite the terms in such a way that all the fields contain only upper or only lower indices.
2. Replace every derivative by $(-i)$ times the incoming momentum of the field on which it acts.
3. Sum over all permutations of the indices and momenta of equal external fields.
4. Delete all the external fields.

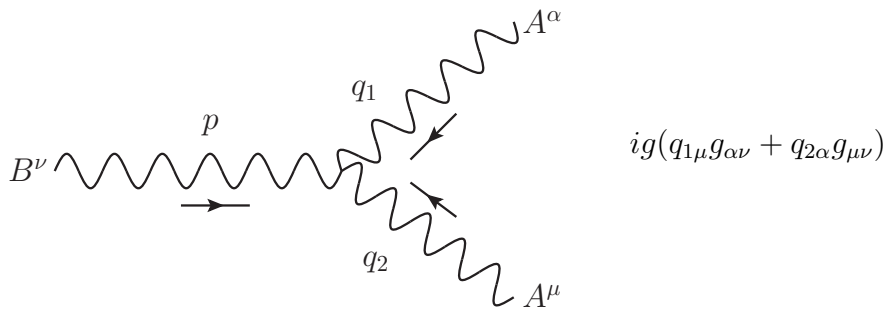
Example: Let a fictitious Lagrangian be

$$\mathcal{L} = ig(\partial_\mu A_\nu)A^\mu B^\nu + g'A^\mu D_\mu C$$

There are two vertices: one with the external fields A, A, B and one with A, D, C:

First vertex:

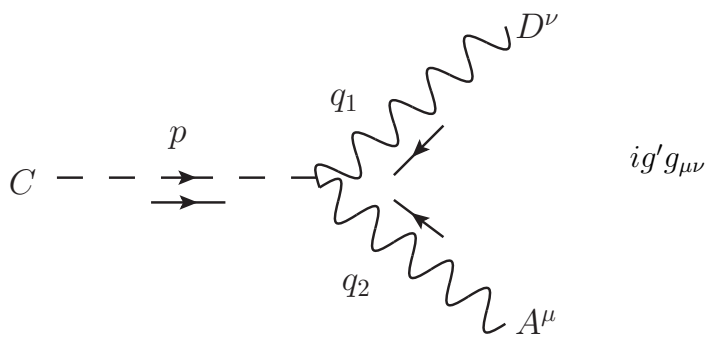
1. $\rightarrow -g(\partial_\mu A_\nu)A^\mu B^\nu = -g(\partial_\mu A^\alpha)g_{\alpha\nu}A^\mu B^\nu$
2. $\rightarrow -g(-iq_{1\mu})g_{\alpha\nu}A^\alpha A^\mu B^\nu = ig(q_{1\mu}g_{\alpha\nu})A^\alpha A^\mu B^\nu$
3. $\rightarrow ig(q_{1\mu}g_{\alpha\nu} + q_{2\alpha}g_{\mu\nu})A^\alpha A^\mu B^\nu$
4. $\rightarrow ig(q_{1\mu}g_{\alpha\nu} + q_{2\alpha}g_{\mu\nu})$



$$ig(q_{1\mu}g_{\alpha\nu} + q_{2\alpha}g_{\mu\nu})$$

Second vertex:

1. $\rightarrow ig' A^\mu D_\mu C = ig' g_{\mu\nu} A^\mu D^\nu C$
2. nothing to do
3. nothing to do
4. $\rightarrow ig' g_{\mu\nu}$



$$ig' g_{\mu\nu}$$

2.3 Effective field theories

If one wants to develop new theories of physics beyond the Standard Model, one can either try to construct a specific model or use a model-independent ansatz: the effective Lagrangian formalism ([13], [14]).

In the latter case, the actual new theory (which is not worked out explicitly in the effective theory) is assumed to manifest itself above a certain energy scale Λ . However, this energy scale is assumed to be very high, so it is far from experimental reach. The effective Lagrangian formalism is understood to be a low-energy approximation of the actual, unknown theory (where low always means low in comparison with Λ), so the effective Lagrangian is an expansion in inverse powers of Λ :

$$\mathcal{L}_{eff} = \mathcal{L}_0 + \frac{1}{\Lambda} \mathcal{L}_1 + \frac{1}{\Lambda^2} \mathcal{L}_2 + \dots \quad (2.18)$$

In contrast to the Standard Model Lagrangian, such an effective Lagrangian is not renormalizable. All terms of a Lagrangian always have dimension four, so that the action is dimensionless. Due to the factors $\frac{1}{\Lambda^n}$, the terms \mathcal{L}_i contain operators of higher dimensions.

In principle, the effective Lagrangian can contain an infinite number of terms. However, terms of higher order are suppressed by high powers of $\frac{1}{\Lambda}$, so they do not need to be considered. Typically, only the first non-vanishing order is kept.

One of the main assumptions of an effective field theory concerns the low-energy symmetries. Another one is the low-energy particle content. This can be the Standard Model particle content, but also new particles can be added, like the spin-2 particles in this thesis (see chapter 3). The underlying high-energy theory is assumed to contain additional heavy particles, whose masses correspond to the energy scale Λ . Although they cannot be produced directly in low-energy reactions, they influence the low-energy interactions through their virtual effects.

Now let's look at a famous example to illustrate the general formalism of effective field theories, the Fermi theory.

2.3.1 Example: The Fermi theory

The Fermi theory is the low-energy effective theory of the weak interactions. An early version of it was written down during the 1930's as a theory of the beta decay of nucleons, but it can also describe other weak processes. Let's take τ decay as an example to look at the low-energy effects due to the interaction of the W boson with light particles:

The amplitude for the τ decay $\tau(\mathbf{k}) \rightarrow \nu_\tau(\mathbf{l})\bar{f}_m(\mathbf{q})f_n(\mathbf{p})$ is given by [13]:

$$\begin{aligned} \mathcal{M}(\tau \rightarrow \nu_\tau\bar{f}_mf_n) &= e_W^2 U_{mn}^* [\bar{u}_\nu(\mathbf{l})\gamma^\mu(1 - \gamma_5)u_\tau(\mathbf{k})][\bar{u}_n(\mathbf{p})\gamma^\nu(1 - \gamma_5)v_m(\mathbf{q})] \\ &\quad * \left[\frac{g_{\mu\nu} - (k-l)_\mu(k-l)_\nu/M_W^2}{(k-l)^2 - M_W^2 + i\epsilon} \right] \end{aligned} \quad (2.19)$$

where U_{mn}^* is a unitary matrix which accounts for a mixing between leptons of different generations.

In the low-energy approximation, this amplitude is simplified by expanding the propagator of the W boson in inverse powers of M_W^2 :

$$\begin{aligned} \left[\frac{g_{\mu\nu} - (k-l)_\mu(k-l)_\nu/M_W^2}{(k-l)^2 - M_W^2 + i\epsilon} \right] &\approx -\frac{g_{\mu\nu}}{M_W^2} \left[1 - \frac{(k-l)^2}{M_W^2} + \dots \right] \\ &\quad + \frac{(k-l)_\mu(k-l)_\nu}{M_W^4} [1 + \dots] \end{aligned} \quad (2.20)$$

If only the lowest order term in this expansion is kept, (2.19) becomes:

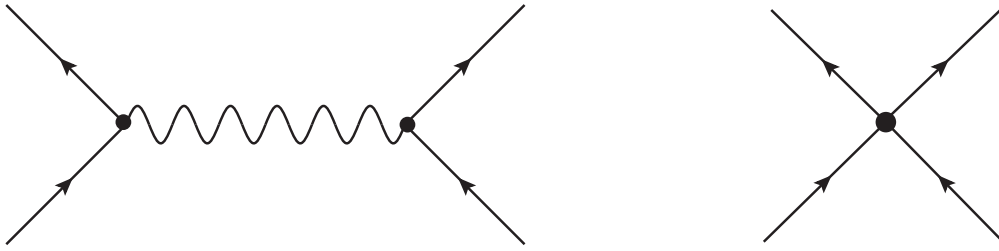
$$\mathcal{M}(\tau \rightarrow \nu_\tau\bar{f}_mf_n) = -\frac{G_F}{\sqrt{2}} U_{mn}^* [\bar{u}_\nu(\mathbf{l})\gamma^\mu(1 - \gamma_5)u_\tau(\mathbf{k})][\bar{u}_n(\mathbf{p})\gamma_\mu(1 - \gamma_5)v_m(\mathbf{q})] \quad (2.21)$$

where G_F is the Fermi coupling constant and $G_F/\sqrt{2} = e_W^2/M_W^2$.

Exactly the same matrix element (2.21) is obtained at lowest order in perturbation theory from the effective Lagrangian

$$\mathcal{L} = \frac{G_F}{2\sqrt{2}} U_{mn}^* [\bar{\nu}_\tau\gamma^\mu(1 - \gamma_5)\tau][\bar{f}_n\gamma_\mu(1 - \gamma_5)f_m] + c.c. \quad (2.22)$$

As G_F has mass dimension -2, this Lagrangian is an example of a $\frac{1}{\Lambda^2}\mathcal{L}_2$ term of the general effective Lagrangian (2.18). Here, the W mass plays the role of the energy scale Λ .



Whereas the matrix element (2.19) corresponds to a Feynman diagram with virtual W exchange (left hand side of the above figure), the matrix element of the effective theory, (2.21), corresponds to the effective four vertex Feynman diagram on the right hand side of the figure.

3 Lagrangian and Feynman Rules for the interaction of a Spin-2 particle with electroweak bosons

In this chapter, effective Lagrangians for the interaction of a spin-2 particle with electroweak bosons are constructed and the Feynman rules, which result from these Lagrangians, are given.

This is done for two cases. In the first part, a spin-2 state which behaves as a singlet under $SU(2)$ transformations is presented, and in the second part, a spin-2 triplet in the adjoint representation follows.

These states are described by the general spin-2 fields $T_{\mu\nu}$ (singlet) and $T_{\mu\nu}^j$ (triplet) (see appendix A). These fields are symmetric in μ, ν , transverse and $T_{\mu}^{\mu} = T_{\mu}^{\mu j} = 0$.

3.1 Spin-2 singlet

3.1.1 Lagrangian

To develop a model for the interaction of a spin-2 singlet particle with electroweak bosons, a Lagrangian needs to be constructed.

To this end, an effective ansatz (see chapter 2.3) is used:

$$\mathcal{L}_{eff,singlet} = \sum_i \frac{f_i}{\Lambda} T_{\mu\nu} O_i^{\mu\nu} \quad (3.1)$$

f_i are variable, dimensionless coupling parameters, Λ is the energy scale, at which the new theory manifests itself, $T_{\mu\nu}$ is the general spin-2 singlet field (see appendix A) and $O_i^{\mu\nu}$ are operators which have to be constructed.

From the features of the spin-2 field $T_{\mu\nu}$ mentioned above, one can conclude that the operators $O_i^{\mu\nu}$ must have at least dimension 4.

Λ is supposed to be very high, otherwise effects of the model would have been visible in earlier experiments. Therefore, terms of higher order are suppressed and do not have to be considered here.

Now the operators have to be constructed. Therefore, one has to determine their possible ingredients first:

As this model should treat the interaction of the spin-2 particle with photons, W and Z bosons, but not with gluons, fermions or any particles which are not part of the SM, the only suitable ingredients are the vector fields V^{μ} (which can be $W^{\pm\mu}$, Z^{μ} or A^{μ}), the scalar Higgs field Φ and the covariant derivative D^{μ} (see chapter 2.1).

Furthermore, there are several constraints which limit the number of operators:

- As mentioned previously, the dimension of $O_i^{\mu\nu}$ must be four. Thereby, Φ , D^μ and V^μ all have mass dimension one. Also the result must be a rank-2 Lorentz tensor $O^{\mu\nu}$, with all other Lorentz indices properly contracted.
- Gauge invariance needs to be respected. As the operators $O_i^{\mu\nu}$ have to be SU(2) invariant, $O_i^{\mu\nu}$ cannot contain a Higgs field Φ without its hermitian conjugate Φ^\dagger and vice versa.
- Furthermore, the operators always have to contain an even number of V^μ and D^μ to ensure Lorentz invariance.
- $O^{\mu\nu}$ cannot be antisymmetric, because $T_{\mu\nu}$ is symmetric (see its definition in appendix A) and the product of a symmetric and an antisymmetric tensor gives zero.
- Operators of the form ($g^{\mu\nu}$ times a scalar) do not have to be considered, as they only contribute to off-shell spin-2 states. This can be easily seen by looking at $T_{\mu\nu}O_i^{\mu\nu} = T_{\mu\nu}g^{\mu\nu} \cdot \text{scalar} = T_\mu^\mu \cdot \text{scalar}$ and showing $\epsilon_\mu^\mu = 0$ from the explicit form of the polarization vectors (see appendix A). Therefore, such terms cannot contribute to spin-2 resonances.

Although one can think of many combinations of V^μ , Φ and D^μ which could form operators, these constraints exclude most of them. Finally, there are only five suitable operators left to form the effective Lagrangian of the spin-2 singlet model:

$$\begin{aligned} \mathcal{L}_{eff,singlet} = \frac{1}{\Lambda} T_{\mu\nu} & \left(f_1 B^{\alpha\nu} B^\mu{}_\alpha + f_2 W_i^{\alpha\nu} W^{i\mu}{}_\alpha + f_3 \widetilde{B}^{\alpha\nu} B^\mu{}_\alpha \right. \\ & \left. + f_4 \widetilde{W}_i^{\alpha\nu} W^{i\mu}{}_\alpha + 2f_5 (D^\mu \Phi)^\dagger (D^\nu \Phi) \right) \end{aligned} \quad (3.2)$$

where $B^{\alpha\nu}$ and $W_i^{\alpha\nu}$ are the field strength tensors given by eq. (2.2) and (2.3) and

$$\begin{aligned} \widetilde{B}^{\alpha\nu} &= \frac{1}{2} \epsilon^{\alpha\nu\rho\sigma} B_{\rho\sigma} \\ \widetilde{W}_i^{\alpha\nu} &= \frac{1}{2} \epsilon^{\alpha\nu\rho\sigma} W_{i\rho\sigma} \end{aligned} \quad (3.3)$$

are the corresponding dual field strength tensors.

The factor 2 in front of the f_5 term is a relic of its symmetry. One could also take the term $T_{\mu\nu}(D^\nu\Phi)^\dagger(D^\mu\Phi)$, but as $T_{\mu\nu}$ is symmetric, this is equal to $T_{\mu\nu}(D^\mu\Phi)^\dagger(D^\nu\Phi)$.

It is interesting to compare the Lagrangian (3.2) with the Lagrangian for gravitons given in [15]:

$$\mathcal{L}_G = -\frac{1}{\Lambda} \sum_n T^{(n)\mu\nu} \mathcal{T}_{\mu\nu} \quad (3.4)$$

where $T^{(n)\mu\nu}$ is the n-th graviton Kaluza-Klein mode, which corresponds to the general spin-2 field $T^{\mu\nu}$ and $\mathcal{T}_{\mu\nu}$ is the energy-momentum tensor of the SM fields. $\mathcal{T}^{\mu\nu}$ contains terms analogous to $B^{\alpha\nu}B^\mu_\alpha$ and $W_i^{\alpha\nu}W^{i\mu}_\alpha$, but also terms describing the couplings of the gravitons to fermions and gluons, which are not part of (3.2), because we restrict ourselves to a model of the interaction of a spin-2 particle with electroweak bosons.

The terms of $\mathcal{L}_{eff,singlet}$ containing $\tilde{B}^{\alpha\nu}$ and $\tilde{W}_i^{\alpha\nu}$ are not part of the graviton Lagrangian. As the results will show, these terms do not lead to spin-2 resonances, but they can influence the total cross sections of the considered processes (see section 5.3.1 and fig. 5.41).

Another important feature of $\mathcal{L}_{eff,singlet}$ is the presence of variable prefactors f_i , whereas the prefactors of \mathcal{L}_G are fixed by the theory.

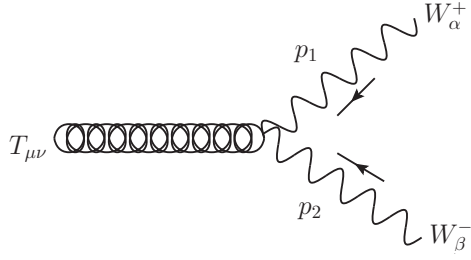
3.1.2 Feynman Rules

In order to derive the Feynman rules from the effective singlet Lagrangian (3.2), first B and W^i are replaced with W^\pm , Z and A according to eq. (2.11)-(2.14). This yields a Lagrangian with many terms, from which the Feynman rules can be calculated by following the procedure given in chapter 2.2. The present Feynman rules were calculated by hand as well as cross-checked by the programs FeynRules [16] and LanHEP [17].

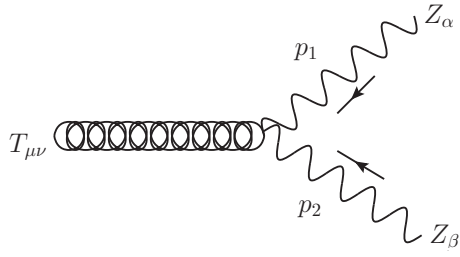
All in all, this yields 17 vertices, with 3, 4 or 5 particles attached to the vertex, like: THH , THW^+W^- , $T\gamma W^+W^-Z$ etc.

However, most of them are not needed to analyze processes in vector boson fusion. The four relevant vertices, which will appear, are TW^+W^- , TZZ , $T\gamma\gamma$ and $T\gamma Z$.

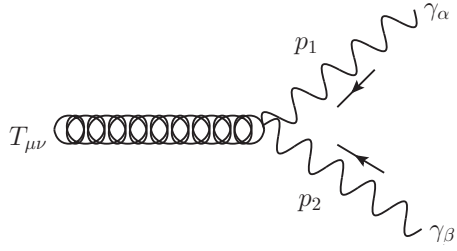
Note that it is not necessary to symmetrize the following Feynman rules, since the spin-2 field $T_{\mu\nu}$ is symmetric.



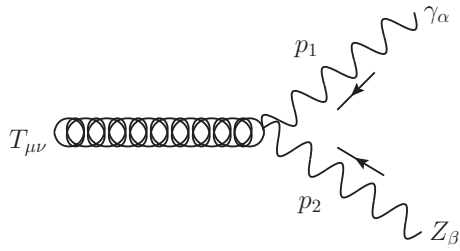
$$\frac{2if_2}{\Lambda} K_1^{\alpha\beta\mu\nu} + \frac{if_4}{\Lambda} K_2^{\alpha\beta\mu\nu} + \frac{if_5 g^2 v^2}{2\Lambda} K_3^{\alpha\beta\mu\nu}$$



$$\frac{2i}{\Lambda} (f_2 c_w^2 + f_1 s_w^2) K_1^{\alpha\beta\mu\nu} + \frac{i}{\Lambda} (f_4 c_w^2 + f_3 s_w^2) K_2^{\alpha\beta\mu\nu} + \frac{if_5 v^2}{2\Lambda} (g^2 + g'^2) K_3^{\alpha\beta\mu\nu}$$



$$\frac{2i}{\Lambda} (f_1 c_w^2 + f_2 s_w^2) K_1^{\alpha\beta\mu\nu} + \frac{i}{\Lambda} (f_3 c_w^2 + f_4 s_w^2) K_2^{\alpha\beta\mu\nu}$$



$$\frac{2i}{\Lambda} c_w s_w (f_2 - f_1) K_1^{\alpha\beta\mu\nu} + \frac{i}{\Lambda} c_w s_w (f_4 - f_3) K_2^{\alpha\beta\mu\nu}$$

with $c_w = \cos\theta_W$, $s_w = \sin\theta_W$ and

$$\begin{aligned}
K_1^{\alpha\beta\mu\nu} &= p_1^\nu p_2^\mu g^{\alpha\beta} - p_1^\beta p_2^\nu g^{\alpha\mu} - p_2^\alpha p_1^\nu g^{\beta\mu} + p_1 \cdot p_2 g^{\alpha\nu} g^{\beta\mu} \\
K_2^{\alpha\beta\mu\nu} &= p_{2\rho} p_{1\sigma} g^{\alpha\mu} \epsilon^{\beta\nu\sigma\rho} + p_{1\rho} p_{2\sigma} g^{\beta\mu} \epsilon^{\alpha\nu\sigma\rho} + (p_{1\rho} p_2^\mu - p_{2\rho} p_1^\mu) \epsilon^{\alpha\beta\nu\rho} \\
K_3^{\alpha\beta\mu\nu} &= g^{\alpha\nu} g^{\beta\mu}
\end{aligned} \tag{3.5}$$

The variables g , g' , v , $\cos\theta_W$ and $\sin\theta_W$ have already been defined in chapter 2.1.

3.2 Spin-2 triplet

In this section, the Lagrangian and the Feynman rules for a spin-2 triplet are presented. While the spin-2 singlet involves only one uncharged particle, T , the triplet consists of three spin-2 particles: T^1 , T^2 and T^3 , which form charged and neutral linear combinations analogous to W^\pm from W^1 and W^2 (see eq. 2.11, 2.12):

$$\begin{aligned}
T^\pm &= \frac{1}{\sqrt{2}}(T^1 \mp i T^2) \\
T^0 &= T^3
\end{aligned} \tag{3.6}$$

So the constituents of the spin-2 triplet are one pair of charged particles and one uncharged particle.

3.2.1 Lagrangian

For the construction of the triplet Lagrangian, the effective ansatz is nearly the same as for the singlet Lagrangian. It just contains an additional summation over the index j ($j = 1, 2, 3$) of the triplet particles.

$$\mathcal{L}_{eff,triplet} = \sum_{i,j} \frac{f_i}{\Lambda} T_{\mu\nu}^j O_{i,j}^{\mu\nu} \tag{3.7}$$

The operators can be constructed by applying the same rules as in the singlet case. The resulting triplet Lagrangian is:

$$\begin{aligned}
\mathcal{L}_{eff,triplet} &= \frac{1}{\Lambda} T_{\mu\nu j} (f_6 (D^\mu \Phi)^\dagger \sigma^j (D^\nu \Phi) + f_7 W_{\alpha}^{j\mu} B^{\alpha\nu} \\
&\quad + f_8 \epsilon^{ijk} W_i^{\mu\alpha} W_{k\alpha}{}^\nu)
\end{aligned} \tag{3.8}$$

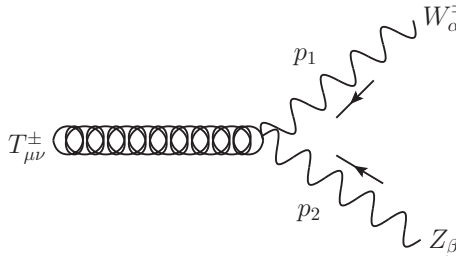
Similar to the singlet Lagrangian, also here terms with dual field strength tensors would be possible, but as the results of the singlet case show, these do not lead to spin-2 resonances. Therefore, they are neglected already at this stage.

3.2.2 Feynman Rules

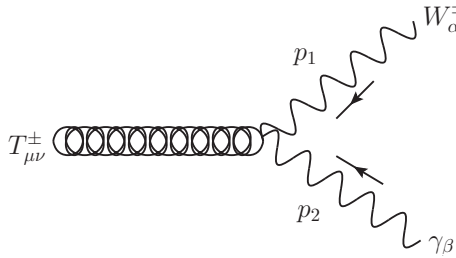
From the triplet Lagrangian (3.8), the following Feynman rules were calculated by hand by applying the procedure of chapter 2.2. They have also been cross-checked with LanHEP. The fields B and W^i are replaced with W^\pm , Z and A according to eq. (2.11-2.14) and T^j are replaced with T^\pm and T^0 (eq. (3.6)).

This yields 38 vertices in total, which contain 3, 4 or 5 particles, for example: $T^0 H H$, $T^0 H W^+ W^-$, $T^0 \gamma W^+ W^-$, $T^\pm W^\mp \gamma Z$, $T^0 Z H H$, $T^\pm W^\mp H H$, $T^0 W^+ W^- Z Z$, $T^\pm W^\mp W^+ W^- Z$.

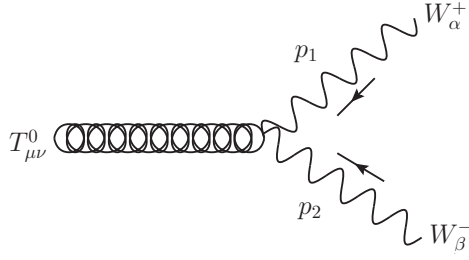
However, as in the singlet case, most of them are not needed for the analysis of processes in vector boson fusion. The relevant vertices are:



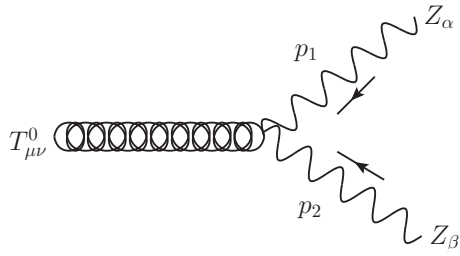
$$-\frac{if_6}{4\Lambda} g v^2 \sqrt{g^2 + g'^2} K_3^{\alpha\beta\mu\nu} - \frac{if_7}{\Lambda} s_w K_1^{\alpha\beta\mu\nu}$$



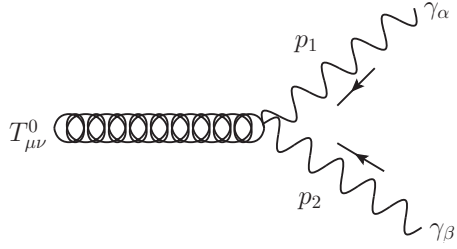
$$\frac{if_7}{\Lambda} c_w K_1^{\alpha\beta\mu\nu}$$



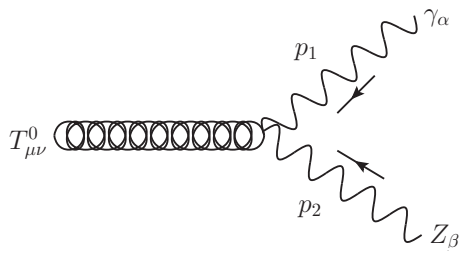
$$\frac{if_6}{4\Lambda} g^2 v^2 K_3^{\alpha\beta\mu\nu}$$



$$-\frac{if_6}{4\Lambda} (g^2 + g'^2) v^2 K_3^{\alpha\beta\mu\nu} - \frac{2if_7}{\Lambda} c_w s_w K_1^{\alpha\beta\mu\nu}$$



$$\frac{2if_7}{\Lambda} c_w s_w K_1^{\alpha\beta\mu\nu}$$



$$\frac{if_7}{\Lambda} (c_w^2 - s_w^2) K_1^{\alpha\beta\mu\nu}$$

with $K_1^{\alpha\beta\mu\nu}$ and $K_3^{\alpha\beta\mu\nu}$ as in the singlet case (see eq. (3.5)).

Note that these vertices do not contain a term proportional to f_8 . This coupling only appears when considering vertices with 4 or 5 particles. So for the following VBFNLO analysis, the f_8 term of the Lagrangian (3.8) does not play any role.

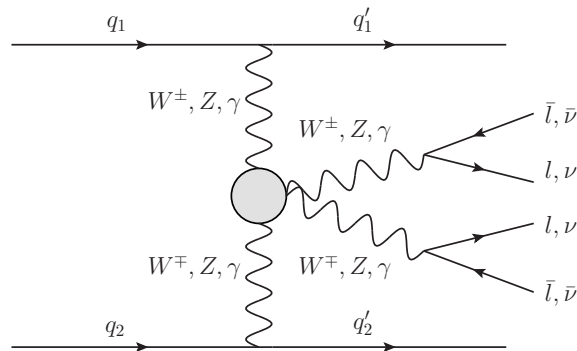
4 Implementation into VBFNLO

One of the main tasks of this thesis was the implementation of the model for spin-2 particles developed in chapter 3 into the program VBFNLO [8]. With this program, it is possible to simulate the influence of this model on electroweak boson fusion and to get predictions for total cross sections, angular distributions etc. This chapter illustrates the general features of VBFNLO as well as the changes which were performed concerning the spin-2 model.

4.1 Vector Boson Fusion and the program VBFNLO

VBFNLO is a parton level Monte Carlo program written in FORTRAN, which simulates vector boson fusion (VBF) processes at next-to-leading order (NLO) in the strong coupling constant α_s . It was created by D. Zeppenfeld et al. and is still enlarged by various effects (especially beyond standard model aspects) at the ITP in Karlsruhe. The main result of a VBFNLO calculation is the total cross section of a vector boson fusion process at a proton-proton collider like the LHC. This thesis focuses on electroweak boson fusion processes at leading order.

The topology of typical electroweak boson fusion processes is shown in the following figure:



The circular area involves various subdiagrams which are contained in the so-called *leptonic tensors*.

The different processes which can be calculated with VBFNLO are distinguished by the final states. The initial state consists of two protons, but it is also possible to switch to a proton and an antiproton.

The following table gives an overview of all the processes which are relevant for this thesis:

Process ID	Name	Final state
200	WPWMjj	$e^+ \nu_e \mu^- \bar{\nu}_\mu jj$
210	ZZjj_ll	$e^+ e^- \mu^+ \mu^- jj$
211	ZZjj_lnu	$e^+ e^- \nu_\mu \bar{\nu}_\mu jj$
220	WPZjj	$e^+ \nu_e \mu^+ \mu^- jj$
230	WMZjj	$e^- \bar{\nu}_e \mu^+ \mu^- jj$
240	AAjj	$\gamma\gamma jj$
101	Hjj_AA	$\gamma\gamma jj$

where jj denotes two jets in the final state which result from the two quarks emerging from the interaction process.

The cross section for a general hadron collider process can be written as [18]

$$\sigma = \int dx_1 dx_2 \sum_{subprocesses} f_{a_1/p}(x_1, \mu_F^2) f_{a_2/p}(x_2, \mu_F^2) \frac{1}{2\hat{s}} \int dLIPS_{2 \rightarrow n} \theta(cuts) \overline{|\mathcal{M}|^2}(a_1 a_2 \rightarrow b_1 \dots b_n). \quad (4.1)$$

Here, $f_{a_i/p}(x_i, \mu_F^2)$ is the parton distribution function (PDF) of the proton for the parton a_i , with x_i being the fraction of the proton momentum carried by the parton a_i and μ_F being the factorization scale. \hat{s} is the square of the centre of mass energy for the particular partonic subprocess, $dLIPS_{2 \rightarrow n}$ is the Lorentz invariant phase space element for a process with 2 initial particles going to n final particles and $\theta(cuts)$ is a Heaviside step function which sets some constraints on the final state configurations, e.g. to exclude regions of the phase space which cannot be seen in a real detector experiment. $\overline{|\mathcal{M}|^2}$ finally denotes the square of the matrix element of the particular subprocess, which includes the sum over the different polarizations and colours of the final state partons and the average of these for the initial state partons.

This integral cannot be solved analytically, not only because it is very complex, but also because the PDFs are only known numerically. Therefore, VBFNLO uses the Monte Carlo integration method to solve the integral (4.1) numerically.

A basic Monte Carlo integration works as follows [19]:

For the calculation of a d dimensional integral over the unit hypercube $[0, 1]^d$

$$I = \int_{V=[0,1]^d} f(\vec{x}) d^d x \quad (4.2)$$

a basic Monte Carlo algorithm chooses N uniformly distributed points \vec{x}_n randomly out of V . Then, the Monte Carlo estimate for the integral is given by

$$I_{MC} = \frac{1}{N} \sum_{n=1}^N f(\vec{x}_n) \quad (4.3)$$

Due to the law of large numbers, the Monte Carlo estimate converges to the true value of the integral:

$$\lim_{N \rightarrow \infty} \frac{1}{N} \sum_{n=1}^N f(\vec{x}_n) = I \quad (4.4)$$

The error in such a Monte Carlo integration scales like $\frac{\sigma(f)}{\sqrt{N}}$, where $\sigma(f)$ is the standard deviation of f .

In order to reduce both error and running time, VBFNLO uses a modified version of an algorithm called VEGAS [20].

A leading order calculation in VBFNLO proceeds through the following steps:

First, the parameters of the process are read in. The general parameters can be set in the data file **vbfnlo.dat**, the cuts can be set in **cuts.dat** and some specific parameters for specific models can be set in other **.dat** files, like the spin-2 parameters of this thesis in **spin2coupl.dat** (for these data files, see Appendix C). According to these parameters, the random number generator, the routine for the integration, the histogram routine etc. are initialized.

The actual calculation is executed with two nested loops: The first one runs over the different iterations of the Monte Carlo algorithm, while the second one runs over the different points of the phase space. The main routine, where all the parts of the calculation come together, is **vbfnlo_main.F**.

The contribution of every phase space point of each iteration to the cross section is calculated in the following way:

The routine for the integration yields an array of random numbers and their corresponding weights.

The routine **phasespace.F** converts these random numbers into the corresponding particle momenta.

A phase space point only contributes to the cross section if it is accepted by the set of cuts. Otherwise its weight and therefore its contribution is set to zero and the rest of the calculation process is skipped.

After that, the factorization and renormalization scale for the phase space point are calculated.

Then, the square of the matrix element is calculated by the corresponding subroutine which is called by the function **amplitudes.F**. The result is multiplied with a phase space factor and is transferred, together with its weight, to the routine for the integration.

The output of the integration is the total cross section of the process and its statistical error.

For the last iteration of the calculation, there is the additional option to use the routine **histograms.F**, which provides the tools to create some histograms (like for example the distribution of transverse momenta or angular distributions) and which can easily be modified by the user for the individual histograms he is interested in.

For a NLO calculation, there are additional contributions to the cross section which have to be calculated, but the principal steps of the calculation are the same.

In order to get a fast calculation, the leptonic tensors are calculated separately and afterwards included at the desired place.

The topology of a part of a VBF process (see figure) can be written as:

$$\mathcal{M} = \mathcal{J}_{q1}^\mu \mathcal{J}_{q2}^\nu \mathcal{L}_{\mu\nu} \quad (4.5)$$

The leptonic tensor $\mathcal{L}_{\mu\nu}$ is the part of the amplitude which results from cutting off the electroweak boson propagators that connect the circular area with the quarks. It is independent of the QCD part of the different subprocesses and therefore it has to be calculated only once for each phase space point.

The leptonic tensors are calculated by calling specific subroutines, the so-called *HELAS routines* [21]. Often the calls can be generated by the program MADGRAPH, but they can be implemented 'by hand' as well, which was done for the spin-2 processes.

4.2 Overview of the implementation of the Spin-2 model into VBFNLO

For the implementation of the spin-2 model into VBFNLO, the following changes were performed:

- A switch was implemented, which decides whether the spin-2 model should be included into the VBFNLO calculation or not. It can be set in **vbfno.dat**.
- For the parameters of the spin-2 model (couplings, masses, etc.), the files **spin2coupl.dat**, **spin2coupl.inc** and **spin2coupl.F** were created: In **spin2coupl.inc**, the new variables are stored in a common block, they can be set in **spin2coupl.dat** and are read in **spin2coupl.F**.
- New HELAS routines were created which are used to calculate the different Feynman diagrams involving spin-2 particles.
- The leptonic tensors of the VBF processes for electroweak boson pair production with four leptons in the final state (200, 210, 211, 220 and 230) were enlarged by the additional Feynman diagrams which contain spin-2 particles, where each diagram is calculated by a set of calls of HELAS routines. Furthermore, a formfactor (see chapter 5.1, eq. 5.4) is defined and multiplied to the corresponding subamplitudes.
- The new VBF process 240, $pp \rightarrow \gamma\gamma jj$ via a spin-2 resonance, was created.
- The widths of the spin-2 particles (see Appendix B) were implemented. They are needed for the calculation of the spin-2 propagators, which is performed in the HELAS routines.
- Some phase space files were slightly modified in order to adjust them to spin-2 resonances.
- The subroutine **histograms.F** was enlarged by various histograms.

4.3 New HELAS routines and extension of the leptonic tensors

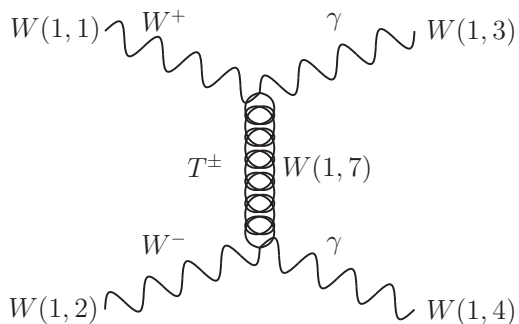
A significant part of the implementation of the spin-2 model into VBFNLO was the extension of the leptonic tensors. They contain the additional Feynman

diagrams which include the coupling of a spin-2 particle to electroweak bosons. Also new HELAS routines for their calculation have been created.

The original files which calculate the leptonic tensors are called **toww.F** for process 200, **tozz.F** for the processes 210 and 211 and **towz.F** for 220 and 230. The corresponding extended files, which include the spin-2 diagrams, are called **toww_spin2.F**, etc. For the new process 240, a new leptonic tensor file called **spin2toaa.F** was created.

A leptonic tensor file consists of several subroutines which calculate the Feynman diagrams of the corresponding subprocess by a set of calls of HELAS routines. For the calculation of new Feynman diagrams involving spin-2 particles, new HELAS routines, which apply the Feynman rules of the spin-2 model (see chapter 3), must be used.

The following example shall illustrate the general procedure:



The diagram on the left is the third diagram of a subroutine of spin2toaa.F. The corresponding code for its calculation is:

```
CALL VXXXXX(P(0,3), ZERO, lsign(3), 1, W(1,3))
CALL VXXXXX(P(0,4), ZERO, lsign(4), 1, W(1,4))
CALL VCARTX(Q1(0), WMASS, wwidth, MU, -1, W(1,1))
CALL VCARTX(Q2(0), WMASS, wwidth, NU, -1, W(1,2))
CALL UWAXXX_TRIPPM(W(1,1),W(1,3) , W(1,7))
CALL WATXXX_TRIPPM(W(1,2),W(1,4), W(1,7) , AMP(3))
```

The first four lines compute the external lines of the diagram, which are the same for all diagrams of the corresponding subroutine. Therefore, only lines like the two last lines need to be added for further diagrams.

Whereas the first four lines are calls of HELAS routines which were already implemented before, the last two lines, which contain the spin-2 couplings, are calls of new spin-2 HELAS routines.

UWAXXX_TRIPPM calculates the off-shell tensor current $W(1,7)$ of the charged spin-2 triplet particle T^\pm from the input wave functions $W(1,1)$ and $W(1,3)$. WATXXX_TRIPPM returns the vertex function $AMP(3)$, which is calculated from the input functions $W(1,2)$, $W(1,4)$ and $W(1,7)$.

More detailed information about these calculations can be found below (see eq. 4.6 and 4.7).

At the end of a subroutine, the corresponding leptonic tensor is calculated by adding up all the vertex functions $AMP(i)$ and can be multiplied by a formfactor, which is implemented in each of the leptonic tensor subroutines as well.

As the example shows, there are two different kinds of spin-2 HELAS routines: Those which calculate an off-shell tensor current and those which calculate a vertex. Furthermore, as there are different Feynman rules for different electroweak bosons involved in a vertex, there must be two HELAS routines for each kind of combination of bosons which couple to the spin-2 particle (one for the current and one for the vertex). Last but not least, each spin-2 particle (the singlet particle T , the neutral triplet particle T^0 and the charged triplet particles T^\pm) has its own set of HELAS routines.

So, all in all, there are 20 spin-2 HELAS routines which were created. The notation is as follows: The name of the 10 tensor current functions begins with a U and the following two letters indicate which vector bosons are involved. The first three letters of the 10 vertex functions denote the involved particles. The three X in both of them are just a convention. The spin-2 singlet functions are named ...SING, the neutral triplet functions ...TRIPN and the charged triplet functions ...TRIPPM.

The structure of a spin-2 HELAS routine which calculates an off-shell tensor current, like UWAXXX_TRIPPM($w1, a2$, uwa), is:

- $w1$ and $a2$ are complex input wave functions ($w1$ denotes the W boson, $a2$ the photon) with 6 components. The output of the routine is the complex tensor current uwa , which has 18 components.
- After reading the four-momenta of the W boson and the photon from the fifth and sixth component of $w1$ and $a2$, the momentum of the spin-

2 particle is calculated by adding them and stored in the 17th and 18th component of uwa .

- The tensors $K_{1,2,3}^{\alpha\beta\mu\nu}$ of the spin-2 Feynman rules are computed.
- The numerator and the denominator of the spin-2 propagator (see Appendix A) are calculated.
- The off-shell tensor current is calculated from the input functions $w1$ and $a2$, the respective Feynman rule and the propagator.
For $UWAXXX_TRIPPM(w1,a2, uwa)$, the corresponding formula is:

$$ywa^{\gamma\delta} = -\frac{B^{\mu\nu\gamma\delta}}{k^2 - m_T^2 + im_T\Gamma_T} \frac{f_7}{\Lambda} c_w K_{1,\alpha\beta\mu\nu} w1^\alpha a2^\beta \quad (4.6)$$

The 16 components of ywa are stored in the first 16 entries of uwa .

The structure of a vertex routine, like $WATXXX_TRIPPM(w1,a2,tc, vertex)$, is analogous, apart from the following differences: An additional input, the tensor function tc of the spin-2 particle, is needed, the momentum of the spin-2 particle does not need to be calculated (as it is already contained in the input tensor function) and the propagator is not needed either. The tensor function tc can be the output of a HELAS routine which calculates an off-shell tensor current, like uwa from $UWAXXX_TRIPPM(w1,a2, uwa)$. The output, $vertex$, is computed from the three input functions and the respective Feynman rule.

For $WATXXX_TRIPPM(w1,a2,tc, vertex)$, the corresponding formula is:

$$vertex = \frac{f_7}{\Lambda} c_w K_{1,\alpha\beta\mu\nu} w1^\alpha a2^\beta ft^{\mu\nu} \quad (4.7)$$

The 16 components of $ft^{\mu\nu}$ are equal to the first 16 entries of tc .

4.4 The different processes: New Feynman diagrams and implementation

In this section, the modifications of the different processes which are relevant for this thesis are presented, together with all the new Feynman diagrams involving spin-2 particles. Whereas the VBF processes for electroweak boson pair production with four leptons in the final state (200, 210, 211, 220 and 230) were already implemented and just had to be enlarged, the VBF process $pp \rightarrow \gamma\gamma jj$ via a spin-2 resonance (240) was created completely new.

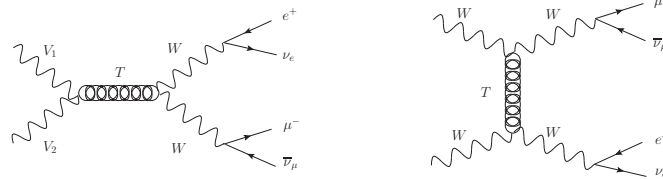
4.4.1 200: $VV \rightarrow e^+ \nu_e \mu^- \bar{\nu}_\mu$

This process, called WPWMjj, is characterized by the four final state leptons $e^+ \nu_e \mu^- \bar{\nu}_\mu$, which emerge from a W^+ and a W^- boson. All off-shell effects to this final state are included. Its leptonic tensor file, toww.F, already contained all the contributing Standard Model diagrams, which are calculated in several subroutines according to the initial bosons, which couple to the initial quark legs. The notation $VV \rightarrow e^+ \nu_e \mu^- \bar{\nu}_\mu$ only denotes the process of the leptonic tensors. In the full process, there are also the two quarks in the initial state and the jets in the final state.

For the process 200, the new Feynman diagrams involving a spin-2 particle are:

Spin-2 singlet and neutral triplet

For the spin-2 singlet particle T , the new diagrams are:



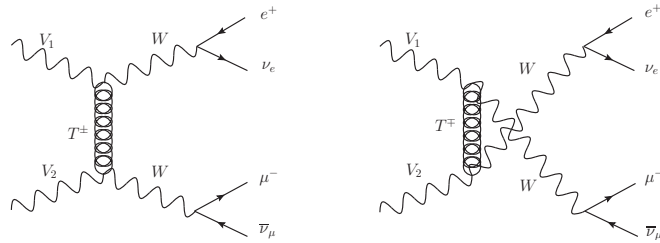
with $V_1, V_2 \cong W^+W^-, \gamma Z, Z\gamma, \gamma\gamma, ZZ$

The Feynman diagrams for the neutral spin-2 triplet are the same as for the singlet particle (just replace T with T^0).

This is a general feature of all the considered processes, as the set of vertices is identical for both particles.

Charged spin-2 triplet

For the charged triplet particles, the new contributions are:



with $V_1, V_2 \hat{=} \gamma Z, Z\gamma, \gamma\gamma, ZZ$

Implementation

In order to implement these new Feynman diagrams, the new file `toww_spin2.F` was created, which is a modification of `toww.F`. There, the subroutines are called `AAtoWW_spin2` instead of `AAtoWW` for example. The new Feynman diagrams were implemented into these subroutines by writing a set of calls of HELAS routines (see the previous section for details). Furthermore, a formfactor (see chapter 5.1, eq. 5.4), which can be multiplied to the subamplitude, was implemented into each subroutine.

These modified subroutines are used for the further calculations in the file `m2s_qqzqq.F` instead of the original ones if the spin-2 switch is set to true.

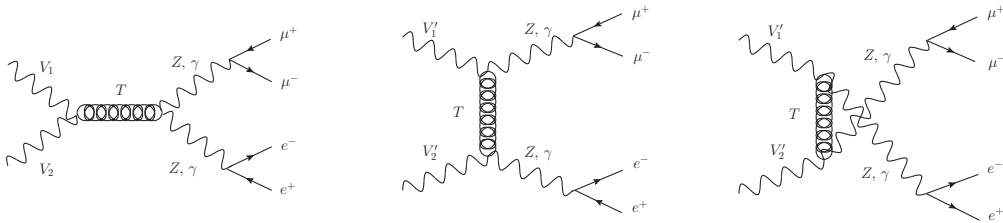
Also the exchange of the order of the initial electroweak bosons is performed there: These subroutines are called twice, with interchange of the two initial bosons, if these bosons are not the same.

For the processes 210, 211, 220 and 230, the procedure is completely analogous to the one described here.

4.4.2 210: $VV \rightarrow e^+ e^- \mu^+ \mu^-$

The modified leptonic tensor file of this process, which is called `ZZjj_ll`, is denoted as `tozz_spin2.F`, its subroutines are called in `m2s_qqzqq.F`, as previously. The new Feynman diagrams are:

Spin-2 singlet and neutral triplet

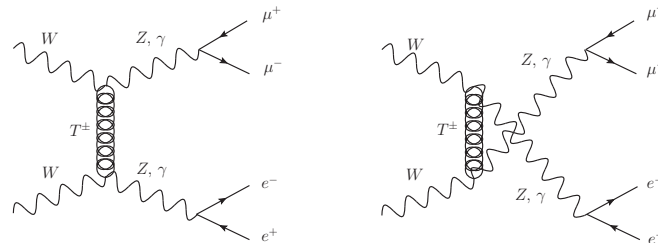


with $V_1, V_2 \hat{=} W^+W^-, \gamma Z, Z\gamma, \gamma\gamma, ZZ$ and $V'_1, V'_2 \hat{=} \gamma Z, Z\gamma, \gamma\gamma, ZZ$.

For the two final bosons, there are always four possible combinations: $ZZ, \gamma\gamma, Z\gamma, \gamma Z$.

Charged spin-2 triplet

Again, for the final bosons, there are the four possible combinations $ZZ, \gamma\gamma, Z\gamma, \gamma Z$, but the initial bosons can only be W^+W^- .

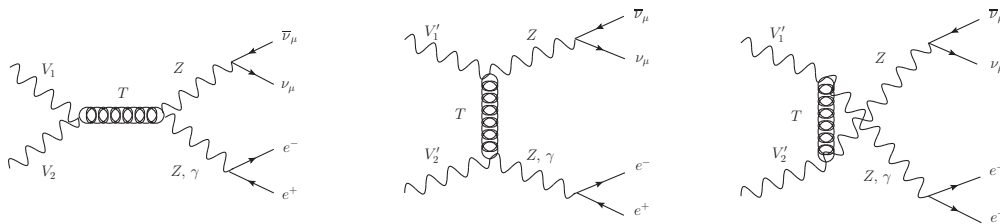


4.4.3 211: $VV \rightarrow e^+ e^- \nu_\mu \bar{\nu}_\mu$

This process, called ZZjj_lnu, uses the same modified leptonic tensor file as 210: tozz_spin2.F and its subroutines are called in m2s.qqzqq.F as well.

There are only half as much new Feynman diagrams as for process 210, because the photon can decay into charged leptons, but not into neutrinos.

Spin-2 singlet and neutral triplet

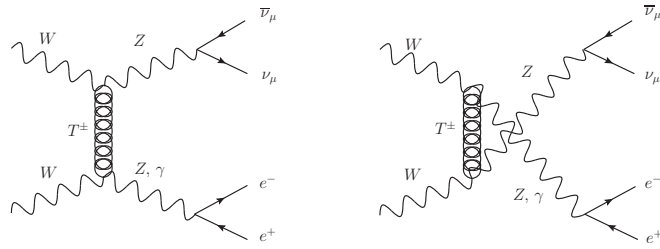


with $V_1, V_2 \hat{=} W^+W^-, \gamma Z, Z\gamma, \gamma\gamma, ZZ$ and $V'_1, V'_2 \hat{=} \gamma Z, Z\gamma, \gamma\gamma, ZZ$

For the two final bosons, there are only two possible combinations: ZZ and $Z\gamma$, instead of four for process 210.

Charged spin-2 triplet

The new diagrams for T^\pm are:

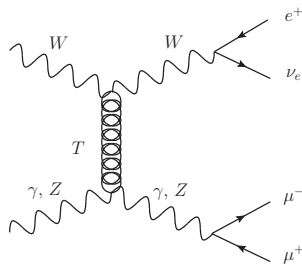


4.4.4 220: $VV \rightarrow e^+ \nu_e \mu^+ \mu^-$

This process is called WPZjj. Its modified leptonic tensor file is denoted as towz_spin2.F, its subroutines are called in m2s_qqwqq.F.

The new Feynman diagrams are:

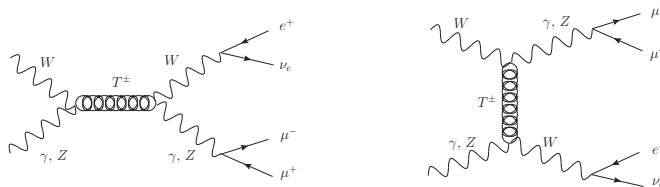
Spin-2 singlet and neutral triplet



There are four possible combinations for the two lower boson lines: ZZ, $\gamma\gamma$, Z γ , γZ .

Charged spin-2 triplet

The new diagrams for T^\pm are:

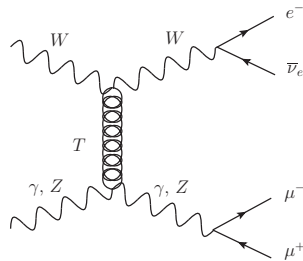


4.4.5 230: $VV \rightarrow e^- \bar{\nu}_e \mu^+ \mu^-$

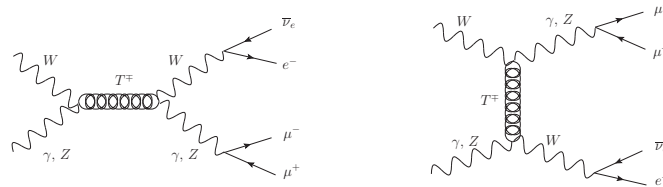
This process, called WMZjj, is very similar to the process 220: The only difference can be found in the final leptons: $e^- \bar{\nu}_e$ instead of $e^+ \nu_e$, which emerge from a W^- instead of a W^+ . Therefore, this process is implemented in the same modified leptonic tensor file, towz_spin2.F and its subroutines are called in m2s_qqwqq.F as well.

Also the Feynman diagrams are analogous:

Spin-2 singlet and neutral triplet



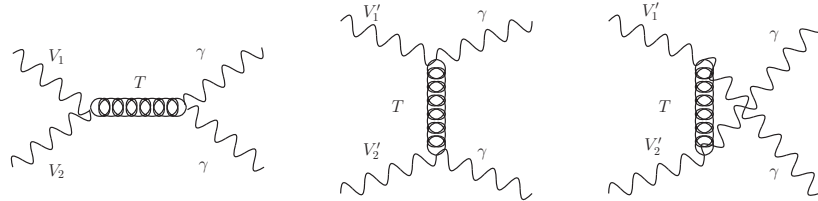
Charged spin-2 triplet



4.4.6 240: $VV \rightarrow \gamma\gamma$

This new process is denoted as AAjj and characterized by two photons in the final state and an intermediate state with a spin-2 particle involved. In contrast to the other processes discussed before, this one does not contain any Standard Model background. The only diagrams that contribute to this processes are the following ones:

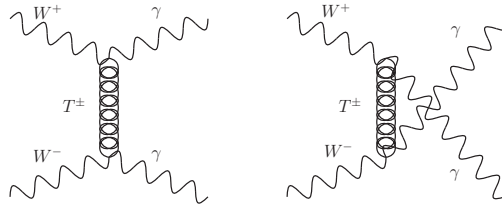
Spin-2 singlet and neutral triplet



with $V_1, V_2 \cong W^+W^-, \gamma Z, Z\gamma, \gamma\gamma, ZZ$ and $V'_1, V'_2 \cong \gamma Z, Z\gamma, \gamma\gamma, ZZ$

Charged spin-2 triplet

For T^\pm , only the following diagrams are possible:



Implementation

To implement this new process, first, its name AAjj and its number 240 were defined in **process.inc**. Furthermore, some new files were created: **spin2toaa.F**, **qqsp2aaqq.F** and **tensorsp2aa.inc**. tensorsp2aa.inc contains a common block of the new variables for the leptonic tensors. The leptonic tensors are calculated from the Feynman diagrams listed above in the file spin2toaa.F, which has a similar structure as other leptonic tensor files and which also provides the opportunity to multiply the leptonic tensors with a formfactor. The subroutines of spin2toaa.F are called in m2s.qqzqq.F, and again, the exchange of the order of the initial electroweak bosons is also performed there: The subroutines are called twice, with interchange of the two initial bosons, if these bosons are not the same. The square of the matrix element of the process is calculated in qqsp2aaqq.F by contracting the leptonic tensors with the hadronic tensors $\mathcal{J}_{q1}^\mu \mathcal{J}_{q2}^\nu$ (see eq. 4.5).

The process 240 can also be used in another way: It includes the opportunity to have a Higgs instead of a spin-2 particle in the leptonic tensor subroutines. Therefore, `spin2toaa.F` contains a second part, which is usually commented out for a normal run of 240 with spin-2 particles. There, two Feynman diagrams are considered which contribute to the leptonic tensors: Their structure is like the left one of the spin-2 singlet case, but with a Higgs instead of T , and with the initial bosons W^+W^- in one diagram and ZZ in the other one. The Higgs boson couples to the photons by an effective dimension-five operator.

There is also another way to simulate the Higgs case: VBF Higgs production multiplied with the photon branching ratio of the Higgs. This is implemented in process 101 (`Hjj_AA`), which was used, but not modified for this thesis.

The comparison of the results of process 101 and the Higgs case of process 240 is also a good way to test the implementation of 240: The two results agree well, some small differences originate from the effective coupling of the Higgs to the photons.

4.5 Input parameters and selection cuts

4.5.1 Input parameters

The following parameters, which can be set in the input file `vbfnlo.dat` (see Appendix C.1), are taken from the 2010 results of the Particle Data Group [22].

The masses of the electroweak bosons are:

$$\begin{aligned} m_W &= 80.399 \text{ GeV} \\ m_Z &= 91.1876 \text{ GeV} \end{aligned}$$

The Fermi constant is:

$$G_F = 1.16637 \cdot 10^{-5} \text{ GeV}^{-2}$$

α and $\sin^2 \theta_W$ are calculated from these by using LO electroweak relations. This is chosen by setting `EWScheme = 3` in `vbfnlo.dat`.

The masses of the leptons and the light quarks are neglected. The top and bottom quark do not contribute to the considered processes.

The chosen PDF set (only at LO, since no NLO calculations were performed) is: **CTEQ6LI** [23].

The factorization scale is set to $\mu_F = Q$, where Q is the momentum transfer between the respective initial and final state quarks.

The present analysis focuses on a Higgs mass of

$$m_H = 120 \text{ GeV.}$$

This is in agreement with constraints from direct searches at LEP and Tevatron. Also a relatively light Higgs around this value is favoured by electroweak precision data.

4.5.2 Selection cuts

A sensible choice of selection cuts is necessary for several reasons: Some basic cuts are needed to render the calculations finite, the detector geometry has to be respected, and the background should be suppressed compared to the signal process.

Therefore, some different sets of cuts can be applied [24]:

1. Inclusive Cuts:

The weakest of the applied constraints are called inclusive cuts and are summarized in the following table:

Cut	VBFNLO Notation
$p_{T,j}^{tag} > 30 \text{ GeV}$	PT_JET_MIN = 30.0d0
$ \eta_j < 4.5$	Y_JET_MAX = 4.5d0
$\Delta R_{jj} > 0.7$	RJJ_MIN = 0.7d0
$p_{T,l} > 20 \text{ GeV}$	PT_L_MIN = 20.0d0
$ \eta_l < 2.5$	Y_L_MAX = 2.5d0
$\Delta R_{lj} > 0.4$	RLJ_MIN = 0.4d0
$m_{ll} > 15 \text{ GeV}$	MLL_MIN = 15.0d0

where η is the rapidity, the index l denotes the final state leptons, *tag* stands for *tagging* (the tagging jets are the two jets

which have the largest transverse momentum) and ΔR is defined as: $\Delta R = \sqrt{(\eta_1 - \eta_2)^2 + (\phi_1 - \phi_2)^2}$.

These cuts are applied to avoid singularities, to respect the accessible rapidity range of the detector and to ensure well-observable isolated particles.

2. VBF cuts:

Vector boson fusion events have some characteristic features, which can be used to suppress the background: The two tagging jets are located in the far forward region of the detector and have a large invariant mass and rapidity gap between them, whereas the final state leptons lie in the central rapidity range between the two jets.

Therefore, the VBF cuts are chosen as:

Cut	VBFNLO Notation
$\eta_{j,min}^{tag} < \eta_l < \eta_{j,max}^{tag}$	LRAPIDGAP = true
$\Delta\eta_{jj} > 4$	ETAJJ_MIN = 4.0d0
$\eta_{j1}^{tag} \times \eta_{j2}^{tag} < 0$	YSIGN = true
$m_{jj} > m_{jj}^{min}$	MDIJ_MIN (=5.0d2 or 1.0d3)

where MDIJ_MIN = 1000 GeV for process 200 (WPWMjj) and 500 GeV for all other processes considered in this thesis.

3. Cuts on the invariant mass of the final state lepton system:

In order to study distributions of a spin-2 resonance in the processes with four leptons in the final state (200, 210, 211, 220, 230), it is convenient to cut off all the contributions which do not stem from this resonance.

Therefore, a minimal and a maximal invariant mass of the final state lepton system can be required. The corresponding VBFNLO notation of these cuts is MLEP_MIN and MLEP_MAX. The values of MLEP_MIN and MLEP_MAX are adjusted to the width of the considered resonance.

In addition to these sets of cuts, some other cuts are always applied:

A maximal rapidity for the partons: Y_P_MAX = 5.0d0 and some photon cuts: A maximal photon rapidity similar to the maximal lepton rapidity (see

inclusive cuts): $Y_G\text{MAX} = 2.5d0$, a minimal transverse momentum of the photons: $PT_G\text{MIN} = 20.0d0$ (similar to $PT_L\text{MIN}$ of the inclusive cuts), a minimal photon-photon R separation: $RGG\text{MIN} = 0.4d0$, a minimal jet-photon R separation: $RJG\text{MIN} = 0.4d0$ and a photon isolation cut: $PHISOLCUT = 0.7d0$ with an efficiency: $EFISOLCUT = 1.0d0$.

All these cuts can be set in the VBFNLO data file **cuts.dat**, see Appendix C.2.

5 Results

5.1 Unitarity violation and formfactor in longitudinal WW scattering

A physical theory has to preserve unitarity. However, as the present model for the interaction of spin-2 particles with electroweak bosons is an effective theory, which is a low-energy approximation and can only be used up to a certain energy scale, it is no surprise that the amplitudes increase with the centre of mass energy and therefore the theory violates unitarity at a certain scale.

For a detailed treatment, a partial wave analysis is a useful tool. It is applied to the scattering process of two longitudinal W bosons.

According to Ref. [25], the partial wave decomposition of the matrix element for fixed helicity combinations is given by:

$$\mathcal{M} = 16\pi \sum_j (2j+1) a_{\lambda\mu}^j d_{\lambda\mu}^j(\theta) \quad (5.1)$$

where $\lambda(\mu)$ is the helicity difference between the initial (final) bosons and $d_{\lambda\mu}^j(\theta)$ are the Wigner d-functions which are given in appendix E.

The orthogonality of the d-functions (eq. E.3) can be used to obtain the coefficients $a_{\lambda\mu}^j$: Multiplying eq. (5.1) by $d_{\lambda\mu}^{j'}(\theta)$, integrating over $\cos\theta$ and inserting eq. (E.3) yields:

$$a_{\lambda\mu}^j = \frac{1}{32\pi} \int_{-1}^1 \mathcal{M} d_{\lambda\mu}^j(\theta) d\cos\theta \quad (5.2)$$

Unitarity of the S-matrix implies [26]:

$$|Re(a_{\lambda\mu}^j)| \leq 0.5 \quad (5.3)$$

The partial wave analysis of longitudinal WW scattering was performed by using a FORTRAN-program whose original version was written by C. Englert [7] and which was modified for the present thesis: It uses HELAS routines to calculate the matrix element and the routine **gaussint** for the integration over θ .

For the spin-2 case, there are two Feynman diagrams which contribute to the WW scattering for the singlet case and the same ones for the triplet case

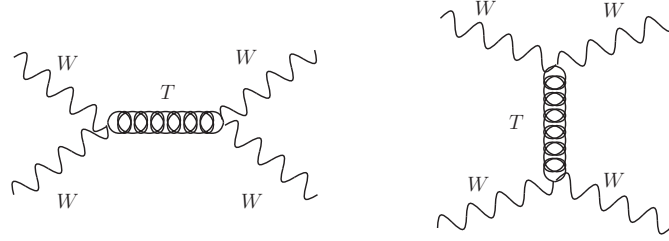


Figure 5.1: Spin-2 Feynman diagrams of WW scattering

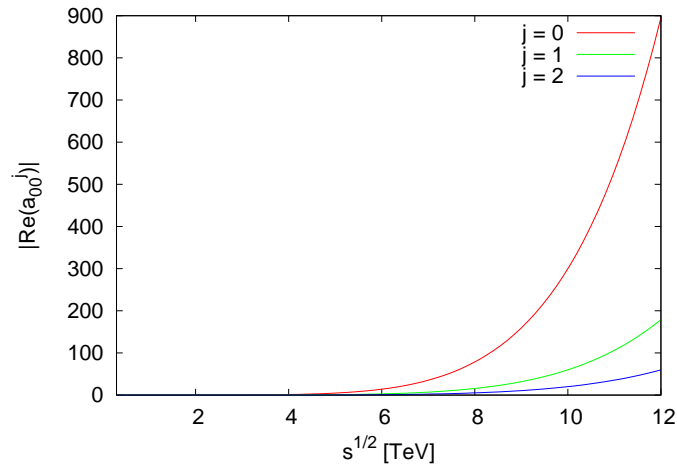


Figure 5.2: Coefficients of the partial wave analysis in longitudinal WW scattering for the spin-2 diagrams of fig. 5.1

(fig. 5.1).

Of course, the values of the coefficients $a_{\lambda\mu}^j$ depend strongly on the chosen parameters of the spin-2 model.

The first coefficients of the partial wave decomposition in longitudinal WW scattering with the two spin-2 singlet graphs of fig. 5.1 are shown in fig. 5.2 for the following parameters: $f_1 = f_2 = f_5 = 1$, $f_{i \neq 1,2,5} = 0$, $\Lambda = 200$ TeV, $m_T = 120$ GeV, $\text{brat} = 1$. With these parameters, the VBF photon pair-production process yields a cross section which is roughly the same for a Higgs and a spin-2 particle (see table 5.1).

a_{00}^0 gives the major contribution, so it determines the unitarity bound: For the

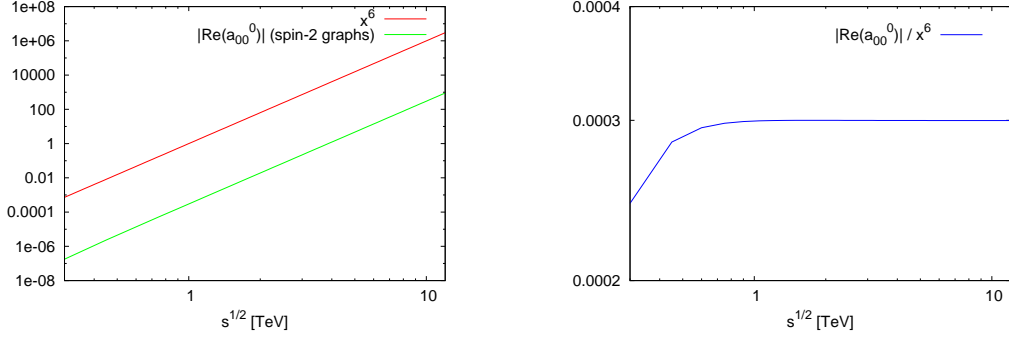


Figure 5.3: Energy dependence of $|Re(a_{00}^0)|$. Left hand side: Comparison to x^6 , right hand side: Ratio of $|Re(a_{00}^0)|$ and x^6 .

given set of parameters, unitarity is violated above around 3.4 TeV (see fig. 5.4).

The left hand side of fig. 5.3 depicts the energy dependence of this coefficient: In the double logarithmic plot, the slope characterizes the exponent of the functions, so one can see that $|Re(a_{00}^0)| \propto s^3$ (or $\propto E^6$, respectively) and therefore $\mathcal{M} \propto E^6$ for the spin-2 diagrams. As illustrated by the right hand side of fig. 5.3, this is a very good approximation for high energies above around 1 TeV.

In fig. 5.4, the behavior of $|Re(a_{00}^0)|$ is compared to the Standard Model longitudinal WW scattering: There, unitarity violation is only avoided due to the Higgs boson.

There is a possibility to evade unitarity violation for the present spin-2 model as well: The introduction of a formfactor, which is multiplied to the amplitudes and yields a suppression of high energies.

The chosen parametrization of this formfactor is:

$$f(q_1^2, q_2^2, p_{sp2}^2) = \left(\frac{\Lambda_{ff}^2}{|q_1^2| + \Lambda_{ff}^2} \cdot \frac{\Lambda_{ff}^2}{|q_2^2| + \Lambda_{ff}^2} \cdot \frac{\Lambda_{ff}^2}{|p_{sp2}^2| + \Lambda_{ff}^2} \right)^{n_{ff}} \quad (5.4)$$

where q_1^2 and q_2^2 are the invariant masses of the initial electroweak bosons and p_{sp2}^2 is the invariant mass of the sum of the initial boson momenta, equivalent to that of a s-channel spin-2 particle.

The energy scale Λ_{ff} and the exponent n_{ff} are free parameters.

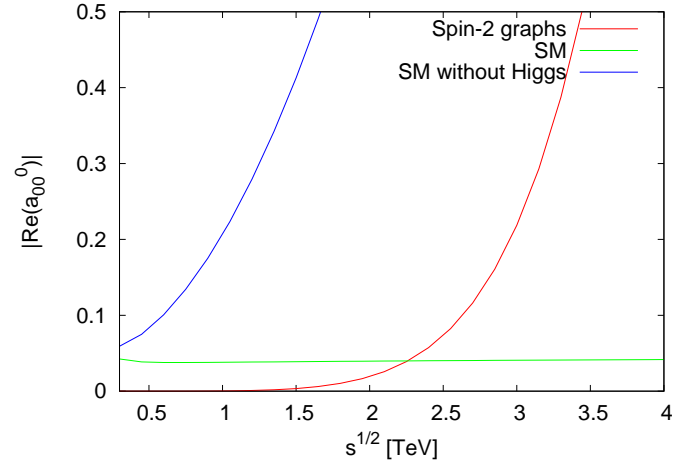


Figure 5.4: Unitarity violation: Comparison with the Standard Model

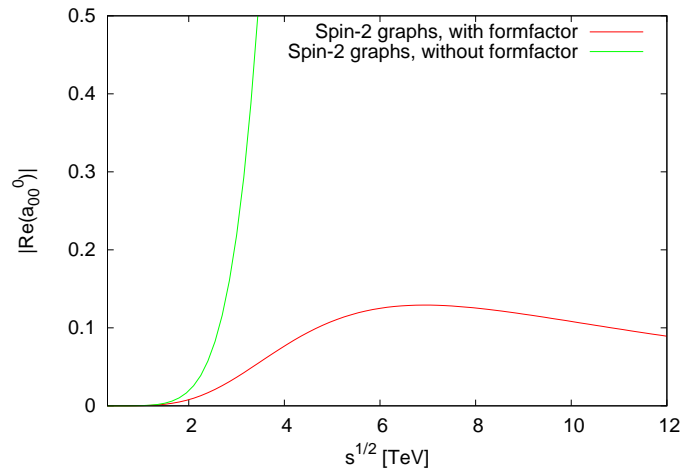


Figure 5.5: Influence of the formfactor for $\Lambda_{ff} = 4 \text{ TeV}$ and $n_{ff} = 4$

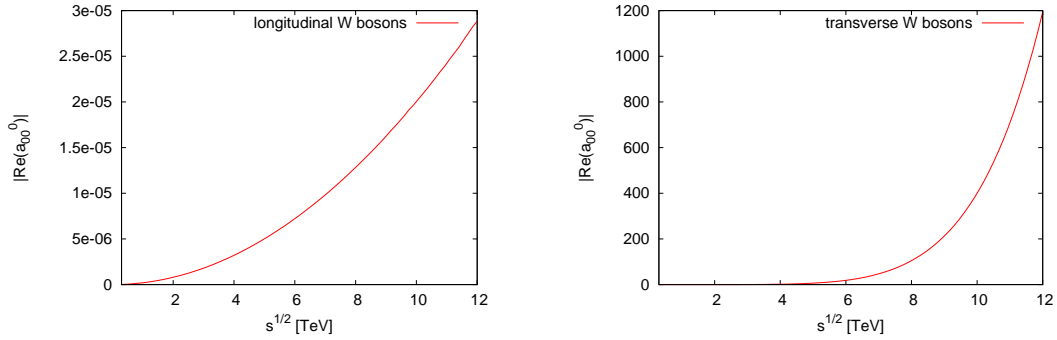


Figure 5.6: Left hand side: $|Re(a_{00}^0)|$ for $f_5 = 0$ for longitudinal W bosons, right hand side: for transverse W bosons

The influence of this formfactor on the energy dependence of $|Re(a_{00}^0)|$ is illustrated in fig. 5.5 for $\Lambda_{ff} = 4$ TeV and $n_{ff} = 4$.

So with a suitable choice of Λ_{ff} and n_{ff} , unitarity is preserved.

However, this is only one argument for the introduction of this formfactor. Another even more important one concerns the distribution of transverse momenta. This will be discussed in section 5.2.2.

A further analysis of the behavior of different couplings reveals that unitarity violation in longitudinal WW scattering stems from the coupling f_5 , whereas the contribution of the other couplings is insignificant.

This is illustrated by fig. 5.6: The left hand side shows the behavior of $|Re(a_{00}^0)|$ in longitudinal WW scattering for the parameter settings $f_1 = f_2 = 1$, $f_{i \neq 1,2} = 0$, $\Lambda = 200$ TeV, $m_T = 120$ GeV, $brrat = 1$, which is the same as before, except for the absence of f_5 . The right hand side shows the same for transverse W bosons.

Fig. 5.6 demonstrates that, in contrast to f_5 (see fig. 5.4), f_1 and f_2 do not lead to unitarity violation for longitudinal W bosons, whereas for transverse ones, they do.

There is another interesting feature which is observable in the partial wave analysis of WW scattering: As explained in Ref. [27], the numerator of the spin-2 propagator (eq. A.7) acts as a projector on the on-shell particle ($k^2 = m^2$) if m_T^2 is replaced with k^2 in eq. A.7. Therefore, it is proportional to $d_{\lambda\mu}^2$.

If the longitudinal W bosons are chosen as off-shell particles in order to get an on-shell spin-2 particle and m_T^2 is replaced with k^2 in the numerator of the

propagator, one finds that for the resonance ($s^{1/2} = 120$ GeV) only a_{00}^2 contributes, the other coefficients vanish.

Note that this feature is visible in the imaginary part, not in the real part of a_{00}^2 , since for the resonance, the denominator of the propagator is purely imaginary.

In the following sections of this chapter, the formfactor of eq. 5.4 will be used to preserve unitarity and to suppress unphysical high-energy contributions. Furthermore, in case of the photon pair-production process, it will be used to adjust the transverse momentum distributions of a spin-2 resonance to those of a Higgs (see section 5.2.2). Thereby, the absence of a formfactor can be understood as the limiting case of $\Lambda_{ff} \rightarrow \infty$.

5.2 Photon pair-production in Vector Boson Fusion via Higgs and Spin-2 resonances

In this section, the VBFNLO process 240 (see section 4.4.6), which concerns photon pair-production in vector boson fusion via Higgs and spin-2 resonances, is analyzed. First, the total cross sections together with their errors are presented for different cases and parameter settings. Afterwards, p_T distributions are analyzed and the relevance of the formfactor, which was introduced in section 5.1, is illustrated. Then, the resonance peak of the Higgs and the spin-2 resonance are compared and the task of the spin-2 branching ratio parameters (see Appendix B) is elucidated. Finally, the most important aspect of this analysis is presented: The various angular distributions.

The main issue of all these facets of the analysis is the comparison of a Higgs and a spin-2 resonance. Additionally, different cuts and parameter settings are investigated and the spin-2 singlet is compared to the spin-2 triplet case.

If there are no other specifications, the analysis is executed with the following settings (see Appendix C1, C3):

- The VBFNLO calculation is performed with 4 iterations and 2^{24} points.
- The mass of the Higgs and the spin-2 particles are chosen as 120 GeV.
- All the spin-2 branching ratio parameters are set to 1.
- Only the s-channel diagrams of the Feynman diagrams presented in 4.4.6 are considered (see 5.2.3).
- In order to obtain cross sections comparable to the Higgs case (see table 5.1), the usual spin-2 parameter settings are:
Spin-2 singlet, without formfactor: $f_1 = f_2 = f_5 = 1, f_{i \neq 1,2,5} = 0, \Lambda = 200 \text{ TeV}$,
spin-2 singlet, with formfactor: $f_1 = f_2 = f_5 = 1, f_{i \neq 1,2,5} = 0, \Lambda = 20 \text{ TeV}, \Lambda_{ff} = 400 \text{ GeV}, n_{ff} = 3$,
spin-2 triplet, without formfactor: $f_6 = f_7 = 1, f_{i \neq 6,7} = 0, \Lambda = 50 \text{ TeV}$,
spin-2 triplet, with formfactor: $f_6 = f_7 = 1, f_{i \neq 6,7} = 0, \Lambda = 8 \text{ TeV}, \Lambda_{ff} = 400 \text{ GeV}, n_{ff} = 3$.

The formfactor is used both for the preservation of unitarity (see section 5.1) and in order to adjust the p_T distributions of a spin-2 resonance to those of the Higgs, which will be discussed in section 5.2.2.

- For figures which compare different values of coupling parameters, the complete parameter settings can be found in table 5.1. There, couplings f_i which are not given explicitly are set to zero and the parameters of the formfactor are $\Lambda_{ff} = 400 \text{ GeV}$, $n_{ff} = 3$.
- The distributions are determined in the laboratory frame.

In order to investigate possible effects of a finite detector resolution, a smearing of the energy and the transverse momenta of the final state photons and jets according to a Gaussian distribution was performed by using an in-house routine. The energy of each jet is smeared according to a parametrization which is based on a CERN CMS study [28]:

$$\frac{\Delta E_j}{E_j} = \left(\frac{a}{E_{Tj}} \oplus \frac{b}{\sqrt{E_{Tj}}} \oplus c \right) \quad (5.5)$$

The individual terms are added in quadrature. E_{Tj} denotes the transverse energy of the jet. The parameters a, b and c depend on the rapidity η_j of the jet in the following way:

	a	b	c
$ \eta_j < 1.4$	5.6	1.25	0.033
$1.4 < \eta_j < 3$	4.8	0.89	0.043
$ \eta_j > 3$	3.8	0	0.085

For the photons, an energy resolution of 2% is assumed:

$$\frac{\Delta E_\gamma}{E_\gamma} = 2\% \quad (5.6)$$

The x and y components of the transverse momenta are smeared in a similar way.

However, it turned out that this smearing hardly influences the studied distributions. Therefore, the results which are presented here were performed without smearing.

5.2.1 Cross sections

Table 5.1 gives an overview of the cross sections and the corresponding errors computed by VBFNLO for the photon pair-production process (process 240) for different scenarios and different sets of parameters. The given errors are statistical errors from the Monte Carlo integration.

Process and parameters	Cross section [fb]	Error [fb]
Higgs ($m_H = 120$ GeV), inclusive cuts	4.0978	0.0017
Higgs ($m_H = 120$ GeV), inclusive + vbf cuts	2.1859	0.00105
Spin-2 singlet, without formfactor, $f_1 = f_2 = f_5 = 1$, $\Lambda = 200$ TeV, inclusive cuts	2.9301	0.0042
Spin-2 singlet, without formfactor, $f_1 = f_2 = f_5 = 1$, $\Lambda = 200$ TeV, inclusive + vbf cuts	0.4870	0.0008
Spin-2 singlet, with formfactor, $f_1 = f_2 = f_5 = 1$, $\Lambda = 20$ TeV, inclusive cuts	4.5908	0.0022
Spin-2 singlet, with formfactor, $f_1 = f_2 = f_5 = 1$, $\Lambda = 20$ TeV, inclusive + vbf cuts	2.5571	0.00135
Spin-2 singlet, with formfactor, $f_1 = f_2 = 1$, $\Lambda = 20$ TeV, inclusive cuts	4.0376	0.0019
Spin-2 singlet, with formfactor, $f_1 = 2$, $f_2 = f_5 = 1$, $\Lambda = 27$ TeV, inclusive cuts	4.9627	0.0023
Spin-2 singlet, with formfactor, $f_1 = 1$, $\Lambda = 10$ TeV, inclusive cuts	4.7081	0.0022
Spin-2 singlet, with formfactor, $f_2 = 1$, $\Lambda = 10$ TeV, inclusive cuts	4.6184	0.0022

Spin-2 singlet, with formfactor, $f_1 = -1, f_2 = f_5 = 1, \Lambda = 20 \text{ TeV}$, inclusive cuts	2.0242	0.00096
Spin-2 singlet, with formfactor, $f_2 = -1, f_1 = f_5 = 1, \Lambda = 20 \text{ TeV}$, inclusive cuts	1.3614	0.00066
Spin-2 singlet, with formfactor, $f_5 = -1, f_1 = f_2 = 1, \Lambda = 20 \text{ TeV}$, inclusive cuts	3.6160	0.0017
Spin-2 triplet, without formfactor, $f_6 = f_7 = 1, \Lambda = 50 \text{ TeV}$, inclusive cuts	4.5134	0.0066
Spin-2 triplet, with formfactor, $f_6 = f_7 = 1, \Lambda = 8 \text{ TeV}$, inclusive cuts	4.4898	0.0021
Spin-2 triplet, with formfactor, $f_7 = 1, \Lambda = 8 \text{ TeV}$, inclusive cuts	4.4461	0.0021
Spin-2 triplet, with formfactor, $f_6 = 1, f_7 = -1, \Lambda = 8 \text{ TeV}$, inclusive cuts	4.5925	0.0021

Table 5.1: Total cross sections and errors for process 240

The cross sections are invariant under a global change of the sign of the coupling parameters.

Including the parameters f_3 and f_4 (or, more precisely, taking $f_1 = f_2 = f_3 = f_4 = f_5 = 1$ instead of $f_1 = f_2 = f_5 = 1$) has hardly any effect: The distributions look similar and up to the 11th decimal place, the cross section is the same. If f_3 and f_4 are the only non-vanishing couplings, the cross section is not defined, because in this case, the width of the spin-2 resonance is always zero (see appendix B).

A similar effect appears if only f_5 or f_6 are taken. Since for the present analysis of this process, the masses of the spin-2 particles are set to 120 GeV, the spin-2 particles are too light to decay into WW- or ZZ- pairs, so the partial widths which contain these coupling parameters only contribute to the total width via off-shell effects. These are not considered here.

5.2.2 p_T distributions and formfactor

On the left hand side of fig. 5.7, the distribution of the transverse momentum (p_T) of a final state photon is shown for the spin-2 singlet case, the right hand side depicts the same distribution for the Higgs case. In both cases, inclusive cuts are applied.

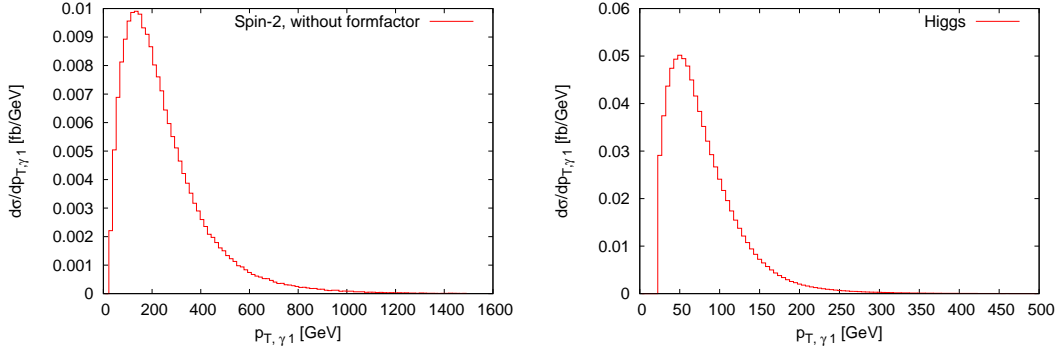


Figure 5.7: Transverse momentum of a final state photon (left hand side: Spin-2 singlet (without formfactor), right hand side: Higgs)

Although the shape of these p_T distributions looks similar, the p_T scale is very different: The transverse momentum of the photon is much higher if it is produced by a spin-2 particle then in the case of the production of a Higgs. So one could think that such p_T distributions provide a nice opportunity to distinguish between a Higgs and a spin-2 particle.

However, it is a little more complicated: The p_T distributions can be understood by looking at the spin-2 propagator: There, the momentum of the spin-2 particle appears in the numerator (which is not the case for the Higgs). This leads to high values of p_T . So, the p_T distribution is not really determined by the spin of the resonance, but it is a feature of the propagator structure.

Furthermore, if differences between the Higgs and the spin-2 resonance are found in the angular distributions, it can also be argued that these differences could result from the particular structure of the propagator and not from the different spin.

However, there is a nice tool to avoid this: The formfactor, which was introduced in section 5.1 (eq. 5.4). By adjusting the parameters of this formfactor, p_T distributions can be modulated such that they are almost similar for the spin-2 and the Higgs case.

To illustrate this effect, fig. 5.8 shows a comparison of the p_T distributions

of a final state photon for the Higgs case, the spin-2 singlet case without a formfactor and with a formfactor ($\Lambda_{ff} = 400$ GeV, $n_{ff} = 3$).

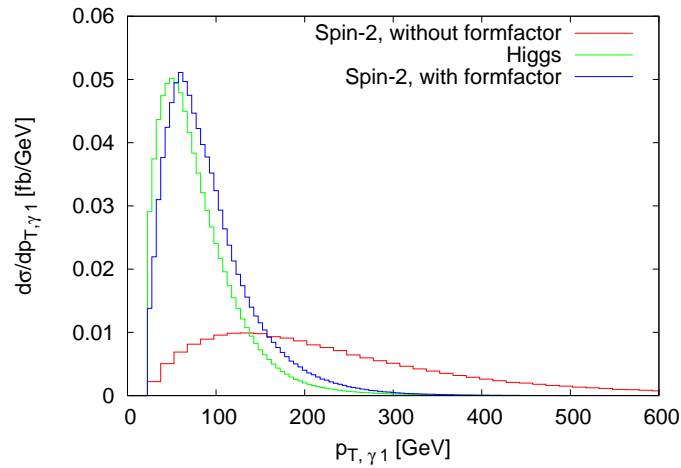


Figure 5.8: Transverse momentum of a final state photon

These distributions look identical for the other final state photon because of Bose symmetry.

Furthermore, the same features emerge for other p_T distributions as well: Fig. 5.9 shows the p_T distribution of the jet with the largest transverse momentum. The parameters of the formfactor are the same as before.

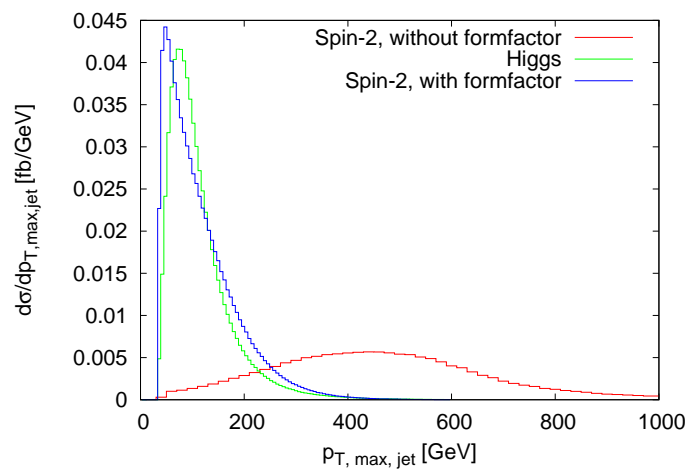


Figure 5.9: p_T of the jet with the largest transverse momentum

Although the differences between the Higgs case and the spin-2 case without formfactor are even more grave for this distribution than for the photon p_T distribution, it is possible to adjust them by using the same parameters of the formfactor.

So, even if the LHC would find p_T distributions which look like the ones of the Higgs, this would not be a proof for a Higgs resonance, they could originate from a spin-2 resonance with an adequate formfactor as well.

A similar effect has also been investigated concerning anomalous Higgs couplings [29]. For such couplings, the p_T values of the jet with the largest transverse momentum are higher than those of the SM Higgs as well. However, the distribution can also be adjusted to the SM case by using a formfactor.

The p_T distributions depend slightly on the spin-2 coupling parameters, which is illustrated exemplarily by fig. 5.10 for the $p_{T,max,jet}$ distribution of a spin-2 resonance with formfactor ($\Lambda_{ff} = 400$ GeV, $n_{ff} = 3$) and inclusive cuts for three different spin-2 singlet parameter settings.

The p_T distributions of the spin-2 triplet case can be adjusted to the Higgs case with the same formfactor settings, which is also depicted by fig 5.10.

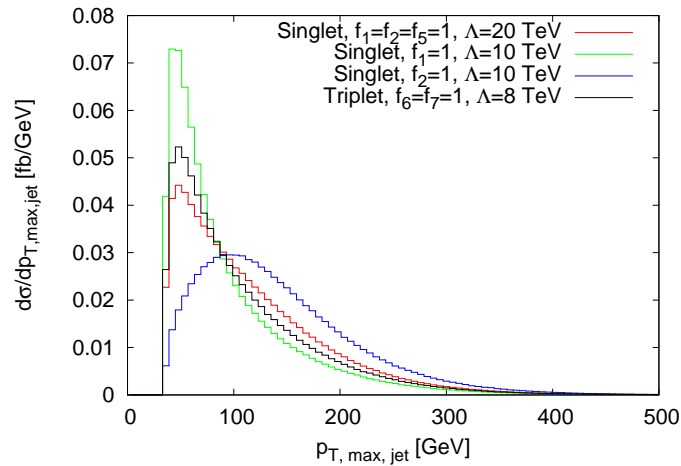


Figure 5.10: $p_{T,max,jet}$, spin-2 singlet and triplet with formfactor for different coupling parameters, inclusive cuts

Other p_T distributions depend on the coupling parameters in a similar way.

5.2.3 Resonance peak, width and branching ratio

Fig. 5.11 depicts the distribution of the invariant mass of the final state photon system with inclusive cuts. The red line of this diagram illustrates the Higgs resonance peak. In order to see the shape of the peak, the narrow width approximation, which is usually applied in VBFNLO for this process, is switched off, which hardly influences the cross section and the various distributions. With a width of 3.265 MeV, the Higgs resonance is indeed very narrow.

The spin-2 resonance, however, is even more narrow: For the singlet case, with a formfactor, inclusive cuts and the usual settings of the parameters, the cross section is comparable to the one of the Higgs case, but the width of the resonance is only 0.0172 MeV (for a branching ratio $b_{\text{rrat}} = 1$).

For these settings, the spin-2 resonance is shown on the left hand side of fig. 5.12. For the green line, only the s -channel diagrams of the Feynman diagrams (section 4.4.6) are considered, whereas for the red line, all the diagrams were included.

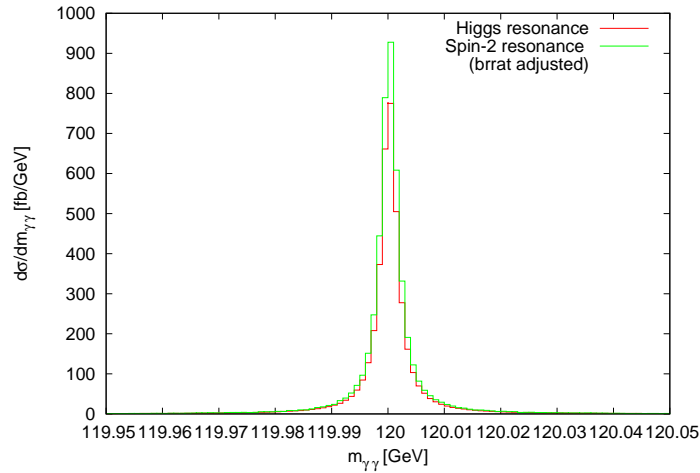


Figure 5.11: $m_{\gamma\gamma}$, spin-2 singlet with adjusted parameters ($b_{\text{rrat}} = 0.075$, $\Lambda = 5.32$ TeV) compared to Higgs (inclusive cuts)

Near the resonance, the relative deviation between the two lines (right hand side of fig. 5.12) is insignificant. Outside the mass range of fig. 5.12, there are no other contributions from none of the diagrams. In addition, including or discarding the non-resonant diagrams hardly influences the cross section and

the other distributions. This is also the case if no formfactor, which could suppress possibly existing high-energy contributions, is applied. Therefore, the non-resonant diagrams are discarded for the rest of the analysis of this process.

As elucidated in appendix B, the width of a spin-2 resonance can be varied by changing the branching ratio (called $brrat$ for the singlet case), which is a free parameter. By changing $brrat$ and Λ simultaneously, it is possible to adjust the width of the spin-2 resonance to the one of the Higgs without changing the cross section too much (one could also change the f_i separately, but this is not necessary).

This is illustrated by the green line of fig. 5.11: For $\Lambda = 5.32$ TeV, $brrat = 0.075$ and the other parameters as usual, the width of the spin-2 singlet resonance is 3.24 MeV and the cross section is 4.866 fb. Both of these values are comparable to the Higgs results. The other distributions are not influenced by these changes.

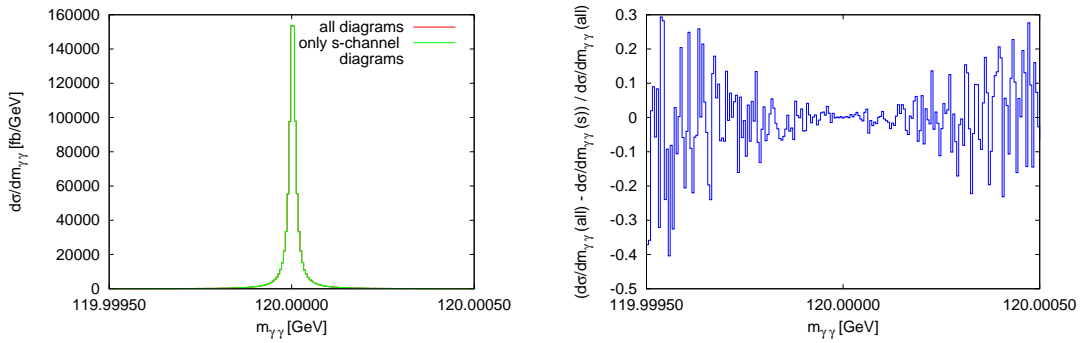


Figure 5.12: Left hand side: $m_{\gamma\gamma}$, spin-2 singlet resonance, inclusive cuts, all Feynman diagrams included (red line) and only s-channel diagrams (green line), right hand side: relative deviation between both lines

So, similar to the argumentation for the p_T distributions, a width of a resonance like the one of fig. 5.11 is not a proof for a Higgs resonance. It can also be a spin-2 resonance with adequate parameters.

However, the details of the resonance peak which are discussed in this section cannot be observed at the LHC, since the resolution of the detectors CMS and ATLAS is roughly 2 GeV for the $m_{\gamma\gamma}$ distribution.

5.2.4 Angular distributions

In this section, various angular distributions are presented. They are compared for a Higgs and a spin-2 resonance and for different spin-2 settings.

Note that all the presented figures include a normalization factor $1/\sigma$.

η_{jets}

A first angular distribution which is typically analyzed for a vector boson fusion process is the rapidity of the tagging jets. Fig. 5.13 and 5.14 show the jet-rapidity distribution, averaged over the two jets, for the three cases Higgs, spin-2 singlet with and without formfactor. For fig. 5.13, only inclusive cuts are applied, whereas for fig. 5.14, vector boson fusion cuts are added.

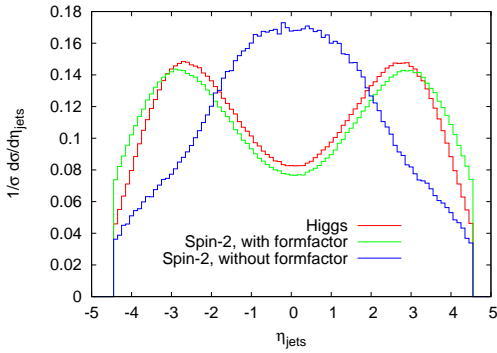


Figure 5.13: Jet-rapidity, averaged over the two jets, inclusive cuts

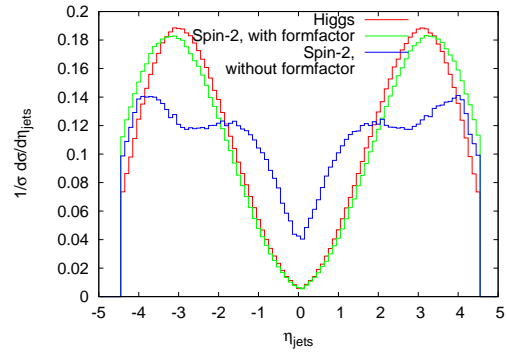


Figure 5.14: Jet-rapidity, averaged over the two jets, inclusive + vbf cuts

While, even if no vbf cuts are applied, the distributions for the Higgs and the spin-2 case with formfactor are both characterized by a rapidity gap which is typical for vector boson fusion processes, the distribution for the spin-2 resonance without formfactor looks different without vbf cuts. Since the momenta of the initial electroweak bosons appear in the Feynman rules (see section 3.1.2) and the numerator of the spin-2 propagator contains the momentum of the spin-2 particle, high p_T values of the jets are preferred if no formfactor is applied (see section 5.2.2, fig. 5.9). This also leads to a rapidity distribution where central jets are preferred.

The distribution of the Higgs and the spin-2 case with formfactor are rather little affected by additional vbf cuts, but the spin-2 distribution without formfactor changes significantly, as the vbf cuts enforce a large rapidity gap, which is not there in the first place.

Furthermore, the jet-rapidity distribution depends slightly on the spin-2 coupling parameters, which is illustrated by fig 5.15.

As shown in fig. 5.16, the jet-rapidity distribution of the spin-2 triplet case with formfactor resembles the singlet case with formfactor for the coupling parameters $f_1 = 2, f_2 = f_5 = 1, f_{i \neq 1,2,5} = 0$. Different settings of the triplet couplings hardly influence the distribution, since the contribution of f_6 is negligible. In fact, this is the case for all the considered angular distributions. A similar effect also appears for the triplet distributions without formfactor.

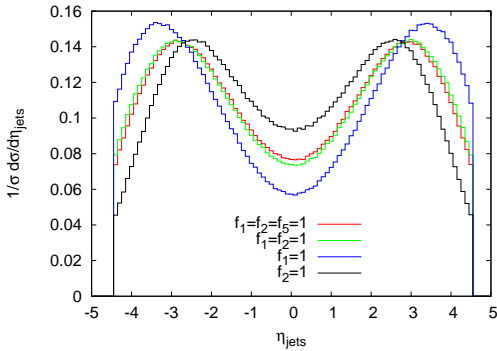


Figure 5.15: jet-rapidity, averaged over the two jets, spin-2 singlet with formfactor, inclusive cuts, different coupling parameters

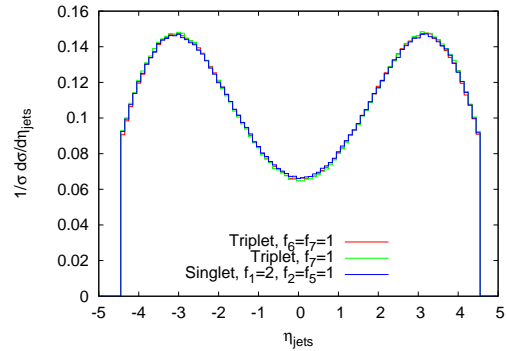


Figure 5.16: jet-rapidity, averaged over the two jets, spin-2 singlet and triplet with formfactor, inclusive cuts

These figures illustrate that the jet-rapidity is not a characteristic of the spin of the resonance, but it depends on kinematics. Similar jet-rapidity distributions for the Higgs and the spin-2 resonance correspond to similar distributions of transverse momenta, which are adjusted by the formfactor.

Therefore, this distribution is not suitable for a distinction between a Higgs and a spin-2 resonance.

Other rapidity distributions and rapidity differences both for jets and photons do not reveal any characteristics which depend on the spin of the resonance either.

$\Delta\Phi_{\gamma\gamma}$

Another angular distribution which can be investigated for this process is the azimuthal angle difference of the two final state photons, $\Delta\Phi_{\gamma\gamma}$.

This distribution is shown in fig. 5.17 for the Higgs case, in fig. 5.18 for

the spin-2 singlet case without formfactor and fig. in 5.19 for the spin-2 singlet case with formfactor. All three distributions are generated both for inclusive and for inclusive + vbf cuts.

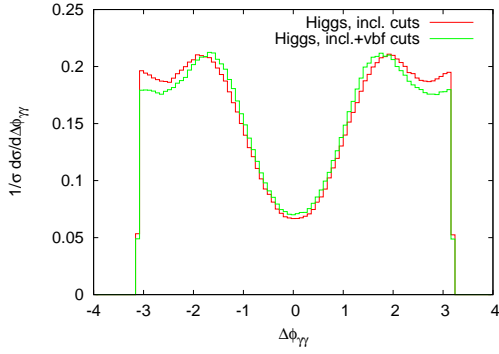


Figure 5.17: $\Delta\Phi_{\gamma\gamma}$, Higgs

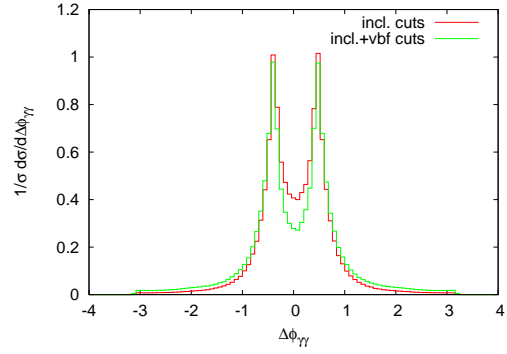


Figure 5.18: $\Delta\Phi_{\gamma\gamma}$, spin-2 singlet, without formfactor

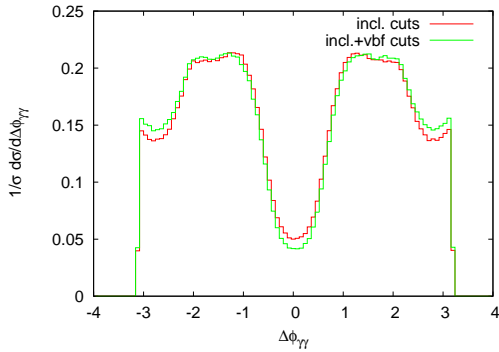


Figure 5.19: $\Delta\Phi_{\gamma\gamma}$, spin-2 singlet, with standard formfactor

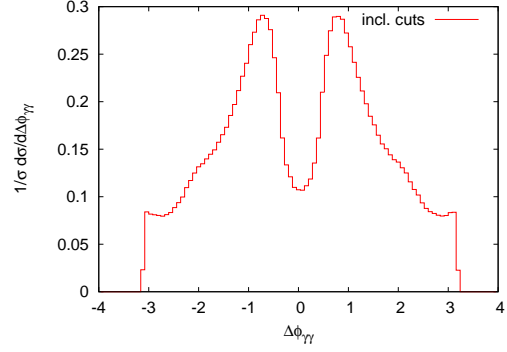


Figure 5.20: $\Delta\Phi_{\gamma\gamma}$, spin-2 singlet, with formfactor, $\Lambda_{ff} = 700$ GeV, $n_{ff} = 4$

Obviously, there is hardly any difference between the two sets of cuts.

However, the $\Delta\Phi_{\gamma\gamma}$ -distribution is very sensitive to the formfactor. Whereas the spin-2 distribution without formfactor looks very different from the one of the Higgs, fig. 5.19 rather resembles the Higgs case.

This dependence on the formfactor is further exemplified by fig. 5.20, whose settings are similar to those of fig. 5.19 (with inclusive cuts), except for

the parameters of the formfactor: They are chosen as $\Lambda_{ff} = 700$ GeV, $n_{ff} = 4$.

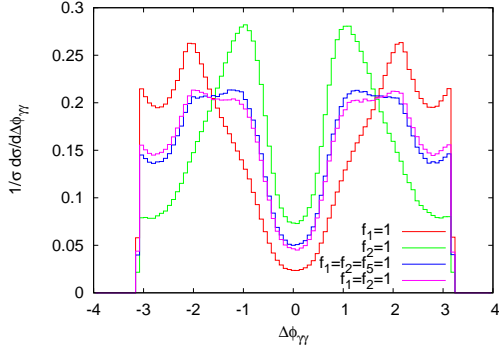


Figure 5.21: $\Delta\Phi_{\gamma\gamma}$, spin-2 singlet, with formfactor, inclusive cuts, different coupling parameters

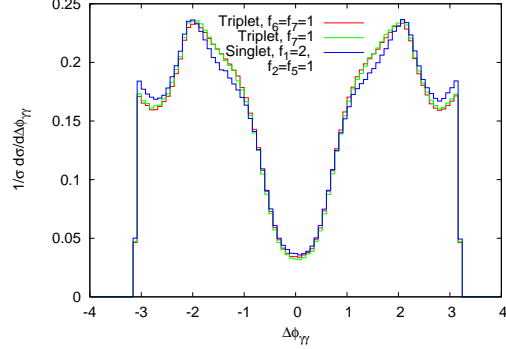


Figure 5.22: $\Delta\Phi_{\gamma\gamma}$, spin-2 singlet and triplet, with formfactor, inclusive cuts

These figures illustrate the fact that the $\Delta\Phi_{\gamma\gamma}$ -distribution, which is measured in the laboratory frame, rather depends on kinematics than on the spin of the resonance: The large difference between the Higgs case and the spin-2 case without formfactor corresponds to the differences of the p_T distributions (see section 5.2.2). The formfactor adjusts the p_T -distributions of the spin-2 and the Higgs resonance, so it also adjusts the $\Delta\Phi_{\gamma\gamma}$ -distribution.

In addition, the $\Delta\Phi_{\gamma\gamma}$ -distribution depends strongly on the spin-2 coupling parameters. This dependence is illustrated by fig. 5.21 for the spin-2 singlet case with standard formfactor.

As for the jet-rapidity distribution, the $\Delta\Phi_{\gamma\gamma}$ -distribution of the spin-2 triplet case is similar to the singlet case with the coupling parameters $f_1 = 2, f_2 = f_3 = 1, f_{i \neq 1,2,3} = 0$ (see fig. 5.22).

Due to the the dependence on the formfactor and coupling parameters, this distribution is not sufficient to distinguish between a Higgs and a spin-2 resonance definitely, but together with other distributions, it can provide useful information about a potential spin-2 resonance and its parameters.

$\Delta\Phi_{jj}$

$\Delta\Phi_{jj}$ is the azimuthal angle difference of the two jets in the laboratory frame. Note that this distribution corresponds to another one: $\Delta\Phi_{12} = \Phi_1 - \Phi_2$, where

$\Phi_{1,2}$ are the azimuthal angles in the Breit frames, which are defined in appendix D. Indeed, the VBFNLO results show that these two distributions are exactly the same. This observation agrees with an accordant statement in Ref. [27].

Fig. 5.23 contains the $\Delta\Phi_{jj}$ distribution of the Higgs, fig. 5.24 depicts the spin-2 singlet case without formfactor and for fig. 5.25, a formfactor is applied. All three figures include two different sets of cuts: inclusive and inclusive + vbf cuts.

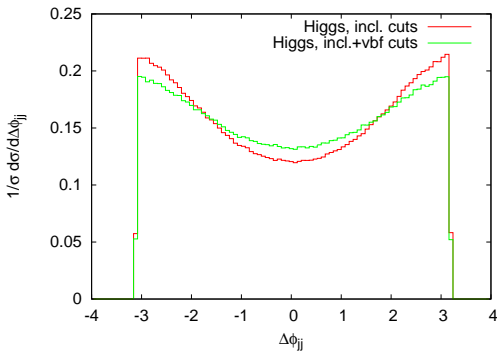


Figure 5.23: $\Delta\Phi_{jj}$, Higgs

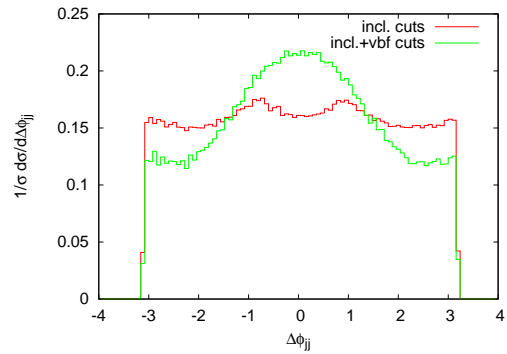


Figure 5.24: $\Delta\Phi_{jj}$, spin-2 singlet, without formfactor

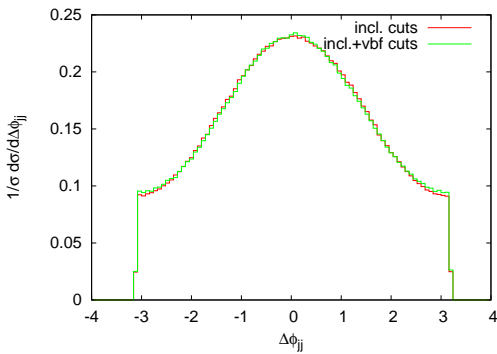


Figure 5.25: $\Delta\Phi_{jj}$, spin-2 singlet, with formfactor

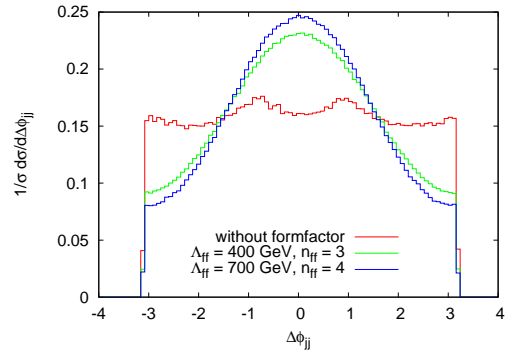


Figure 5.26: $\Delta\Phi_{jj}$, spin-2 singlet, inclusive cuts, different formfactor settings

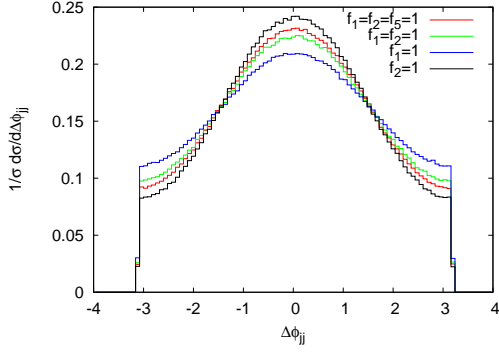


Figure 5.27: $\Delta\Phi_{jj}$, spin-2 singlet, with formfactor, inclusive cuts, different coupling parameters

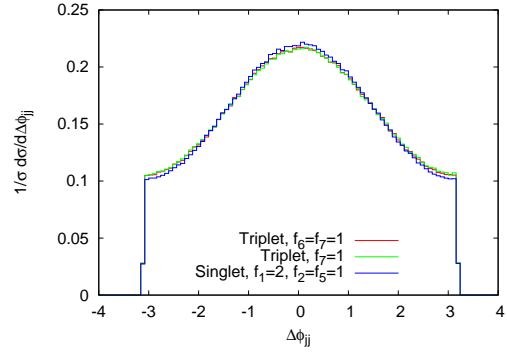


Figure 5.28: $\Delta\Phi_{jj}$, spin-2 singlet and triplet, with formfactor, inclusive cuts

The spin-2 case with a formfactor clearly differs from the Higgs case. Although the $\Delta\Phi_{jj}$ distribution depends slightly on the parameters of the formfactor, which is illustrated by fig. 5.26, and on the coupling parameters, which is depicted in fig. 5.27, the characteristic shape of this distribution is nearly independent from both of these parameters.

Therefore, the $\Delta\Phi_{jj}$ distribution provides a nice tool to distinguish between a Higgs and a spin-2 resonance.

Without a formfactor, the result is less evident. Especially for the use of inclusive cuts only, the distribution looks different than for other spin-2 settings (red line of fig. 5.24 and 5.26), as it is affected by the same kinematic effects which were discussed for the η_{jets} and p_T distributions.

cos Θ (Spin-2 (or Higgs) rest frame)

Another interesting distribution is $\cos \Theta$, with Θ being the angle between the momentum of the initial electroweak boson (q_1) and the outgoing photon (q'_1) in the rest frame of the intermediate particle (Higgs or spin-2) (see appendix D). As detailed calculations of Ref. [27] show, the dependence of the matrix element on Θ is contained in a dependence on the Wigner d-functions $d_{m,m'}^j(\Theta)$ (see appendix E). Therefore, the $\cos \Theta$ distribution should be an indicator of the spin of the resonance. Of course, one could also take the corresponding rapidity $\eta = -\ln \tan \frac{\Theta}{2}$, but the analysis reveals that the features of this distribution are less explicit than those of the $\cos \Theta$ distribution.

Fig. 5.29 and 5.30 compare the $\cos \Theta$ distribution of a spin-2 resonance to the one of a Higgs resonance for inclusive cuts (left hand side) and inclusive + vbf cuts (right hand side). One can see that applying additional vbf cuts hardly influences these distributions. In fig. 5.30, the spin-2 case includes the formfactor, in fig. 5.29, it does not.

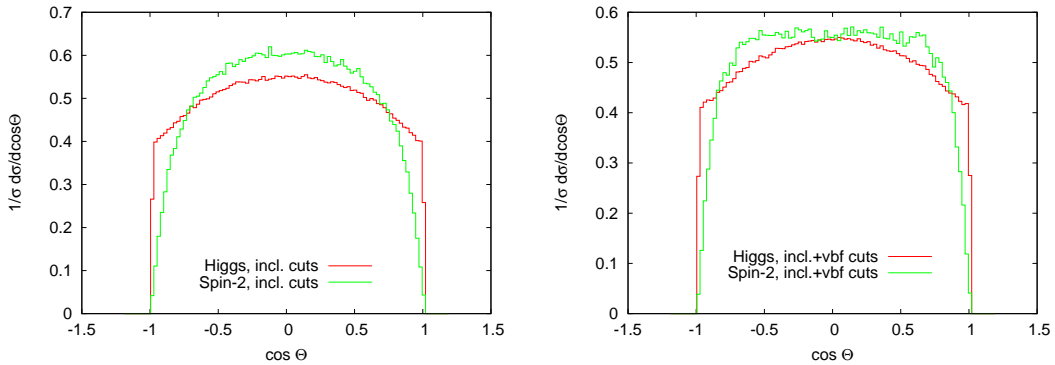


Figure 5.29: $\cos \Theta$, spin-2 singlet without formfactor versus Higgs. Left hand side: inclusive cuts, right hand side: inclusive + vbf cuts

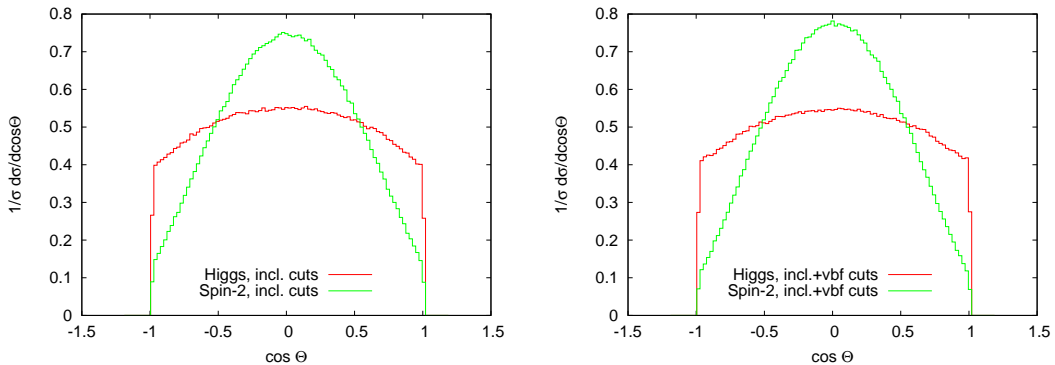


Figure 5.30: $\cos \Theta$, spin-2 singlet with formfactor versus Higgs. Left hand side: inclusive cuts, right hand side: inclusive + vbf cuts

Both of these figures reveal a difference between a Higgs and a spin-2 resonance, but without the formfactor, it is less evident.

However, the Higgs distribution is affected by the cuts: As shown in fig. 5.31, it is flat if the cuts are removed. For the spin-2 case, the cuts cannot be just removed without running into singularities caused by initial state photons. These singularities were evaded by excluding the Feynman diagrams with t-channel photons for the spin-2 case without cuts for a comparison of the spin-2 and the Higgs case in fig. 5.31.

Analogous to other distributions ($p_T, \eta_{jets}, \Delta\Phi_{jj}$), the $\cos \Theta$ distribution depends slightly on the coupling parameters. However, the general shape is the same. This dependence is illustrated by fig. 5.32 for the spin-2 singlet case with formfactor and inclusive cuts.

Again, the distribution of the spin-2 triplet case is similar to the singlet case with the coupling parameters $f_1 = 2, f_2 = f_3 = 1, f_{i \neq 1,2,5} = 0$ (see fig. 5.33).

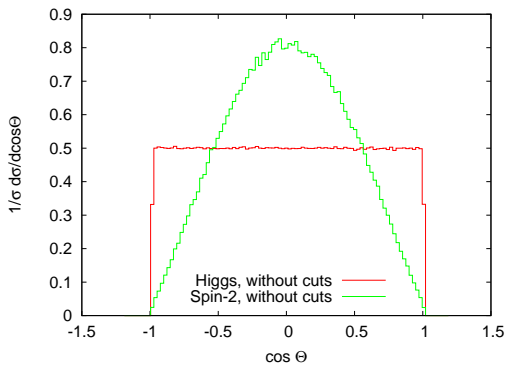


Figure 5.31: $\cos \Theta$, spin-2 singlet without formfactor versus Higgs, without cuts

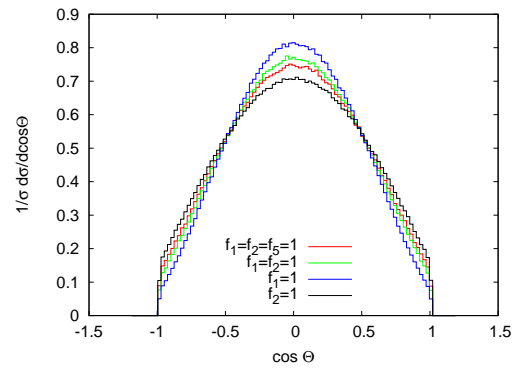


Figure 5.32: $\cos \Theta$, spin-2 singlet, with formfactor, inclusive cuts, different coupling parameters

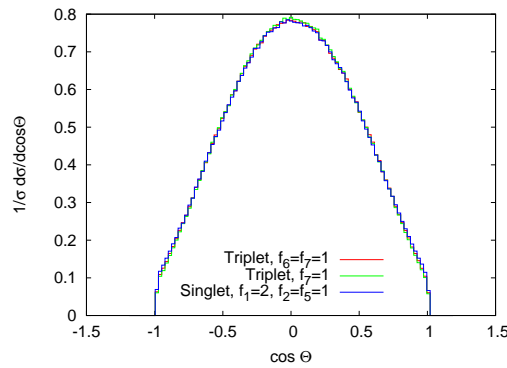


Figure 5.33: $\cos \Theta$, spin-2 singlet and triplet, with formfactor, inclusive cuts

All in all, the $\cos \Theta$ distribution shows a fundamental difference between a spin-2 and a Higgs resonance. Therefore, it is an appropriate distribution for a distinction between the two cases.

θ_1, θ_2 (Breit frame)

θ_1 and θ_2 are the polar angles in the Breit frames of the two initial vector bosons (see appendix D).

Fig. 5.34 shows the θ_1 distribution for inclusive cuts for the three cases Higgs, spin-2 without formfactor and spin-2 with formfactor. The same cases are depicted in fig. 5.35 for inclusive + vbf cuts.

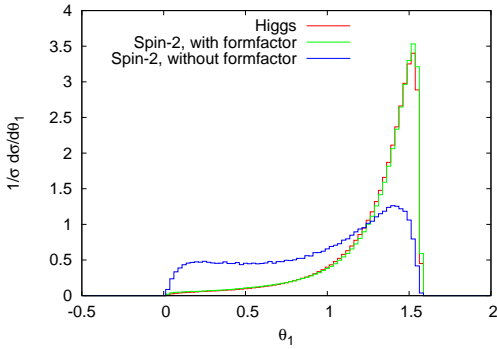


Figure 5.34: θ_1 , inclusive cuts

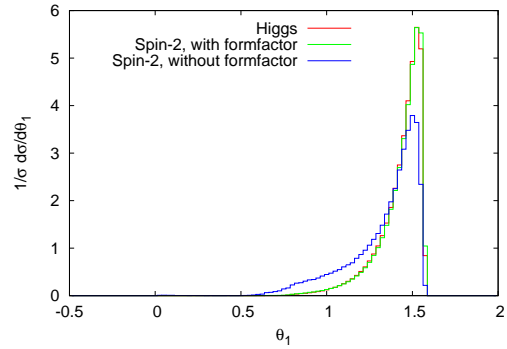


Figure 5.35: θ_1 , inclusive + vbf cuts

Obviously, these distributions do not depend on the spin, but on the formfactor. This is because the θ_1 distribution corresponds to the p_T distribution of the jet, and as the p_T distributions of the spin-2 resonance can be adjusted to the Higgs case by the formfactor (fig. 5.9), the formfactor influences the θ_1 distribution in the same way.

Furthermore, this distribution depends on the cuts, since the vbf cuts set constraints on the rapidity of the jets, which also influences the θ_1 distribution.

The features of the θ_2 distribution are exactly the same as those of the θ_1 distribution, as the θ_2 distribution is similar to the θ_1 distribution mirrored at $\theta_1 = \pi/2$.

In order to analyze possible correlations between θ_1 and θ_2 , the double-differential distribution $d^2\sigma/(d\theta_1 d\theta_2)$ has also been checked, but it did not reveal any additional effects.

Thus, as the θ_1 and θ_2 distributions only depend on kinematic effects, but not on the spin of the resonance, they are not suitable to distinguish between a Higgs and a spin-2 resonance.

$$\underline{d^2\sigma/d\Delta\Phi_{12} d\cos\Theta}$$

Fig. 5.36 - 5.39 depict the double differential distribution $d^2\sigma/d\Delta\Phi_{12} d\cos\Theta$. Fig. 5.36 contains the Higgs case, the other figures show the spin-2 singlet case with standard formfactor for different parameter settings. As illustrated by fig. 5.36 and 5.37, vbf cuts hardly influence this distribution.

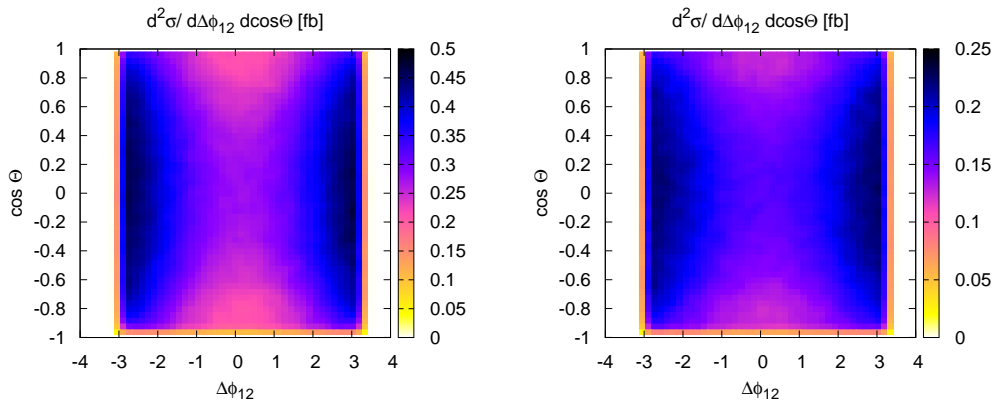


Figure 5.36: Higgs, left hand side: inclusive cuts, right hand side: inclusive + vbf cuts

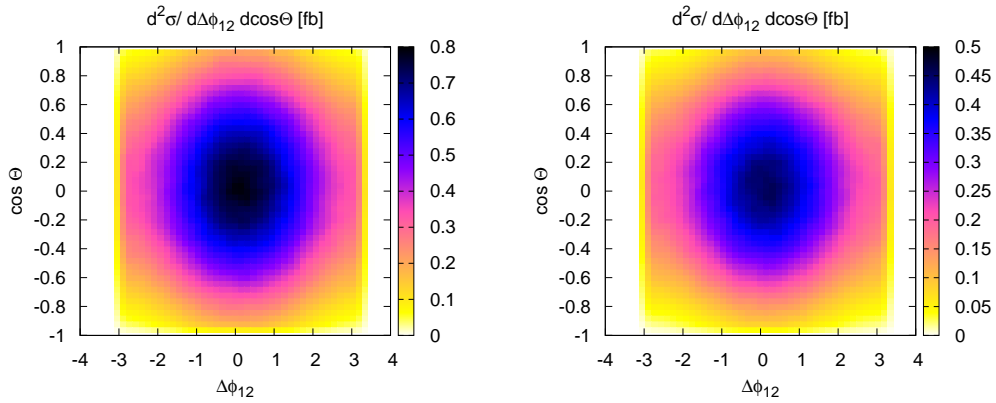


Figure 5.37: Spin-2 singlet, with formfactor, left hand side: inclusive cuts, right hand side: inclusive + vbf cuts

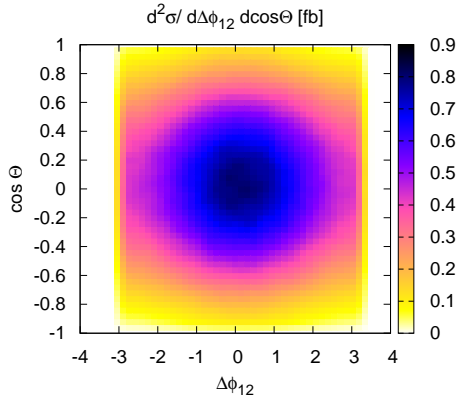


Figure 5.38: Spin-2 singlet, $f_1 = 1$,
 $f_{i \neq 1} = 0$, $\Lambda = 10$ TeV,
with formfactor, inclusive cuts

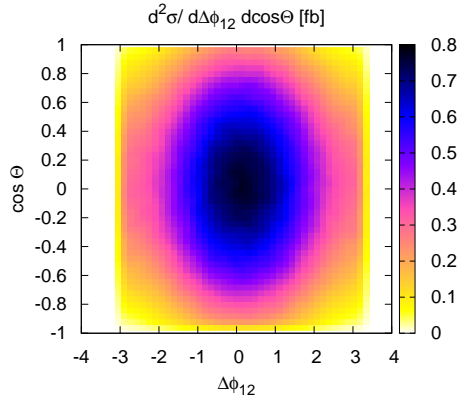


Figure 5.39: Spin-2 singlet, $f_2 = 1$,
 $f_{i \neq 2} = 0$, $\Lambda = 10$ TeV, with
formfactor, inclusive cuts

These plots nicely combine the features of the $\cos \Theta$ and the $\Delta \Phi_{12}$ distributions which were presented previously. They also show that there is no correlation between these two distributions. As mentioned before, the $\Delta \Phi_{12}$ distribution is similar to the $\Delta \Phi_{jj}$ distribution.

Since there is a huge difference between the double differential plots of the Higgs and the spin-2 resonance as well as a significant difference between different spin-2 couplings, this distribution provides a great tool for a distinction between a Higgs and a spin-2 resonance and possibly between different spin-2 parameters.

Other angular distributions

Analogous to the $\cos \Theta$ distribution, $\cos \Theta_{j1,2}$ distributions were analyzed, where $\Theta_{j1,2}$ is the angle between q'_1 and the first or second jet in the rest frame of the intermediate particle (Higgs or spin-2) (see appendix D). They have characteristics similar to the $\cos \Theta$ distribution: The distributions of a spin-2 resonance are always steeper than the ones of the Higgs (which are flat if the cuts are removed) and depend slightly on the formfactor and the coupling parameters.

Furthermore, the distributions corresponding to the various terms of azimuthal angle dependences, which were calculated analytically in eq. 5.5 of Ref. [27], were investigated. Except for the $\Delta \Phi_{12}$ distribution (which is exactly the same as the $\Delta \Phi_{jj}$ distribution presented above) and the $2(\Phi_1 - \Phi_2)$ distribution, all the other distributions are flat both for a Higgs and a spin-2 resonance.

Double differential distributions combining these azimuthal angle terms with Θ or the Breit frame angle θ_1 or Θ with θ_1 did not reveal any additional effects, they only reflect the characteristics of the two single distributions they consist of.

5.2.5 Summary of photon pair-production in VBF via Higgs and Spin-2 resonances

The results presented in this section indicate that it is possible to distinguish between a Higgs and a spin-2 resonance in the vector boson fusion process $VV \rightarrow \gamma\gamma$, while the detailed features of a spin-2 resonance depend on their parameters.

The spin-2 coupling parameters can be tuned such that the cross section is similar to the Higgs case.

The width of a spin-2 resonance differs from the width of a Higgs resonance unless the branching ratio is adjusted. However, this is not observable in CMS and ATLAS.

The p_T distributions are different unless a formfactor with adjusted parameters is applied.

Angular distributions play the most important role. Especially the $\Delta\Phi_{jj}$ and the $\cos\Theta$ distribution are clearly different for a Higgs resonance and spin-2 resonance with a formfactor.

Without the formfactor, these differences are less evident, but in this case, the difference in the p_T distributions can be used as an additional tool to distinguish between a Higgs and a spin-2 resonance.

For all the considered distributions, the spin-2 triplet case resembles the singlet case with adequate coupling parameters.

This can be understood by looking at the Feynman diagrams of this process (section 4.4.6): Apart from two additional non-resonant charged triplet diagrams which hardly contribute, the diagrams are the same for the singlet and the triplet case.

Therefore, this process is not useful for a distinction between a spin-2 singlet and a spin-2 triplet resonance.

5.3 Heavy Spin-2 resonances in four-charged-lepton production via the VBF process $pp \rightarrow VV jj \rightarrow e^+ e^- \mu^+ \mu^- jj$

In the following subsections, heavy spin-2 resonances in VBF processes with four leptons in the final state are investigated. This section deals with process 210, which contains four charged leptons and no neutrinos in the final state. Therefore, a resonance in the invariant mass spectrum of the leptons can be reconstructed exactly, whereas for the other processes, where the four final state leptons also contain neutrinos, this is more difficult. This is why process 210 is analyzed in most detail.

This section contains a list of cross sections for different scenarios and masses of the spin-2 resonance and an analysis both of invariant mass distributions of the four final state leptons and of transverse momentum and angular distributions, which shall reveal the features of heavy spin-2 resonances.

If not indicated otherwise, the analysis is performed with the following settings (see Appendix C.1, C.3):

- The VBFNLO calculation is done with 4 iterations and 2^{24} points.
- The masses of the spin-2 particles are chosen as 1 TeV.
- All the spin-2 branching ratio parameters are set to 1.
- The usual spin-2 parameter settings are:
Spin-2 singlet: $f_1 = f_2 = f_5 = 1, f_{i \neq 1,2,5} = 0, \Lambda = 1500 \text{ GeV}$
Spin-2 triplet: $f_6 = f_7 = 1, f_{i \neq 6,7} = 0, \Lambda = 1500 \text{ GeV}$
If a formfactor is used, its parameters are: $\Lambda_{ff} = 3 \text{ TeV}, n_{ff} = 4$
- The complete Standard Model background as well as all the spin-2 diagrams shown in chapter 4.4.2 are included.
- Inclusive + vbf cuts are applied.
- Effects of the detector resolution are discarded (see section 5.2).

Note that the cross sections given in table 5.2 (and also all the distributions presented in this section) correspond to the leptonic final state $e^+ e^- e^+ e^-$. For $\mu^+ \mu^- \mu^+ \mu^-$, they are the same, as lepton masses are neglected in VBFNLO. For $e^+ e^- \mu^+ \mu^-$, however, they are twice as high, since for the final states $e^+ e^- e^+ e^-$ and $\mu^+ \mu^- \mu^+ \mu^-$, there is a symmetry factor 0.5 due to the

identical leptons. The cross section for all the possible combinations of final state leptons together can be obtained by multiplying the given cross sections with an appropriate multiplicity factor. This is the case for all the considered processes with four leptons in the final state (210, 211, 200, 220 and 230, see also chapter 5.4). For some of the final states, there is some interference between different processes, but this interference is insignificant. One such example is $e^+ e^- \nu_e \bar{\nu}_e$, which can be generated both as $(e^+ e^-) (\nu_e \bar{\nu}_e)$ (process 211) and as $(e^+ \nu_e) (e^- \bar{\nu}_e)$ (process 200), where the brackets group the fermions into pairs connected by a continuous fermion line. The first case gives rise to events with $m_{e^+e^-} \approx m_Z \approx m_{\nu_e \bar{\nu}_e}$ while the second case has $m_{e^+ \nu_e} \approx m_W \approx m_{e^- \bar{\nu}_e}$.

5.3.1 Cross sections

Table 5.2 gives an overview of the cross sections and the corresponding errors due to Monte Carlo integration computed by VBFNLO for different scenarios and different masses of the spin-2 resonance for the leptonic final state $e^+ e^- e^+ e^-$. To obtain the total cross sections of the final states $e^+ e^- \mu^+ \mu^-$, $e^+ e^- e^+ e^-$ and $\mu^+ \mu^- \mu^+ \mu^-$ together, the given cross sections have to be multiplied by 4.

Process and parameters	Cross section [fb]	Error [fb]
SM, without spin-2	$2.2715 \cdot 10^{-2}$	$4.4636 \cdot 10^{-5}$
Spin-2 singlet, without formfactor, $m = 1000$ GeV, $f_1 = f_2 = f_3 = 1$	$8.8837 \cdot 10^{-2}$	$1.8511 \cdot 10^{-4}$
Spin-2 singlet, without formfactor, $m = 1000$ GeV, $f_1 = f_2 = f_3 = f_4 = f_5 = 1$	0.2427	$4.1469 \cdot 10^{-4}$
Spin-2 singlet, with formfactor, $m = 500$ GeV	$3.7217 \cdot 10^{-2}$	$1.6235 \cdot 10^{-4}$
Spin-2 singlet, with formfactor, $m = 750$ GeV	$2.5296 \cdot 10^{-2}$	$2.1982 \cdot 10^{-4}$
Spin-2 singlet, with formfactor, $m = 1000$ GeV	$2.3905 \cdot 10^{-2}$	$1.0464 \cdot 10^{-4}$
Spin-2 singlet, with formfactor, $m = 1250$ GeV	$2.2735 \cdot 10^{-2}$	$1.8740 \cdot 10^{-4}$
Spin-2 singlet, with formfactor, $m = 1500$ GeV	$2.2893 \cdot 10^{-2}$	$1.2104 \cdot 10^{-4}$
Spin-2 triplet, with formfactor, $m = 1000$ GeV	$2.2949 \cdot 10^{-2}$	$1.3888 \cdot 10^{-4}$

Table 5.2: Total cross sections and errors for process 210

5.3.2 Invariant mass distribution of the four final state leptons

Fig. 5.40 depicts the invariant mass distribution of the four final state leptons from 0 to 11 TeV. For the Standard Model diagrams only (red line), a Higgs resonance at 120 GeV (which is not visible in this large mass range, but later in fig. 5.42 and 5.43) is followed by a continuous distribution which vanishes for high energies. For the spin-2 singlet case without a formfactor (green line), a spin-2 resonance at 1 TeV is visible. However, there are significant high-energy contributions resulting from unitarity violation (see chapter 5.1), which only decrease and vanish for very high energies due to the suppression by the PDFs. In order to get rid of these unphysical high-energy contributions, the formfactor (eq. 5.4) is used. For $\Lambda_{ff} = 3$ TeV and $n_{ff} = 4$, these contributions are suppressed efficiently (blue line).

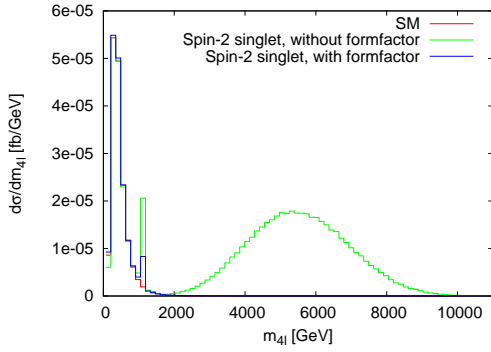


Figure 5.40: Invariant mass of the four final state leptons, with and without formfactor

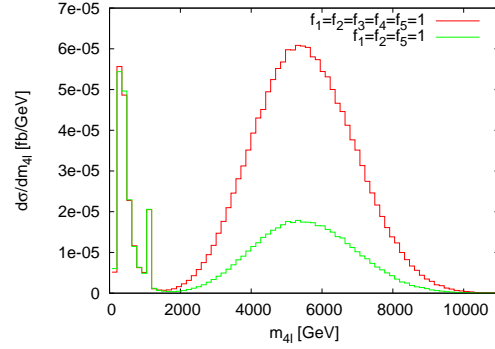


Figure 5.41: Invariant mass of the four final state leptons, influence of f_3 and f_4

In this process, the effects of the couplings f_3 and f_4 are clearly visible (fig. 5.41). Although these couplings do not lead to a resonance, they increase the high-energy contributions significantly. This also leads to a large modification of the total cross section (see table 5.2).

For different masses of the spin-2 singlet particle, the invariant mass distribution is shown in fig. 5.42 and 5.43. There, the spin-2 resonance peak is visible even for a mass of 1.5 TeV. The spin-2 triplet case is analogous, except for the height and width of the resonance, which is shown exemplarily for a mass of 1 TeV in fig. 5.43. The triplet resonance is generated by the neutral spin-2 triplet particle, since for the charged particle, there are only non-resonant Feynman diagrams for this process (see section 4.4.2). Due to the use of the formfactor, there are no contributions outside the depicted mass range, except

for a mass of 500 GeV, where a smaller value of Λ_{ff} has to be used to suppress these contributions completely.

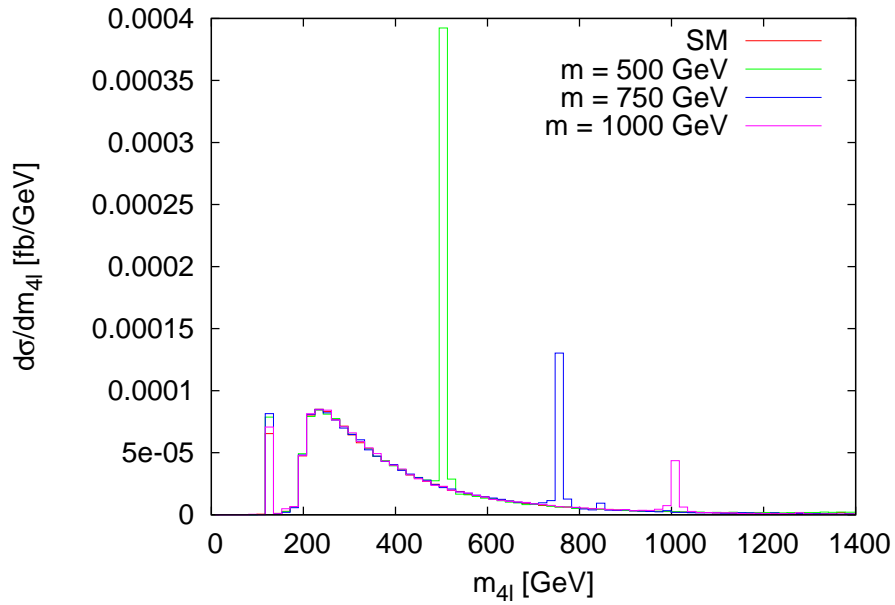


Figure 5.42: Spin-2 singlet resonance for different masses

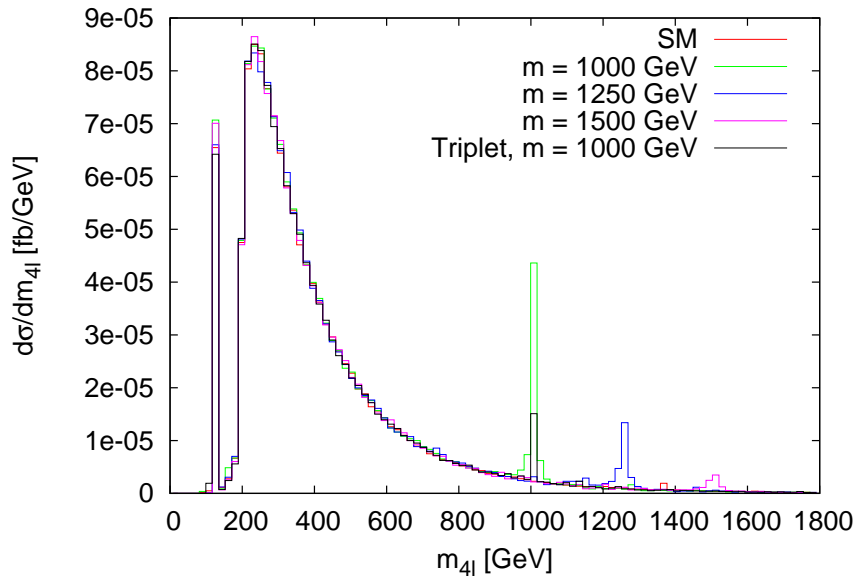


Figure 5.43: Spin-2 resonance for different masses, singlet and triplet

Table 5.3 gives an overview of the total widths of the resonances shown in fig. 5.42 and 5.43. For the triplet resonance, this is the width of the neutral particle. These widths correspond to branching ratio parameters = 1. They are relatively small, so the choice of larger couplings f_i or a smaller value of Λ would also be sensible. This choice would increase the widths and the observed rates proportional to $\left(\frac{f_i}{\Lambda}\right)^2$.

Resonance	Width [GeV]
Singlet, 500 GeV	0.982
Singlet, 750 GeV	3.238
Singlet, 1000 GeV	7.607
Singlet, 1250 GeV	14.795
Singlet, 1500 GeV	25.505
Triplet, 1000 GeV	1.004

Table 5.3: Total widths of the resonances shown in fig. 5.42 and 5.43

5.3.3 Transverse momentum and angular distributions

In this section, the characteristics of the transverse momentum and angular distributions of a spin-2 resonance are analyzed for singlet and triplet resonances at 1 TeV. Thereby, the formfactor with the parameters $\Lambda_{ff} = 3$ TeV and $n_{ff} = 4$ is always applied. If not indicated otherwise, the singlet case with the usual parameter settings is studied.

Since the spin-2 resonance contributes little to the total cross section, which can be seen in table 5.2, these distributions would be dominated by the SM background. In order to reveal the features of the spin-2 resonance, additional cuts on the invariant lepton mass are applied (see section 4.5.2) to restrict it to the region of the spin-2 resonance peak. The values of MLEP_MIN and MLEP_MAX are adjusted to the width of the resonance.

For the parameter settings $f_1 = f_2 = f_5 = 1$, $f_{i \neq 1,2,5} = 0$ and $f_1 = f_2 = 1$, $f_{i \neq 1,2} = 0$, they are chosen as MLEP_MIN = 950 GeV and MLEP_MAX = 1050 GeV. For the triplet case, MLEP_MIN = 990 GeV and MLEP_MAX = 1010 GeV are used and for $f_5 = 1$, $f_{i \neq 5} = 0$, the chosen values are MLEP_MIN = 995 GeV and MLEP_MAX = 1005 GeV. The latter cases are only presented for illustration, since the experimental resolution is worse.

However, for larger couplings f_i or a smaller value of Λ , smaller values of MLEP_MIN and larger values of MLEP_MAX could be used.

In order to compare the features of the spin-2 resonance to those of the SM background, the same cuts on the invariant lepton mass are applied to the SM background. For the SM distributions shown in this section, MLEP_MIN = 950 GeV and MLEP_MAX = 1050 GeV are used. For MLEP_MIN = 990 GeV and MLEP_MAX = 1010 GeV and MLEP_MIN = 995 GeV and MLEP_MAX = 1005 GeV, there is hardly any modification of all the SM distributions.

Note that all the figures which are presented in this section include a normalization factor $1/\sigma$.

p_T of the jet with the largest transverse momentum

Fig. 5.44, 5.45 and 5.46 depict the p_T distribution of the jet with the largest transverse momentum. The distributions of the spin-2 resonance are hardly affected by the SM background, which is exemplified by the blue line of fig. 5.44, except for the parameter setting $f_5 = 1, f_{i \neq 5} = 0$, where the resonance is very small and narrow. Therefore, fig. 5.46 shows the distribution both with and without the SM background. This is also the case for the other p_T and angular distributions of this section.

From fig. 5.44 and 5.45, one can see that this distribution is rather similar with and without a spin-2 resonance for most of the parameter settings. The SM distribution just peaks at slightly higher values of p_T . However, for $f_5 = 1, f_{i \neq 5} = 0$, the distribution changes significantly (fig. 5.46).

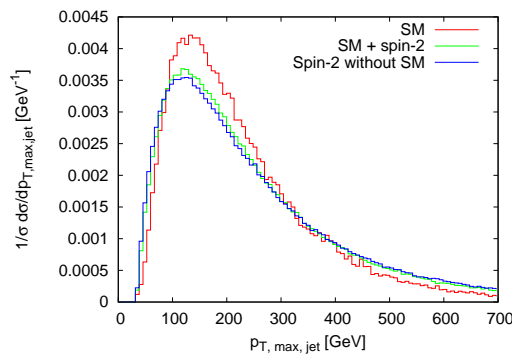


Figure 5.44: $p_{T,max,jet}$, spin-2 singlet resonance ($f_1 = f_2 = f_5 = 1, f_{i \neq 1,2,5} = 0$)

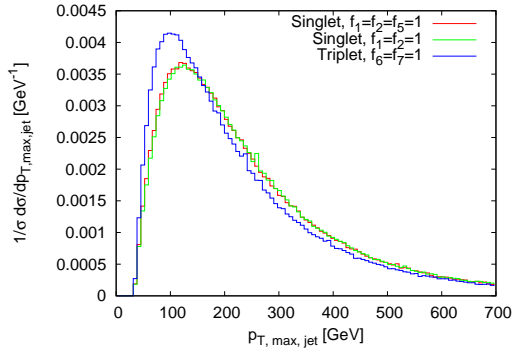


Figure 5.45: $p_{T,max,jet}$,
different parameter settings

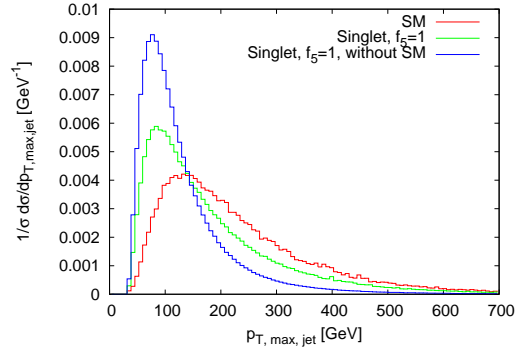


Figure 5.46: $p_{T,max,jet}$ for $f_5 = 1$,
 $f_{i \neq 5} = 0$

p_T of the final state lepton with the largest transverse momentum

In contrast to the $p_{T,max,jet}$ distribution, the p_T distribution of the final state lepton with the largest transverse momentum (denoted as $p_{T,max,l}$) is affected significantly by the spin-2 resonance, which can be seen in fig. 5.47. Whereas the singlet and triplet case look almost the same for the parameter settings considered in fig. 5.48, the coupling f_5 alone leads to a different, characteristic distribution (fig. 5.49).

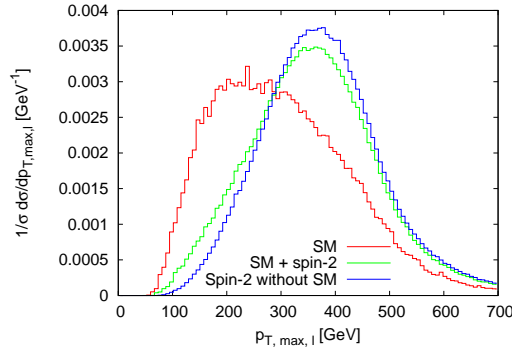


Figure 5.47: $p_{T,max,l}$, spin-2 singlet resonance ($f_1 = f_2 = f_5 = 1$, $f_{i \neq 1,2,5} = 0$)

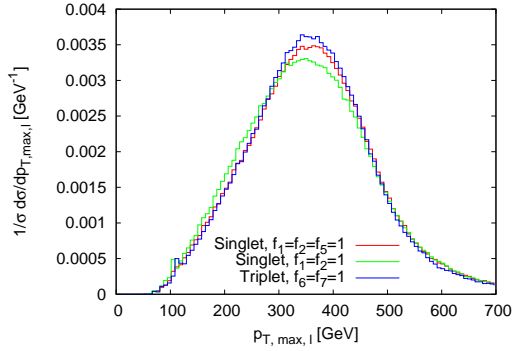


Figure 5.48: $p_{T,max,l}$,
different parameter settings

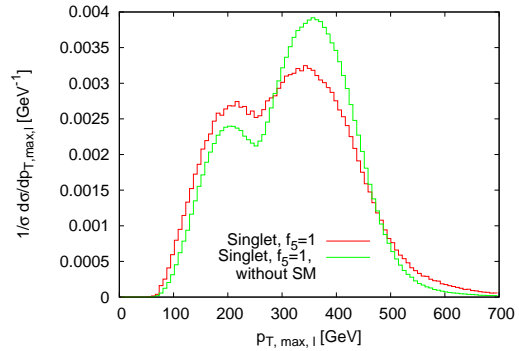


Figure 5.49: $p_{T,max,l}$ for $f_5 = 1$, $f_{i \neq 5} = 0$

cos Θ (Spin-2 rest frame)

As in chapter 5.2.4, the $\cos \Theta$ distribution is investigated for this process as well. Θ is the angle between the momenta of an incoming and an outgoing electroweak boson (q_1 and q'_1) in frame (III) of appendix D, which is the rest frame of the spin-2 particle in case of a spin-2 resonance. For the processes with four leptons in the final state, q'_1 is the sum of the two momenta of the respective final state leptons.

There is a clear difference between the $\cos \Theta$ distribution of the spin-2 resonance and the SM background, which is illustrated by fig. 5.50.

The distributions of the singlet and the triplet resonance are almost identical (see fig. 5.52).

In contrast to the p_T distributions, the $\cos \Theta$ distribution is affected by the absence of the coupling f_5 (green line of fig. 5.52). This is not an effect of a larger contribution of the SM background, but a feature of the spin-2 couplings, which is proven by the black line of fig. 5.52.

The coupling f_5 alone again leads to a different, characteristic distribution (fig. 5.53).

Fig. 5.51 depicts the $\cos \Theta$ distribution of the Higgs resonance for $m_H = 120$ GeV. For this purpose, MLEP_MAX is set to 150 GeV. This distribution can be compared to the right hand sides of fig. 5.29 and 5.30 (red line), which show the $\cos \Theta$ distribution of the Higgs resonance in the photon pair-production process 240. Despite the different final state and the absence of any SM background in process 240, the characteristic shape of this distribution is the same.

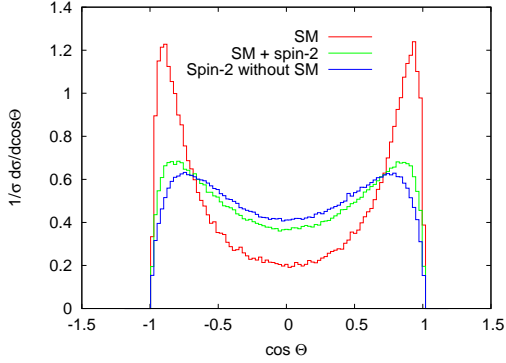


Figure 5.50: $\cos \Theta$, spin-2 singlet resonance

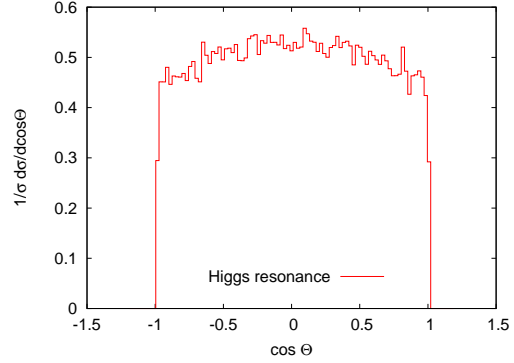


Figure 5.51: $\cos \Theta$, Higgs resonance

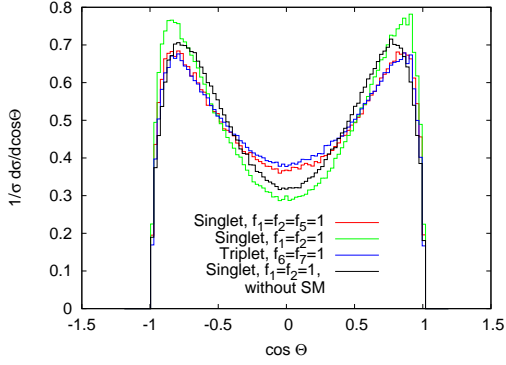


Figure 5.52: $\cos \Theta$, different parameter settings

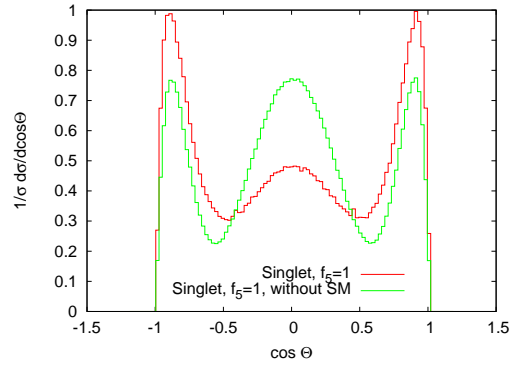


Figure 5.53: $\cos \Theta$ for $f_5 = 1, f_{i \neq 5} = 0$

$\Delta\Phi_{jj}$

The azimuthal angle difference of the two jets in the laboratory frame, $\Delta\Phi_{jj}$, is shown in fig 5.54, 5.55 and 5.56. As already mentioned in chapter 5.2.4, this distribution corresponds to the $\Delta\Phi_{12} = \Phi_1 - \Phi_2$ distribution, where $\Phi_{1,2}$ are the azimuthal angles in the Breit frames, which are defined in appendix D.

The characteristics of $\Delta\Phi_{jj}$ are different for a spin-2 resonance and the SM background (fig. 5.54). Whereas for the SM case, the jets are mostly back-to-back, the spin-2 resonance leads to a rather flat $\Delta\Phi_{jj}$ distribution, where values around zero are slightly preferred.

This distribution is hardly affected by a change of the spin-2 couplings (fig. 5.55), although the characteristic shape is obscured by the SM background in the case $f_5 = 1, f_{i \neq 5} = 0$ (fig. 5.56).

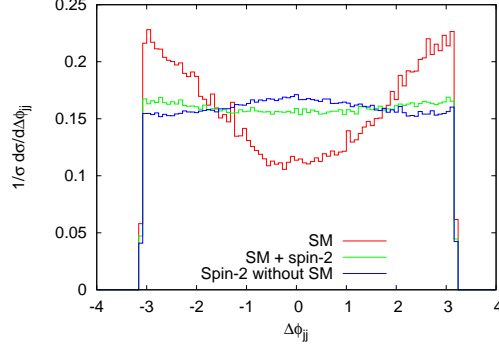


Figure 5.54: $\Delta\Phi_{jj}$, spin-2 singlet resonance ($f_1 = f_2 = f_5 = 1$, $f_{i \neq 1,2,5} = 0$)

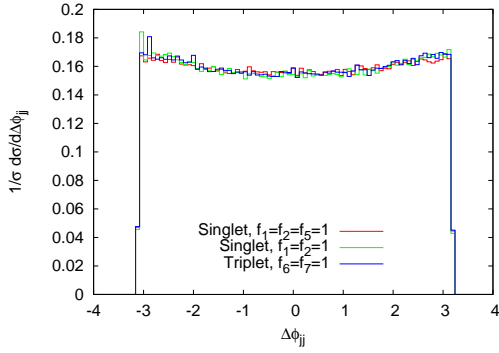


Figure 5.55: $\Delta\Phi_{jj}$, different parameter settings

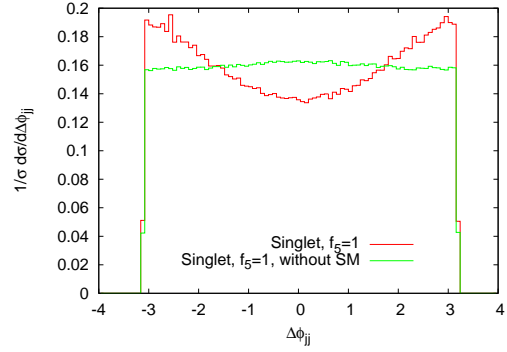


Figure 5.56: $\Delta\Phi_{jj}$ for $f_5 = 1$, $f_{i \neq 5} = 0$

Angular distributions of the final state leptons

The following figures present some angular distributions between two of the final state leptons which do not emerge from the same vector boson. There are four different possible combinations of such leptons. For the distributions presented here, the two positively charged leptons are chosen. The distributions of the other combinations of leptons look similar.

$\Delta\eta_l$

Fig. 5.57, 5.58 and 5.59 depict the rapidity difference of the two leptons, denoted as $\Delta\eta_l$. There is a clear difference between the distribution of the spin-2 resonance and the one of the SM, which can be seen in fig. 5.57. The spin-2 resonance leads to smaller values of $\Delta\eta_l$.

Whereas the singlet case with $f_1 = f_2 = f_5 = 1$, $f_{i \neq 1,2,5} = 0$ looks nearly the same as the triplet case with $f_6 = f_7 = 1$, $f_{i \neq 6,7} = 0$, the absence of f_5 in the singlet case causes a small modification of $\Delta\eta_l$ (fig. 5.58). Again, the coupling f_5 alone leads to a different, characteristic distribution (see fig. 5.59).

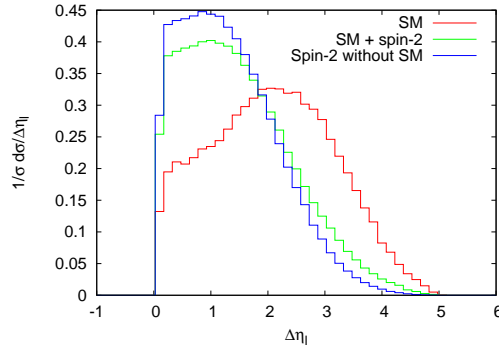


Figure 5.57: $\Delta\eta_l$, spin-2 singlet resonance ($f_1 = f_2 = f_5 = 1$, $f_{i \neq 1,2,5} = 0$)

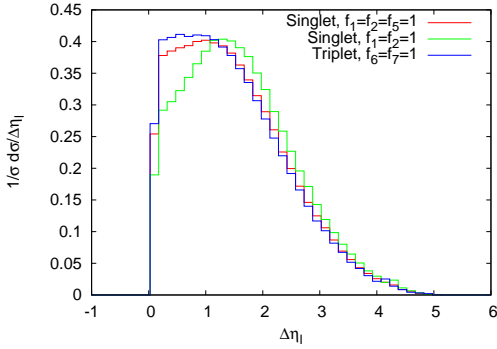


Figure 5.58: $\Delta\eta_l$, different parameter settings

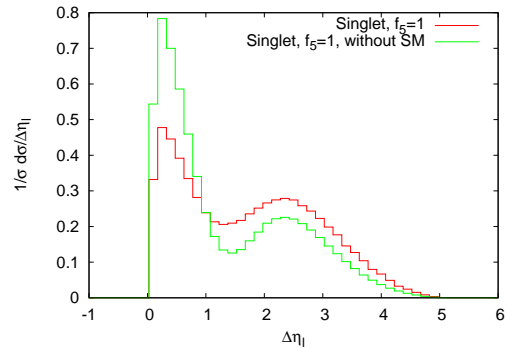


Figure 5.59: $\Delta\eta_l$ for $f_5 = 1$, $f_{i \neq 5} = 0$

$\Delta\Phi_l$

The differences between the SM and the spin-2 resonance are less distinct in the azimuthal angle difference of the two leptons ($\Delta\Phi_l$). In both cases, the leptons are mainly back-to-back due to the large considered invariant mass of the four-lepton system (see fig. 5.60). As illustrated by fig. 5.61, the different parameter settings can hardly be distinguished, except for $f_5 = 1$, $f_{i \neq 5} = 0$, which leads to a $\Delta\Phi_l$ distribution where the leptons are even more back-to-back (see fig. 5.62).

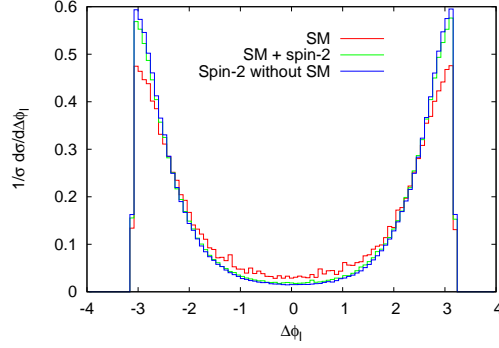


Figure 5.60: $\Delta\Phi_l$, spin-2 singlet resonance ($f_1 = f_2 = f_5 = 1$, $f_{i \neq 1,2,5} = 0$)

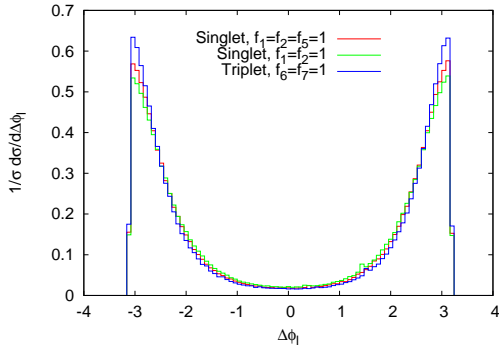


Figure 5.61: $\Delta\Phi_l$, different parameter settings

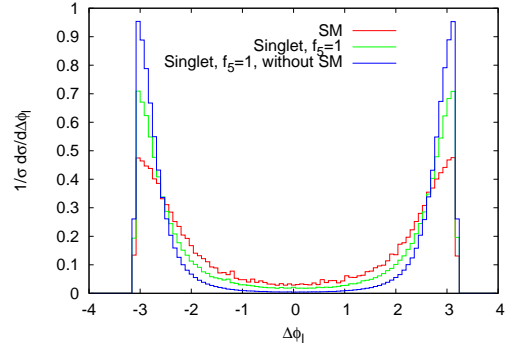


Figure 5.62: $\Delta\Phi_l$ for $f_5 = 1$, $f_{i \neq 5} = 0$

ΔR_l

Fig. 5.63, 5.64 and 5.65 depict the R-separation ΔR_l of the two leptons. Since ΔR_l is defined as $\Delta R_l = \sqrt{\Delta\eta_l^2 + \Delta\Phi_l^2}$, this distribution combines the features of the $\Delta\eta_l$ and the $\Delta\Phi_l$ distribution.

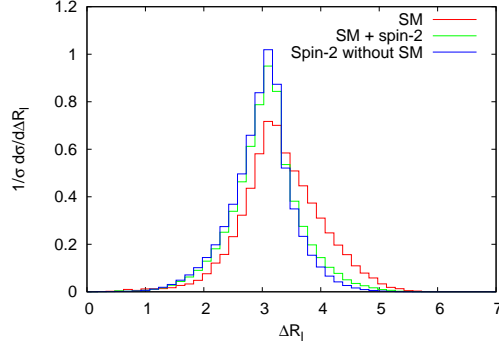


Figure 5.63: ΔR_l , spin-2 singlet resonance ($f_1 = f_2 = f_5 = 1$, $f_{i \neq 1,2,5} = 0$)

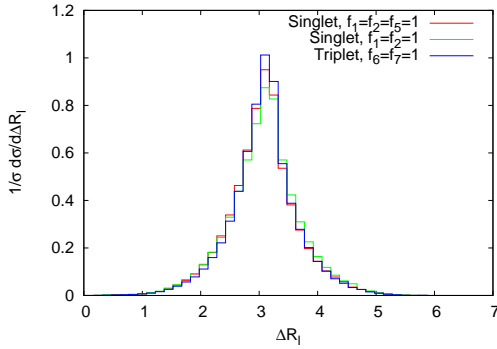


Figure 5.64: ΔR_l , different parameter settings

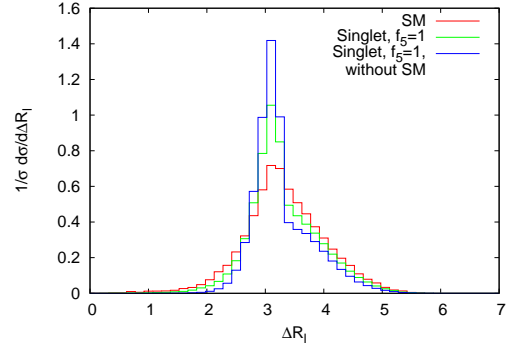


Figure 5.65: ΔR_l for $f_5 = 1$, $f_{i \neq 5} = 0$

Other angular distributions

Apart from the distributions presented above, various other angular distributions were investigated.

One of them is the rapidity of the two tagging jets. This distribution does not reveal any differences between the spin-2 resonance and the SM background, but shows the rapidity gap which is characteristic for vector boson fusion processes.

Analogous to the $\cos \Theta$ distribution, $\cos \Theta_{j1,2}$ distributions were studied, where $\Theta_{j1,2}$ is the angle between q'_1 and the first or second jet in the rest frame (III) of appendix D. They have characteristics similar to the $\cos \Theta$ distribution.

As in case of the photon pair-production process 240, θ_1 and θ_2 , which

are the polar angles in the Breit frames of the two initial electroweak bosons (see appendix D), were analyzed. Similar to that process, these distributions do not reveal any characteristic features of a spin-2 resonance.

Moreover, the distributions corresponding to the various terms of azimuthal angle dependences, which were calculated in Ref. [27], were studied. Except for the $\Delta\Phi_{12}$ distribution (which is exactly the same as the $\Delta\Phi_{jj}$ distribution presented above) and the $2(\Phi_1 - \Phi_2)$ distribution, all the other distributions are flat both for a spin-2 resonance and the SM background.

Double differential distributions which combine these azimuthal angle terms with the Breit frame angle θ_1 or Θ or θ_1 with Θ did not reveal any additional effects, they only reflect the features of the two single distributions they consist of.

5.4 Heavy Spin-2 resonances in other VBF processes with four leptons in the final state

The features of heavy spin-2 resonances in the other considered processes with four leptons in the final state, 211, 200, 220 and 230, are very similar to those of the process $pp \rightarrow VV jj \rightarrow e^+ e^- \mu^+ \mu^- jj$ (process 210), which was studied extensively in the previous section. Especially the characteristics of the transverse momentum and angular distributions are the same in most cases.

Therefore, this section focuses on the invariant mass distributions of the final state leptons, although it is more difficult to reconstruct resonances which emerge in the processes considered here, since all these processes contain one or two neutrinos in the final state.

Additionally, some total cross sections and the corresponding errors due to Monte Carlo integration computed by VBFNLO are given for all the processes.

5.4.1 Process 211: $pp \rightarrow VV jj \rightarrow e^+ e^- \nu_\mu \bar{\nu}_\mu jj$

This process is very similar to the process $pp \rightarrow VV jj \rightarrow e^+ e^- \mu^+ \mu^- jj$ (process 210), as it contains in principle the same Feynman diagrams, but a smaller number of them, since photons can only couple to charged leptons, but not to neutrinos.

All the settings for this process are the same as the standard settings for process 210 (see section 5.3).

Note that there is no use in investigating the angular distributions of the final state leptons which were presented in section 5.3.3, since in this process, the

two charged leptons emerge from the same vector boson and distributions which involve a neutrino cannot be reconstructed experimentally.

Cross sections

Table 5.4 gives some cross sections and the corresponding Monte Carlo integration errors for this process.

Process and parameters	Cross section [fb]	Error [fb]
SM, without spin-2	0.1540	$2.2658 \cdot 10^{-4}$
Spin-2 singlet, without formfactor	0.3999	$1.3388 \cdot 10^{-3}$
Spin-2 singlet, with formfactor	0.1636	$1.6674 \cdot 10^{-3}$

Table 5.4: Total cross sections and errors for process 211

Invariant mass distribution of the four final state leptons

Fig. 5.66 and 5.67 exemplify the invariant mass distribution of the four final state leptons for a spin-2 singlet resonance at 1 TeV. As in process 210, the spin-2 Feynman diagrams lead to unphysical high-energy contributions, which can be suppressed by the formfactor. Triplet resonances and resonances at other masses can be obtained analogously.

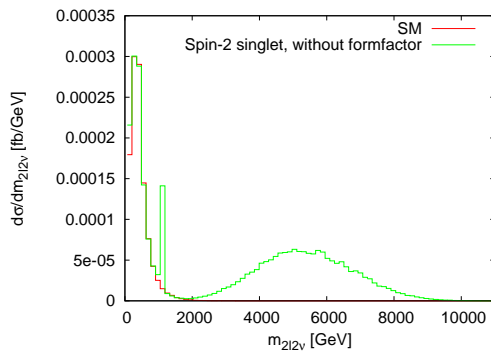


Figure 5.66: Invariant mass distribution of the four final state leptons for process 211, without formfactor

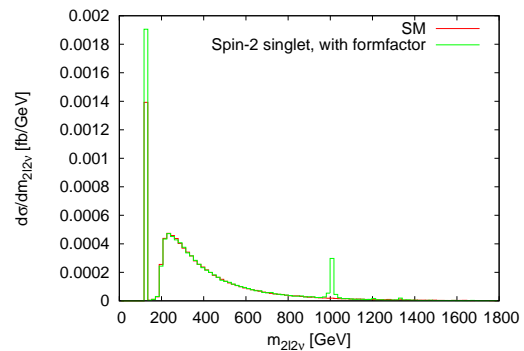


Figure 5.67: Invariant mass distribution of the four final state leptons for process 211, with formfactor

5.4.2 Process 200: $pp \rightarrow VV jj \rightarrow e^+ \nu_e \mu^- \bar{\nu}_\mu jj$

For the analysis of this process, the settings are the same as for process 210, except for the value of Λ . It is chosen as $\Lambda = 1$ TeV in the singlet case and $\Lambda = 300$ GeV in the triplet case, since otherwise, the spin-2 triplet resonance of fig. 5.69 would not be visible.

Cross sections

Table 5.5 gives some cross sections and the corresponding errors for the process 200.

Process and parameters	Cross section [fb]	Error [fb]
SM, without spin-2	1.6235	$1.9977 \cdot 10^{-3}$
Spin-2 singlet, without formfactor	6.8977	$1.6023 \cdot 10^{-2}$
Spin-2 singlet, with formfactor	1.6739	$5.7615 \cdot 10^{-3}$
Spin-2 triplet, with formfactor	1.6507	$6.6604 \cdot 10^{-3}$

Table 5.5: Total cross sections and errors for process 200

Invariant mass distribution of the four final state leptons

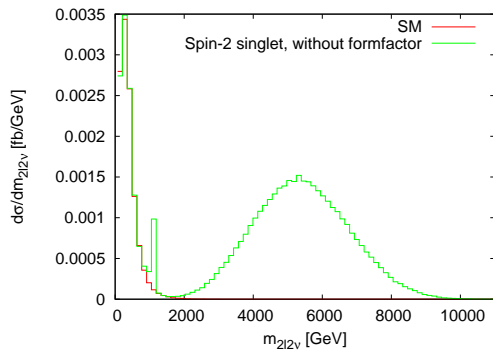


Figure 5.68: Invariant mass distribution of the four final state leptons for process 200, without formfactor

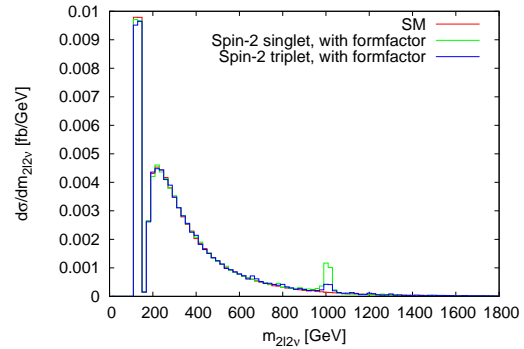


Figure 5.69: Invariant mass distribution of the four final state leptons for process 200, with formfactor, singlet and triplet resonance

From fig. 5.68, it can be seen that the high-energy contributions are larger than for all the other considered processes. Nevertheless, they can be suppressed completely by using the formfactor with the usual parameter settings.

Although Λ was chosen as 300 GeV for the triplet resonance, this resonance (fig. 5.69) is very small in comparison to the one of process 210, where Λ was 1.5 TeV. This can be understood by looking at the spin-2 triplet Feynman rules (see chapter 3.2.2): The uncharged triplet particle couples to two W bosons only via the f_6 term, whereas the Feynman rules for vertices involving photons and Z bosons contain the coupling f_7 .

Angular distributions

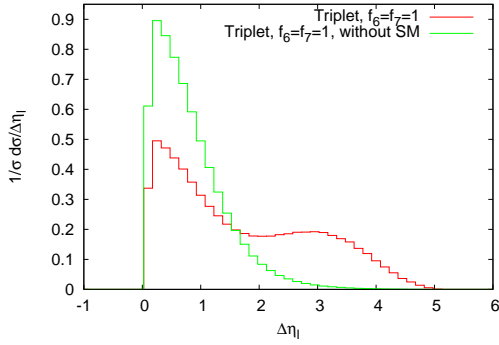


Figure 5.70: $\Delta\eta_l$, spin-2 triplet,
 $f_6 = f_7 = 1, f_{i \neq 6,7} = 0$

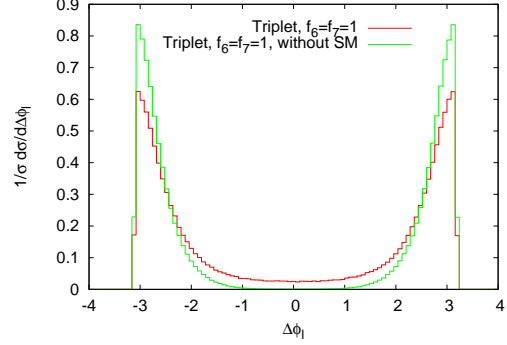


Figure 5.71: $\Delta\Phi_l$, spin-2 triplet,
 $f_6 = f_7 = 1, f_{i \neq 6,7} = 0$

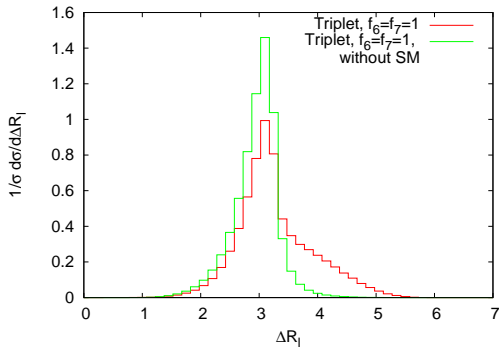


Figure 5.72: ΔR_l , spin-2 triplet,
 $f_6 = f_7 = 1, f_{i \neq 6,7} = 0$

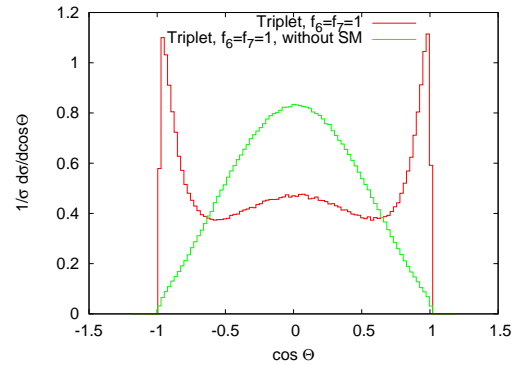


Figure 5.73: $\cos \Theta$, spin-2 triplet,
 $f_6 = f_7 = 1, f_{i \neq 6,7} = 0$

This specific feature of the Feynman rules also affects the angular distributions. For the singlet parameter settings $f_1 = f_2 = f_5 = 1, f_{i \neq 1,2,5} = 0$ and

$f_5 = 1, f_{i \neq 5} = 0$, the distributions look similar to those of process 210 and also the triplet setting $f_6 = 1, f_{i \neq 6} = 0$ yields the same distributions as $f_5 = 1, f_{i \neq 5} = 0$.

However, the situation is different for the triplet setting $f_6 = f_7 = 1, f_{i \neq 6,7} = 0$, since the Feynman rules of the coupling to the initial vector bosons, which involve Z bosons and photons, contain f_6 and f_7 terms, whereas the coupling to the final W bosons only contains f_6 . While the p_T distributions resemble the ones for $f_1 = f_2 = f_5 = 1, f_{i \neq 1,2,5} = 0$ and the $\Delta\Phi_{jj}$ distribution looks as usual, the angular distributions of the final state leptons (fig. 5.70, 5.71 and 5.72) and the $\cos\Theta$ distribution (fig. 5.73) are different. Note that in contrast to process 210, there is only one sensible possibility to combine final state leptons which do not emerge from the same vector boson, as the other ones would involve neutrinos.

Although these distributions differ from those corresponding to other parameter settings, there is little chance that their characteristics will be useful for a distinction between the spin-2 singlet and triplet case. They are obscured by the SM background even for very large coupling parameters (or low values of Λ , respectively) and strong cuts on the invariant lepton mass, which is illustrated by the red lines of fig. 5.70-5.73. For the settings $\Lambda = 300$ GeV, MLEP_MIN= 950 GeV and MLEP_MAX= 1050 (corresponding width: 25.11 GeV), which were applied for the distributions of fig. 5.70-5.73, the SM background contributes roughly 50 % to the distributions.

Nevertheless, this process provides a possibility to distinguish between the singlet and triplet case for certain parameter settings on the basis of the invariant mass distribution: Due to the small coupling of a neutral spin-2 triplet particle to two W bosons only via f_6 , a spin-2 resonance has to be a triplet resonance, if it is clearly observable in the processes 210 and 211, but very small or not detectable in process 200.

5.4.3 Process 220: $pp \rightarrow VV jj \rightarrow e^+ \nu_e \mu^+ \mu^- jj$ **and**
process 230: $pp \rightarrow VV jj \rightarrow e^- \bar{\nu}_e \mu^+ \mu^- jj$

For the analysis of the processes 220 and 230, the settings are the same as for process 210, except for the value of Λ , which is chosen as $\Lambda = 1$ TeV.

Cross sections

The tables 5.6 and 5.7 give some cross sections and the corresponding errors for the processes 220 and 230.

Process and parameters	Cross section [fb]	Error [fb]
SM, without spin-2	0.1728	$2.4422 \cdot 10^{-4}$
Spin-2 singlet, without formfactor	0.2801	$5.6476 \cdot 10^{-4}$
Spin-2 triplet, without formfactor	0.1993	$3.3130 \cdot 10^{-4}$
Spin-2 triplet, with formfactor	0.1748	$2.4535 \cdot 10^{-4}$

Table 5.6: Total cross sections and errors for process 220

Process and parameters	Cross section [fb]	Error [fb]
SM, without spin-2	0.0947	$1.1288 \cdot 10^{-4}$
Spin-2 triplet, without formfactor	0.1025	$1.4985 \cdot 10^{-4}$
Spin-2 triplet, with formfactor	0.0959	$1.3079 \cdot 10^{-4}$

Table 5.7: Total cross sections and errors for process 230

From table 5.6 and 5.7, it is noticeable that the cross sections of process 220 are roughly twice as high as the ones of process 230. This difference stems from the PDFs and is associated with the fact that the three valence quarks of a proton consist of two u quarks and one d quark. Apart from that, the two processes have exactly the same features, since their Feynman diagrams are completely analogous.

Invariant mass distribution of the four final state leptons

From fig. 5.74, 5.75 and 5.76, one can see that only the triplet case leads to a resonance, whereas for the singlet case, there are the usual high-energy contributions, if no formfactor is applied, but no resonance.

This reflects a general feature of the processes 220 and 230: For these processes, only charged resonances are possible. Therefore, a charged spin-2 triplet particle leads to a resonance in these processes, whereas the singlet case can only produce a neutral resonance. This can also be seen from the Feynman diagrams of section 4.4.

For the same reason, there is no Higgs resonance for these processes.

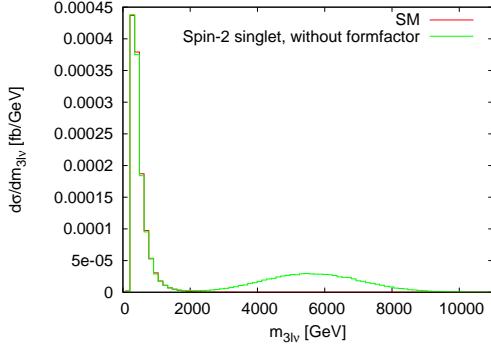


Figure 5.74: Invariant mass distribution of the four final state leptons for process 220, $\Lambda = 1$ TeV, without formfactor, singlet

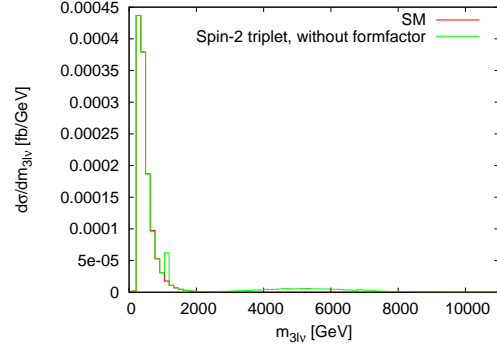


Figure 5.75: Invariant mass distribution of the four final state leptons for process 220, $\Lambda = 1$ TeV, without formfactor, triplet

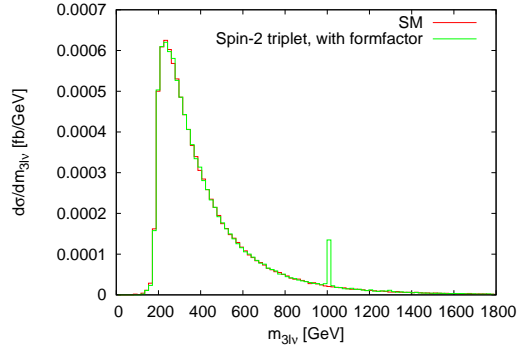


Figure 5.76: Invariant mass distribution of the four final state leptons for process 220, $\Lambda = 1$ TeV, with formfactor, triplet resonance

This feature provides a simple, but powerful tool to distinguish between the spin-2 singlet and triplet case. Regardless of the parameter settings, a spin-2 resonance in the processes $pp \rightarrow VV jj \rightarrow e^+ \nu_e \mu^+ \mu^- jj$ (220) and $pp \rightarrow VV jj \rightarrow e^- \bar{\nu}_e \mu^+ \mu^- jj$ (230) can only be a triplet resonance.

5.4.4 Summary of heavy Spin-2 resonances in VBF processes with four leptons in the final state

The implementation of the present spin-2 model into VBF processes with four leptons in the final state does not only yield spin-2 resonances, but

also unphysical high-energy contributions due to unitarity violation. These contributions can be suppressed by using the formfactor with appropriate parameters.

Heavy spin-2 resonances cause specific transverse momentum and angular distributions, which are similar for the different kinds of processes discussed in section 5.3 and 5.4. Since for the chosen parameters, the spin-2 resonances contribute little to the total cross-sections, these distributions are dominated by the SM background if only inclusive and vbf cuts are applied. Therefore, additional cuts on the invariant mass of the final state lepton system are needed. With these cuts, it is possible to reveal the characteristic distributions of a spin-2 resonance. For most of the parameter settings, the distributions are not affected very much by the SM background. Only for $f_5 = 1, f_{i \neq 5} = 0$ (and the analogous triplet setting $f_6 = 1, f_{i \neq 6} = 0$), they are obscured significantly. However, they can still be distinguished from the distributions of the SM background and from other parameter settings due to their specific features.

Most of the hadronic observables are hardly affected by spin-2 resonances. However, the azimuthal angle difference between the two jets, $\Delta\Phi_{jj}$, shows a characteristic difference between the spin-2 resonance and the SM background, but it is hardly sensitive to different spin-2 coupling parameters. The p_T distribution of the jet with the largest transverse momentum only changes significantly for $f_5 = 1, f_{i \neq 5} = 0$. The distributions of the final state leptons are more suitable. The p_T distribution of the lepton with the largest transverse momentum is modified by a spin-2 resonance such that higher values of $p_{T,max,l}$ are preferred. The angular distributions of the leptons, $\Delta\eta_l, \Delta\Phi_l$ and ΔR_l , also present characteristic features of a spin-2 resonance. The same is true for the $\cos\Theta$ distribution.

Based on the processes 210 and 211, which are dominated by $ZZjj$ production, the spin-2 singlet and triplet scenario cannot be distinguished, as both cases yield the same characteristics. Process 200, which corresponds to W^+W^-jj production, can be useful for such a determination for specific parameter settings due to the different Feynman rules of the coupling of a spin-2 singlet and triplet particle to two W bosons.

However, the most important tools to distinguish between the singlet and triplet case are the processes 220 and 230, which are dominated by $W^\pm Zjj$ production. Since only charged resonances are possible for these processes, only the spin-2 triplet leads to a spin-2 resonance in this case.

6 Summary

The recent start of the LHC provides the chance both for the detection of the Higgs boson, which is the only particle of the Standard Model which has not been observed yet, and the discovery of some manifestations of physics beyond the Standard Model in the form of new, heavy resonances. For both of these scenarios, vector boson fusion processes are important possible detection channels.

For the detection of the Higgs, it is important to verify its spin, which has to be zero. In the photon pair-production VBF process, which is one of the most interesting channels for the detection of the Higgs, the spin of a resonance can also be 2, but not 1 due to the Landau-Yang theorem. Therefore, one of the main goals of this thesis was the distinction of a spin-0 and a spin-2 resonance in this channel.

The other one was the investigation of heavy spin-2 resonances in processes with different four-lepton final states, namely $e^+ e^- \mu^+ \mu^-$, $e^+ e^- \nu_\mu \bar{\nu}_\mu$, $e^+ \nu_e \mu^- \bar{\nu}_\mu$, $e^+ \nu_e \mu^+ \mu^-$ and $e^- \bar{\nu}_e \mu^+ \mu^-$.

In both cases, especially angular correlations were studied in great detail, since they are known as an important tool for the analysis of the spin of resonances.

For these studies, a model of spin-2 particles, which can only interact with electroweak bosons, was developed. This was done for two different cases: a spin-2 state which behaves as a singlet under SU(2) transformations and a spin-2 triplet in the adjoint representation.

To this end, an effective ansatz was used to construct Lagrangians both for the singlet and the triplet scenario. Each of the terms contains the spin-2 field, a dimensionless, variable coupling parameter, which is divided by the new-physics energy scale, and an operator which contains either two electroweak field strength tensors (or the corresponding dual field strength tensors) or a covariant derivative acting on the Higgs field and the hermitian conjugate of this. Thereby, the number of possible operators was limited by several constraints like Gauge and Lorentz invariance.

The particle content of these spin-2 models comprises one neutral spin-2 singlet particle (called T) and three triplet particles, namely one pair of charged particles and one neutral particle (denoted as T^+ , T^- and T^0).

From the singlet and triplet Lagrangian, the corresponding Feynman rules were calculated. Although they consist of 17 vertices in the singlet case and 38 in the triplet case, only few of them were needed for the following analysis. The relevant vertices for the singlet and the neutral triplet particle are the same, namely $T^{(0)}W^+W^-$, $T^{(0)}ZZ$, $T^{(0)}\gamma\gamma$ and $T^{(0)}\gamma Z$. For the charged triplet

particles, the relevant vertices are $T^\pm W^\mp Z$ and $T^\pm W^\mp \gamma$. The Feynman rules of all these vertices involve the same Lorentz structure, which consists of three rank-4 tensors.

In order to analyze the effects of the present spin-2 model in electroweak boson fusion processes, the model was implemented into the Monte Carlo program VBFNLO, which simulates vector boson fusion processes at next-to-leading order in the strong coupling constant. The general procedure of a VBFNLO calculation was illustrated and the implementation of the spin-2 model into VBFNLO was presented.

Then, the results of the analysis of spin-2 resonances were illustrated. First, unitarity constraints were investigated on the basis of longitudinal WW scattering. Since the present spin-2 model is based on an effective ansatz, which is a low-energy approximation and can only be used up to a certain energy scale, the amplitudes increase with the centre of mass energy, which leads to unitarity violation above a certain scale. However, a possibility to evade unitarity violation was found as well: The introduction of a formfactor, whose parameters can be chosen such that unitarity is preserved.

Afterwards, light, Higgs-like spin-2 resonances in the photon pair-production VBF process were investigated. The results of this analysis indicate that it is possible to distinguish between a Higgs and a spin-2 resonance in this process, while the detailed features of a spin-2 resonance depend on their parameters. The cross-section can be similar for a Higgs and a spin-2 resonance if the spin-2 coupling parameters are tuned in an appropriate way. The transverse momentum distributions are different unless a formfactor with adjusted parameters is applied.

Angular distributions are the most important tool for a distinction between the Higgs and the spin-2 scenario. Especially the $\Delta\Phi_{jj}$ and the $\cos\Theta$ distribution are clearly different for a Higgs resonance and spin-2 resonance with a formfactor. This difference is illustrated nicely by a double differential plot which combines both distributions.

Without the formfactor, these differences are less evident, but in this case, the differences in the transverse momentum distributions can be used as an additional tool to distinguish between a Higgs and a spin-2 resonance.

For all the considered distributions, the spin-2 singlet and triplet case are similar, since their Feynman diagrams are nearly the same for the photon pair-production process.

Therefore, this process is not useful for a distinction between a spin-2 singlet and a spin-2 triplet resonance.

Finally, the features of heavy spin-2 resonances in the different processes with four leptons in the final state were presented. Thereby, the process $pp \rightarrow VV jj \rightarrow e^+ e^- \mu^+ \mu^- jj$ has been studied in most detail, since a resonance in the invariant mass distribution of the final state leptons can be reconstructed exactly if no neutrinos are involved. However, the features of the other processes with four leptons in the final state are mainly analogous.

The implementation of the spin-2 model into all these processes does not only yield spin-2 resonances, but also unphysical high-energy contributions resulting from unitarity violation, which can be suppressed by using the formfactor.

Heavy spin-2 resonances lead to specific features in the transverse momentum and angular distributions, which are observable despite the presence of the Standard Model background, if appropriate cuts are applied. The most important distributions are $\cos \Theta$, $\Delta\Phi_{jj}$, the p_T distribution of the lepton with the largest transverse momentum and the angular correlations of the final state leptons $\Delta\eta_l$, $\Delta\Phi_l$ and ΔR_l .

Based on the processes $pp \rightarrow VV jj \rightarrow e^+ e^- \mu^+ \mu^- jj$ and $pp \rightarrow VV jj \rightarrow e^+ e^- \nu_\mu \bar{\nu}_\mu jj$, the spin-2 singlet and triplet scenario cannot be distinguished, as both cases yield the same characteristics. The process $pp \rightarrow VV jj \rightarrow e^+ \nu_e \mu^- \bar{\nu}_\mu jj$ can be useful for such a determination for specific parameter settings due to the different Feynman rules of the coupling of a spin-2 singlet and triplet particle to two W bosons.

For the processes $pp \rightarrow VV jj \rightarrow e^+ \nu_e \mu^+ \mu^- jj$ and $pp \rightarrow VV jj \rightarrow e^- \bar{\nu}_e \mu^+ \mu^- jj$, only charged resonances are possible. Therefore, only the spin-2 triplet leads to a spin-2 resonance. Since this feature does not depend on any of the spin-2 parameters, it provides a both simple and powerful tool to distinguish between the spin-2 singlet and triplet case.

Appendix

A Spin-2 field and propagator

A.1 Spin-2 field

The general form of a spin-2 singlet field is:

$$T^{\mu\nu}(x) = \int \frac{d^3k}{(2\pi)^3 2k^0} \sum_{\lambda=-2}^2 \epsilon^{\mu\nu}(k, \lambda) a_{\lambda}(k) e^{-ikx} + \epsilon^{*\mu\nu}(k, \lambda) a_{\lambda}^{\dagger}(k) e^{ikx} \quad (\text{A.1})$$

and the general form of a spin-2 triplet field is:

$$T_j^{\mu\nu}(x) = \int \frac{d^3k}{(2\pi)^3 2k^0} \sum_{\lambda=-2}^2 \epsilon^{\mu\nu}(k, \lambda) a_{\lambda,j}(k) e^{-ikx} + \epsilon^{*\mu\nu}(k, \lambda) a_{\lambda,j}^{\dagger}(k) e^{ikx} \quad (\text{A.2})$$

a and a^{\dagger} are annihilation and creation operators and $\epsilon^{\mu\nu}$ is the polarization tensor of the spin-2 field [15]:

$$\begin{aligned} \epsilon^{\mu\nu}(k, \pm 2) &= \epsilon^{\mu}(k, \pm) \epsilon^{\nu}(k, \pm) \\ \epsilon^{\mu\nu}(k, \pm 1) &= \frac{1}{\sqrt{2}} (\epsilon^{\mu}(k, \pm) \epsilon^{\nu}(k, 0) + \epsilon^{\mu}(k, 0) \epsilon^{\nu}(k, \pm)) \\ \epsilon^{\mu\nu}(k, 0) &= \frac{1}{\sqrt{6}} (\epsilon^{\mu}(k, +) \epsilon^{\nu}(k, -) + \epsilon^{\mu}(k, -) \epsilon^{\nu}(k, +) + 2\epsilon^{\mu}(k, 0) \epsilon^{\nu}(k, 0)) \end{aligned} \quad (\text{A.3})$$

The polarization vectors ϵ^μ are the usual ones of vector bosons and can be written explicitly as [21]:

$$\begin{aligned}
\epsilon^\mu(k, 1) &= \frac{1}{|\vec{k}|k_T} (0, k_x k_z, k_y k_z, -k_T^2)^T, \\
\epsilon^\mu(k, 2) &= \frac{1}{k_T} (0, -k_y, k_x, 0)^T, \\
\epsilon^\mu(k, 3) &= \frac{E}{m|\vec{k}|} \left(\frac{|\vec{k}|^2}{E}, k_x, k_y, k_z \right)^T \\
&\quad \left(m = \sqrt{E^2 - |\vec{k}|^2}, \quad k_T = \sqrt{k_x^2 + k_y^2} \right)
\end{aligned} \tag{A.4}$$

with

$$\begin{aligned}
\epsilon^\mu(k, \pm) &= \frac{1}{\sqrt{2}} (\mp \epsilon^\mu(k, 1) - i \epsilon^\mu(k, 2)) \\
\epsilon^\mu(k, 0) &= \epsilon^\mu(k, 3)
\end{aligned} \tag{A.5}$$

A.2 Spin-2 propagator

As the propagator is the Greens function of the free field equations, it is independent of the interaction Lagrangian and therefore it is the same as in other theories ([15],[30]):

$$\frac{iB^{\mu\nu\alpha\beta}}{k^2 - m_T^2 + im_T\Gamma_T} \tag{A.6}$$

where m_T is the mass of the spin-2 particle, k is its momentum, Γ_T is its width and

$$\begin{aligned}
B^{\mu\nu\alpha\beta}(k) &= \frac{1}{2} (g^{\mu\alpha} g^{\nu\beta} + g^{\mu\beta} g^{\nu\alpha} - g^{\mu\nu} g^{\alpha\beta}) \\
&\quad - \frac{1}{2m_T^2} (g^{\mu\alpha} k^\nu k^\beta + g^{\nu\beta} k^\mu k^\alpha + g^{\mu\beta} k^\nu k^\alpha + g^{\nu\alpha} k^\mu k^\beta) \\
&\quad + \frac{1}{6} \left(g^{\mu\nu} + \frac{2}{m_T^2} k^\mu k^\nu \right) \left(g^{\alpha\beta} + \frac{2}{m_T^2} k^\alpha k^\beta \right)
\end{aligned} \tag{A.7}$$

B Decay widths of the Spin-2 singlet and triplet particles

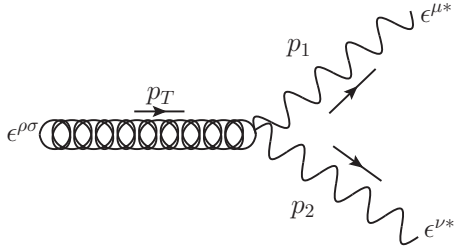
B.1 Singlet

For the calculation of the total decay width of the spin-2 singlet particle, the following formula, which is calculated from a formula taken from [31], is used:

$$\Gamma_{total} = \sum_j \Gamma_j, \quad \Gamma_j = \frac{|\vec{p}|}{8\pi m_T^2} |\mathcal{M}|^2 \quad (\text{B.1})$$

where m_T is the mass of the spin-2 singlet particle (which is called *sp2mass* in VBFNLO) and the sum runs over all possible decay channels.

The matrix element \mathcal{M} corresponds to the following diagram, with a spin-2 particle at rest decaying into two electroweak bosons:



$$i\mathcal{M} = \epsilon^{\mu*}(p_1) \epsilon^{\nu*}(p_2) V_{\mu\nu\rho\sigma} \epsilon^{\rho\sigma}(p_T) \quad (\text{B.2})$$

$V_{\mu\nu\rho\sigma}$ represents the Feynman rules of the corresponding vertex, which can be TW^+W^- , TZZ , $T\gamma\gamma$ or $T\gamma Z$.

If the direction of the decay products is defined as the z-axis, energy-momentum-conservation reads:

$$p_T = p_1 + p_2 \iff \begin{pmatrix} m_T \\ 0 \\ 0 \\ 0 \end{pmatrix} = \begin{pmatrix} \sqrt{p^2 + m_{v1}^2} \\ 0 \\ 0 \\ p \end{pmatrix} + \begin{pmatrix} \sqrt{p^2 + m_{v2}^2} \\ 0 \\ 0 \\ -p \end{pmatrix} \quad (\text{B.3})$$

This yields a $|\vec{p}|$ which is different for the different decay channels W^+W^-/ZZ , γZ and $\gamma\gamma$.

From eq. (B.2), $|\mathcal{M}|^2$ can be calculated by using the following replacements:

$$\text{Photon: } \sum_{\lambda} \epsilon^{\mu*}(q, \lambda) \epsilon^{\nu}(q, \lambda) \rightarrow -g^{\mu\nu} \quad (\text{B.4})$$

$$W, Z: \sum_{\lambda} \epsilon^{\mu*}(q, \lambda) \epsilon^{\nu}(q, \lambda) \rightarrow -g^{\mu\nu} + \frac{q^{\mu}q^{\nu}}{m^2} \quad (\text{B.5})$$

$$\text{Spin-2 particle: } \sum_{\lambda=-2}^2 \epsilon^{\mu\nu}(p, \lambda) \epsilon^{*\alpha\beta}(p, \lambda) \rightarrow B^{\mu\nu\alpha\beta}(p) \quad (\text{B.6})$$

where $B^{\mu\nu\alpha\beta}(p)$ has been given in eq. (A.7).

(B.4) and (B.5) are taken from [31] and (B.6) is taken from [15].

$$\Rightarrow |\mathcal{M}|^2 = \frac{1}{5} V_{\mu\nu\rho\sigma} V_{\lambda\kappa\gamma\delta}^* B^{\rho\sigma\gamma\delta}(p_T) (-\hat{g}^{\mu\lambda}) (-\hat{g}^{\nu\kappa}) \quad (\text{B.7})$$

with $\hat{g}^{\mu\lambda} = g^{\mu\lambda}$ for a photon and $\hat{g}^{\mu\lambda} = g^{\mu\lambda} - \frac{p_i^{\mu} p_i^{\lambda}}{m_{vi}^2}$ ($i = 1$ or 2) for a W or Z boson.

For the decay modes ZZ and $\gamma\gamma$, there is an additional symmetry factor $\frac{1}{2}$ due to the identical particles.

The explicit results for Γ_j are:

$$\Gamma_{W^+W^-} = \left(\frac{24f_2^2(m_T^4 - 3m_T^2m_W^2 + 6m_W^4) + 40f_2f_5g^2v^2(m_T^2 - m_W^2)}{12\Lambda^2} + \frac{f_5^2g^4v^4(m_T^4 + 12m_T^2m_W^2 + 56m_W^4)}{96\Lambda^2m_W^4} \right) * \frac{\sqrt{(m_T^2/4 - m_W^2)}}{(40\pi m_T^2)} \quad (\text{B.8})$$

$$\Gamma_{ZZ} = \left([24f_2^2c_w^4(m_T^4 - 3m_T^2m_Z^2 + 6m_Z^4) + 8c_w^2f_2(6f_1s_w^2(m_T^4 - 3m_T^2m_Z^2 + 6m_Z^4) + 5f_5v^2(g^2 + g'^2)(m_T^2 - m_Z^2)) + 24f_1^2s_w^4(m_T^4 - 3m_T^2m_Z^2 + 6m_Z^4) + 40f_1f_5s_w^2v^2(g^2 + g'^2)(m_T^2 - m_Z^2)] / (12\Lambda^2) + \frac{f_5^2v^4(g^2 + g'^2)^2(m_T^4 + 12m_T^2m_Z^2 + 56m_Z^4)}{96\Lambda^2m_Z^4} \right) * \frac{\sqrt{m_T^2/4 - m_Z^2}}{80\pi m_T^2} \quad (\text{B.9})$$

$$\Gamma_{\gamma\gamma} = \frac{(f_1c_w^2 + f_2s_w^2)^2m_T^3}{80\pi\Lambda^2} \quad (\text{B.10})$$

$$\Gamma_{\gamma Z} = \frac{c_w^2s_w^2(f_1 - f_2)^2(m_T^2 - m_Z^2)^3(6m_T^4 + 3m_T^2m_Z^2 + m_Z^4)}{240\pi\Lambda^2m_T^7} \quad (\text{B.11})$$

Note that all these widths only contain the parameters f_1 , f_2 and f_5 , but not f_3 and f_4 . This means that the corresponding terms in the Lagrangian (3.2) do not lead to spin-2 resonances (see section 5.3.2, fig. 5.41).

To get the total decay width, one has to sum over all of the widths (B.8) - (B.11) where the mass of the spin-2 particle is larger than the sum of the final state particle masses.

There is the possibility of further decay channels beyond the effective theory considered in this thesis, leading to a larger total width. Therefore, an additional parameter, called *brrat*, is introduced, which is the fraction of decays into electroweak bosons over all possible decays.

This parameter has to be greater than zero and less than or equal to one; where the last one signifies that no additional decay modes exist.

This yields

$$\Gamma_{total} = (\Gamma_{W+W^-} + \Gamma_{ZZ} + \Gamma_{\gamma\gamma} + \Gamma_{\gamma Z}) * \frac{1}{brrat} \quad (B.12)$$

Due to the possibility of modifying the parameter *brrat*, the width of a spin-2 resonance can be varied. This could provide a useful tool to achieve an agreement between the present model and a future experimental analysis.

B.2 Triplet

For the decay width of the spin-2 triplet particles, the same basic equations (B.1 - B.7) hold. However, as the Feynman rules are different, of course $V_{\mu\nu\rho\sigma}$ (eq. B.2 and B.7) is different. Also the mass m_T does not have to be the same as in the singlet case. For the neutral triplet particle, it is called *msp2tripn* and for the charged particle *msp2trippm* in VBFNLO.

For the neutral particle, the results for Γ_j are:

$$\Gamma_{W^+W^-} = \frac{f_6^2 g^4 v^4 (m_T^4 + 12m_T^2 m_W^2 + 56m_W^4)}{384\Lambda^2 m_W^4} * \frac{\sqrt{m_T^2/4 - m_W^2}}{40\pi m_T^2} \quad (\text{B.13})$$

$$\begin{aligned} \Gamma_{ZZ} = & \left((768f_7^2 c_w^2 s_w^2 m_Z^4 (m_T^4 - 3m_T^2 m_Z^2 + 6m_Z^4) + 640c_w f_6 f_7 m_Z^4 s_w v^2 \right. \\ & \left. (g^2 + g'^2)(m_T^2 - m_Z^2) + f_6^2 v^4 (g^2 + g'^2)^2 (m_T^4 + 12m_T^2 m_Z^2 + 56m_Z^4) \right) \\ & / (384\Lambda^2 m_Z^4) * \frac{\sqrt{m_T^2/4 - m_Z^2}}{80\pi m_T^2} \end{aligned} \quad (\text{B.14})$$

$$\Gamma_{\gamma\gamma} = \frac{f_7^2 c_w^2 s_w^2 m_T^3}{80\pi\Lambda^2} \quad (\text{B.15})$$

$$\Gamma_{\gamma Z} = \frac{f_7^2 (c_w^2 - s_w^2)^2 (m_T^2 - m_Z^2)^3 (6m_T^4 + 3m_T^2 m_Z^2 + m_Z^4)}{960\pi\Lambda^2 m_T^7} \quad (\text{B.16})$$

The widths for the charged particles are:

$$\Gamma_{W\gamma} = \frac{f_7^2 c_w^2 (m_T^2 - m_W^2)^3 (6m_T^4 + 3m_T^2 m_W^2 + m_W^4)}{960\pi\Lambda^2 m_T^7} \quad (\text{B.17})$$

$$\begin{aligned} \Gamma_{WZ} = & \left((m_T^2 m_W^2 (m_T^2 m_Z^2 (13f_6^2 g^2 v^4 (g^2 + g'^2) + 256f_7^2 m_W^2 m_Z^2 s_w^2) \right. \\ & + 1/4(m_T^2 - m_W^2 + m_Z^2)^2 (7f_6^2 g^2 v^4 (g^2 + g'^2) - 96f_7^2 m_W^2 m_Z^2 s_w^2)) \\ & + 1/4(m_T^2 + m_W^2 - m_Z^2)^2 (m_T^2 m_Z^2 (7f_6^2 g^2 v^4 (g^2 + g'^2) - 96f_7^2 m_W^2 m_Z^2 s_w^2) \\ & + (m_T^2 - m_W^2 + m_Z^2)^2 (f_6^2 g^2 v^4 (g^2 + g'^2) + 32f_7^2 m_W^2 m_Z^2 s_w^2)) \\ & + m_T^2 (m_T^2 - m_W^2 - m_Z^2) (1/4(m_T^2 + m_W^2 - m_Z^2) (m_T^2 - m_W^2 + m_Z^2) \\ & (128f_7^2 m_W^2 m_Z^2 s_w^2 - f_6^2 g^2 v^4 (g^2 + g'^2)) + 40f_6 f_7 g m_T^2 m_W^2 m_Z^2 s_w v^2 \sqrt{g^2 + g'^2}) \\ & + 1/4m_T^4 (-m_T^2 + m_W^2 + m_Z^2)^2 (f_6^2 g^2 v^4 (g^2 + g'^2) + 32f_7^2 m_W^2 m_Z^2 s_w^2) \\ & + 40f_6 f_7 g m_T^2 m_W^2 m_Z^2 s_w v^2 \sqrt{g^2 + g'^2} (m_T^2 + m_W^2 - m_Z^2) \\ & \left. (m_T^2 - m_W^2 + m_Z^2) \right) / (96\Lambda^2 m_T^4 m_W^2 m_Z^2) \\ & * \frac{\sqrt{(m_T^2 - m_W^2 - m_Z^2)^2 - 4m_W^2 m_Z^2}}{80\pi m_T^3} \end{aligned} \quad (\text{B.18})$$

As in the singlet case, a decay channel can only contribute to the total width if the mass of the spin-2 particle is large enough to produce the final vector bosons. Whereas the neutral spin-2 particles (singlet and triplet) can always decay into two photons, a charged spin-2 particle can only decay if its mass is larger than the mass of the W. Lighter spin-2 particles are not considered within

this thesis, as these are difficult to achieve with current experimental constraints.

For the triplet, branching ratios are introduced as additional parameters as well, for the same reason. They can be different from the singlet case and from each other. For the neutral triplet particle, it is called *brattripn* in VBFNLO and for the charged particle *brattripm*.

C Some VBFNLO files

C.1 vbfno.dat

The following text is the content of the file vbfno.dat.

Further information about the chosen parameters can be found in section 4.5.1.

```

! Main input file for vbfno
!
! General parameters of the calculation
!-----
PROCESS          = 220          ! Identifier for process
LOPROCESS_PLUS_JET = false      ! switch: LO process with 1 additional jet
LEPTONS          = 12 -11 13 -13 ! final state leptons

! lepton numbering according to MC particle numbering scheme
! particles are given positive numbers, antiparticles negative numbers
! e-  ve  mu-  vm  ta-  vt
! 11  12  13  14  15  16

LO_ITERATIONS    = 4          ! number of iterations for LO calculation
NLO_ITERATIONS   = 4          ! number of iterations for real-emissions calc.
LO_POINTS        = 22         ! number of points for LO calculation (= 2^..)
NLO_POINTS       = 22         ! number of points for real-emissions calc. (= 2^..)
LO_GRID          = "grid2_1" "grid2_2" "grid2_3" ! names of gridfiles for LO calculation
NLO_GRID         = "grid3_1" "grid3_2" "grid3_3" ! names of gridfiles for real emissions calculation
NLO_SWITCH       = false      ! switch: nlo/lo calculation

ECM              = 14000d0    ! collider center-of-mass energy
BEAM1            = 1          ! type of beam 1 (1=proton, -1= antiproton)
BEAM2            = 1          ! type of beam 2 (1=proton, -1= antiproton)

ID_MUF           = 1          ! ID for factorization scale
ID_MUR           = 1          ! ID for renormalization scale
MUF_USER         = 100d0     ! user defined factorization scale, if MUF is set to 0
MUR_USER         = 100d0     ! user defined renormalization scale, if MUR is set to 0
XIF              = 1d0       ! scale factor xi for mu_F (not mu^2!!)
XIR              = 1d0       ! scale factor xi for mu_R

! Physics parameters
!-----
HMASS            = 120.0d0    ! Higgs mass
TOPMASS          = 173.3d0    ! Top mass
BOTTOMMASS       = 4.67d0     ! Bottom Pole mass
CHARMMASS        = 1.27d0     ! Charm Pole mass
ALFA_S           = 0.1184d0   ! Strong coupling constant
EWScheme         = 3          ! Choose scheme for electroweak parameters (1,2,3,4)
FERMI_CONST      = 1.16637d-5 ! Fermi Constant
ALFA             = 7.2973525376d-3 ! Fine-structure constant
SIN2W            = 0.23116d0   ! Weak mixing angle
WMASS           = 80.399d0    ! W mass
ZMASS           = 91.1876d0   ! Z mass
ANOM_CPL         = false      ! Anomalous couplings
KK_MOD           = false      ! Warped Higgsless Model
SPIN2            = true       ! spin2 couplings

```

```

! Parameters for the LHA event output
|-----
LHA_SWITCH      = true      ! Les Houches interface only for LO calculation
UNWEIGHTING_SWITCH = false   ! unweighted/weighted (T/F) events for LHA
PRENEVUNW      = 1000     ! number of events to calculate pre-maximal weight
TAUMASS        = false     ! Include mass of the tau lepton(s) in the LHA file for VBF processes

! PDF set parameters
|-----
PDF_SWITCH      = 0        ! which pdfs to use: 1 = lhpdf, 0 = hard-wired cteq (default)
! choose pdfset and pdfmember here. Look at the LHAPDF manual for details.
LO_PDFSET       = 10042    ! cteq6ll.LHpdf
NLO_PDFSET      = 10000    ! cteq6.LHpdf
LO_PDFMEMBER    = 0
NLO_PDFMEMBER   = 0

! Parameters for histogram creation
|-----
ROOT            = false    ! create root-file?
TOP             = false    ! create top-drawer file?
GNU            = true     ! create gnu-plot script file?
DATA           = true     ! create data file?
REPLACE        = true     ! replace output files?
ROOTFILE       = histograms ! name of root-file ( + '.root' )
TOPFILE        = histograms ! name of top-drawer file ( + '.top' )
GNUFILE        = histograms ! name of gnuplot file ( + '.gp' )
DATAFILE       = histograms ! name of data directory ( + '.dir' )

```

C.2 cuts.dat

The following text is the content of the file cuts.dat.

For detailed information about the chosen cuts, see section 4.5.2.

```

! input file for the cut parameters

! Jet cuts
|-----
RJJ_MIN        = 0.7d0     ! min jet-jet R separation
Y_P_MAX        = 5.0d0     ! max pseudorapidity for partons
PT_JET_MIN     = 30.0d0    ! min jet pT
Y_JET_MAX      = 4.5d0     ! max jet rapidity

! Lepton cuts (only applied to charged leptons)
|-----
Y_L_MAX        = 2.5d0     ! max lepton rapidity
PT_L_MIN       = 20.0d0    ! min lepton pT
MLL_MIN        = 15.0d0    ! min. ml+l for any comb. of opposite charged leptons
RLL_MIN        = 0.0d0     ! min lepton-lepton R separation
RLL_MAX        = 50.0d0    ! max lepton-lepton R separation

! additional lepton (and neutrino) cuts
|-----
PT_V_MIN       = 0.0d0     ! minimum neutrino pt (only for ZZjj_lnu, WPZjj, WMZjj)
MT_MIN         = 0.0d0     ! minimal transverse mass (only for ZZjj_lnu, WPZjj, WMZjj)
MZZ_MIN        = 0.0d0     ! minimal invariant 4 lepton mass (only for ZZjj_ll)
PTLL_MIN       = 0.0d0     ! minimal pt of 2 leptons (only for ZZjj_ll)
PTDIFF_MIN     = 0.0d0     ! minimal pt difference of 2 lep (only for WPWMjj)
MLJ_MIN        = 0.0d0     ! minimal invariant mass of a jet and a lepton (only for WPWMjj)

MLEP_MIN       = 0.0d0     ! minimal invariant lepton (and neutrino) mass
MLEP_MAX       = 14000.0d0 ! maximal invariant lepton (and neutrino) mass

```



```

! Photon cuts
!-----
Y_G.MAX      = 2.5d0
PT_G.MIN     = 20.0d0
RGG_MIN      = 0.4d0      ! min photon-photon R separation
RGG_MAX      = 50.0d0     ! max photon-photon R separation
PHISOLCUT    = 0.7d0     ! photon isolation cut
EFISOLCUT    = 1d0       ! efficiency of photon isolation cut

! Additional R-separation cuts
!-----
RJL_MIN      = 0.4d0     ! min jet-lepton R separation
RJG_MIN      = 0.4d0     ! min jet-photon R separation
RLG_MIN      = 0.0d0     ! min lepton-photon R separation

! Vector boson fusion cuts (only applied to tagging jets in VBF processes)
!-----
ETAJJ_MIN    = 0.0d0     ! jet-jet rapidity separation
YSIGN        = false     ! jets #1 and #2 must have opposite sign rapidity
LRAPIDGAP    = false     ! leptons fall inside rapidity gap
DELY_JL      = 0.0d0     ! min y-dist of leptons from tagging jets
GRAPIDGAP    = false     ! photons fall inside rapidity gap
DELY_JG      = 0.0d0     ! min y-dist of photons from tagging jets

MDIJ_MIN     = 0.0d0     ! dijet min mass cut on tag jet
MDIJ_MAX     = 14000.0d0 ! dijet max mass cut on tag jet

JVETO        = false     ! veto jet cuts
DELY_JVETO   = 0.0d0     ! min veto-tag y-dist
YMAX_VETO    = 4.5d0     ! max |y| for veto jet
PTMIN_VETO   = 25.0d0    ! min pT for veto jet

```

C.3 spin2coupl.dat

The following text is the content of the file spin2coupl.dat:

```

!! Parameters for Spin 2 theory

! Singlet couplings

f1           = 0.0d0
f2           = 0.0d0
f3           = 0.0d0
f4           = 0.0d0
f5           = 0.0d0

! Triplet couplings

f6           = 2.0d0
f7           = 1.0d0

lambda       = 1.0d3      ! energy scale of couplings (singlet and triplet) in GeV

! masses (in GeV)

```

```

sp2mass    = 1.2d2    ! mass of a spin 2 singlet particle
msp2trippm = 1.2d2    ! mass of a (pos. or neg.) charged spin 2 triplet particle
msp2tripn  = 1.2d2    ! mass of a neutral spin 2 triplet particle

! branching ratios for the widths, 0.2 <= brrat <= 1.0
!(Spin 2 particles could decay into particles which are not considered here)

brrat      = 1.0d0    ! branching ratio for sp2width (singlet width)
brrattrippm = 1.0d0    ! branching ratio for sp2trippmwidth (charged triplet width)
brrattripn  = 1.0d0    ! branching ratio for sp2tripnwidth (neutral triplet width)

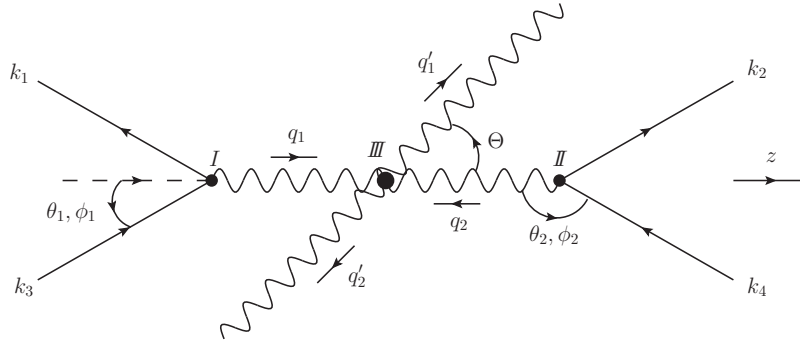
! parameters of the formfactor

nff        = 2.0d0    ! exponent of formfactor
lambdaff   = 4.0d2    ! energy scale of formfactor (in GeV)

```

D Relevant frames and transformations

This section presents the different frames which are used for the present analysis. Apart from the laboratory frame, three other frames are very useful: The Breit frames of the two initial vector bosons and the rest frame of the spin-2 particle (or the Higgs). They are shown in the following figure:



In the Breit frames of the initial vector bosons, the momenta and angles are parametrized as follows:

(I): q_1 Breit frame:

$$\begin{aligned}
q_1^\mu &= k_3^\mu - k_1^\mu = (0, 0, 0, Q_1) \\
k_1^\mu &= \frac{Q_1}{2 \cos \theta_1} (1, \sin \theta_1 \cos \phi_1, \sin \theta_1 \sin \phi_1, -\cos \theta_1) \\
k_3^\mu &= \frac{Q_1}{2 \cos \theta_1} (1, \sin \theta_1 \cos \phi_1, \sin \theta_1 \sin \phi_1, \cos \theta_1)
\end{aligned} \tag{D.1}$$

where $Q_1 = \sqrt{-q_1^2}$, $0 < \theta_1 < \pi/2$, $-\pi < \phi_1 < \pi$

(II): q_2 Breit frame:

$$\begin{aligned} q_2^\mu &= k_4^\mu - k_2^\mu = (0, 0, 0, -Q_2) \\ k_2^\mu &= \frac{-Q_2}{2 \cos \theta_2} (1, \sin \theta_2 \cos \phi_2, \sin \theta_2 \sin \phi_2, -\cos \theta_2) \\ k_4^\mu &= \frac{-Q_2}{2 \cos \theta_2} (1, \sin \theta_2 \cos \phi_2, \sin \theta_2 \sin \phi_2, \cos \theta_2) \end{aligned} \quad (\text{D.2})$$

where $Q_2 = \sqrt{-q_2^2}$, $\pi/2 < \theta_2 < \pi$, $-\pi < \phi_2 < \pi$

This parametrization follows the conventions of [27], but one difference should be noted: The numeration of the parton momenta is changed: $k_1 \leftrightarrow k_3$ and $k_2 \leftrightarrow k_4$, following the numeration of VBFNLO.

The transformation from the laboratory frame into the q_1 Breit frame is performed in the following way:

First, q_1 is rotated to the z-axis, in order to obtain zero in the first two momentum components.

The angle α of this rotation is given by the angle between q_1 and the z-axis:

$$\alpha = \arccos(q_{1,z}/|\vec{q}_1|) \quad (\text{D.3})$$

The axis \vec{a} of the rotation is defined by the normalized cross product of q_1 and the z-axis:

$$\vec{a} = \begin{pmatrix} q_{1,y} \\ -q_{1,x} \\ 0 \end{pmatrix} \cdot \frac{1}{\sqrt{q_{1,x}^2 + q_{1,y}^2}} \quad (\text{D.4})$$

The matrix for the rotation by the angle α about the axis \vec{a} is given by:

$$R = \begin{pmatrix} \cos \alpha + a_x^2(1 - \cos \alpha) & a_x a_y(1 - \cos \alpha) - a_z \sin \alpha & a_x a_z(1 - \cos \alpha) + a_y \sin \alpha \\ a_x a_y(1 - \cos \alpha) + a_z \sin \alpha & \cos \alpha + a_y^2(1 - \cos \alpha) & a_z a_y(1 - \cos \alpha) - a_x \sin \alpha \\ a_x a_z(1 - \cos \alpha) - a_y \sin \alpha & a_z a_y(1 - \cos \alpha) + a_x \sin \alpha & \cos \alpha + a_z^2(1 - \cos \alpha) \end{pmatrix} \quad (\text{D.5})$$

The rotated four-vector is:

$$\begin{aligned} q_{1,rot}^0 &= q_1^0 \\ \vec{q}_{1,rot} &= R \cdot \vec{q}_1 \end{aligned} \quad (\text{D.6})$$

Afterwards, a Lorentz boost along the z-axis is performed with the VBFNLO routine **boostn**, in order to obtain a zero in the energy component. The reference vector for this boost is:

$$r^\mu = (1, 0, 0, -q_{1,rot}^0/q_{1,rot}^z) \quad (\text{D.7})$$

The same transformations are applied to k_1 and k_3 .

For the transformation from the laboratory frame into the q_2 Breit frame, an analogous procedure is performed for q_2 , k_2 and k_4 , but the z-axis needs to be replaced by the negative z-axis.

In the rest frame of the spin-2 particle (or the Higgs), frame (III), the momenta of the outgoing vector bosons, q'_1 and q'_2 , have opposite directions, as well as q_1 and q_2 .

The transformation from the laboratory frame to this frame is implemented by using a Lorentz boost with the reference vector

$$r^\mu = (P^0, -P^1, -P^2, -P^3), \quad (\text{D.8})$$

where $P^\mu = q_{1,lab}^\mu + q_{2,lab}^\mu$.

The angle Θ is defined as the angle between q_1 and q'_1 in frame (III).

E Wigner d-functions

The following formulae are taken from [22] and [25].

The Wigner d-functions $d_{m,m'}^j$ are related to the spherical harmonics Y_j^m by

$$d_{m,0}^j = \sqrt{\frac{4\pi}{2l+1}} Y_j^m e^{-im\phi}. \quad (\text{E.1})$$

Up to $j = 2$, the explicit forms of the d-functions are

$$d_{0,0}^0 = 1$$

$$d_{0,0}^1 = \cos \theta$$

$$d_{1,1}^1 = \frac{1+\cos \theta}{2}$$

$$d_{1,0}^1 = -\frac{\sin \theta}{\sqrt{2}}$$

$$d_{1,-1}^1 = \frac{1-\cos \theta}{2}$$

$$d_{2,2}^2 = \left(\frac{1+\cos \theta}{2}\right)^2$$

$$d_{2,1}^2 = -\frac{1+\cos \theta}{2} \sin \theta$$

$$d_{2,0}^2 = \frac{\sqrt{6}}{4} \sin^2 \theta$$

$$d_{2,-1}^2 = -\frac{1-\cos \theta}{2} \sin \theta$$

$$d_{2,-2}^2 = \left(\frac{1-\cos \theta}{2}\right)^2$$

$$d_{1,1}^2 = \frac{1+\cos \theta}{2} (2\cos \theta - 1) \quad d_{1,0}^2 = -\sqrt{\frac{3}{2}} \sin \theta \cos \theta \quad d_{1,-1}^2 = \frac{1-\cos \theta}{2} (2\cos \theta + 1)$$

$$d_{0,0}^2 = \frac{3}{2} \cos^2 \theta - \frac{1}{2}$$

Other combinations of m, m' can be obtained from:

$$d_{m',m}^j = (-1)^{m-m'} d_{m,m'}^j = d_{-m,-m'}^j \quad (\text{E.2})$$

The d-functions obey the following orthogonality relation:

$$\int_0^\pi d_{m,m'}^j(\theta) d_{m,m'}^{j'}(\theta) \sin \theta d\theta = \delta_{jj'} \frac{2}{2j+1} \quad (\text{E.3})$$

Bibliography

- [1] S. L. Glashow, J. Iliopoulos, L. Maiani: "Weak Interactions with Lepton-Hadron Symmetry", Phys. Rev. D 2 (1970) no. 7, 1285-1292
- [2] A. Salam: "Weak and Electromagnetic Interactions", Almqvist and Forlag, Stockholm, 1968
- [3] S. Weinberg: "A Model of Leptons", Phys. Rev. Lett. 19 (1967) no. 21, 1264-1266
- [4] P. W. Higgs: "Broken symmetries, massless particles and gauge fields", Physics Letters 12 (1964) no. 2, 132-133
- [5] P. W. Higgs: "Broken Symmetries and the Masses of Gauge Bosons", Phys. Rev. Lett. 13 (1964), 508-509
- [6] L. D. Landau, Dokl. Akad. Nauk., USSR 60, 207 (1948); C. N. Yang, Phys. Rev. 77, 242 (1950)
- [7] C. Englert: "Spin 1 Resonances in Vector Boson Fusion in Warped Higgsless Models"
- [8] K. Arnold, M. Bähr, G. Bozzi, F. Campanario, C. Englert, T. Figy, N. Greiner, C. Hackstein, V. Hankele, B. Jäger, G. Klämke, M. Kubocz, C. Oleari, S. Plätzer, S. Prestel, M. Worek, D. Zeppenfeld: "VBFNLO: A parton level Monte Carlo for processes with electroweak bosons", arXiv:0811.4559 [hep-ph]
- [9] D. J. Gross, F. Wilczek: "Ultraviolet Behavior of Non-abelian Gauge Theories", Phys. Rev. Lett. 30 (1973), 1343-1346
- [10] H. D. Politzer: "Reliable Perturbative Results for Strong Interactions?", Phys. Rev. Lett 30 (1973), 1346-1349
- [11] D. Zeppenfeld: "Higgs Physics at the LHC", Third Graduate School in Physics at Colliders, Turin, January 7-11, 2008 (www.to.infn.it/~maina/scuola08/Zepfenfeld_Torino08.pdf)
- [12] M. Steinhauser: "Übungen zu Strahlungskorrekturen in Eichtheorien", Herbstschule für Hochenergiephysik, Maria Laach 2003 (<http://maria-laach.physik.uni-siegen.de/2003/Folien/Steinhauser/laach2003.ps.gz>)
- [13] C. Burgess, G. Moore: "The Standard Model: A Primer"

- [14] W. Buchmüller, D. Wyler: "Effective Lagrangian Analysis of New Interactions and Flavour Conservation", Nucl. Phys. B268 (1986) 621
- [15] K. Hagiwara, J. Kanzaki, Q. Li, K. Mawatari: "HELAS and MadGraph/MadEvent with Spin-2 particles", arXiv:0805.2554v1 [hep-ph]
- [16] N. D. Christensen, C. Duhr: "FeynRules - Feynman rules made easy", Comput. Phys. Commun. 180 (2009), 1614-1641, arXiv:0806.4194 [hep-ph]
- [17] A. Semenov: "LanHEP - a package for the automatic generation of Feynman rules in field theory. Version 3.0", Comput. Phys. Commun. 180 (2009), 431-454, arXiv:0805.0555 [hep-ph]
- [18] D. Zeppenfeld: "Collider Physics", arXiv:hep-ph/9902307v1
- [19] S. Weinzierl: "Introduction to Monte Carlo methods", arXiv:hep-ph/0006269v1
- [20] G. Lepage: "VEGAS: An Adaptive Multi-dimensional Integration Program", CLNS 80-447, 1980
- [21] K. Hagiwara, J. Kanzaki, H. Murayama, I. Watanabe: "HELAS: HELicity Amplitude Subroutines for Feynman diagram evaluations"
- [22] Particle Data Group: "Review of Particle Physics" (http://pdg.lbl.gov/2010/html/computer_read.html)
- [23] J. Pumplin, D. R. Stump, J. Huston, H. L. Lai, P. Nadolsky, W. K. Tung: "New generation of parton distributions with uncertainties from global QCD analysis", arXiv:hep-ph/0201195
- [24] C. Englert, B. Jäger, M. Worek, D. Zeppenfeld: "Observing Strongly Interacting Vector Boson Systems at the CERN Large Hadron Collider", arXiv:0810.4861v2 [hep-ph]
- [25] M. Jakob, G. C. Wick: "On the General Theory of Collisions for Particles with Spin", Ann. Phys. 7 (1959) 404-428
- [26] B. Feigl: "Anomale Vier-Vektorboson-Kopplungen bei der Produktion von drei Vektorbosonen am LHC" (<http://www-itp.particle.uni-karlsruhe.de/diplomatheses.de.shtml>)
- [27] K. Hagiwara, Q. Li, K. Mawatari: "Jet angular correlation in vector-boson fusion processes at hadron colliders", arXiv:0905.4314v2 [hep-ph]

- [28] A. Heister, O. Kodolova, V. Konoplyanikov, S. Petrushanko, J. Rohlf, C. Tully, A. Ulyanov, CERN-CMS-NOTE-2006-036
- [29] T. Figy, D. Zeppenfeld: "QCD Corrections to Jet Correlations in Weak Boson Fusion", arXiv:hep-ph/0403297v1
- [30] G. F. Giudice, R. Rattazzi, J. D. Wells: "Quantum Gravity and Extra Dimensions at High-Energy Colliders", arXiv:hep-ph/9811291v2
- [31] M. E. Peskin, D. V. Schröder: "An Introduction to Quantum Field Theory"

Danksagung

Zunächst danke ich Herrn Prof. Zeppenfeld für die gute Betreuung, die interessante Themenstellung, die Korrekturvorschläge für diese Arbeit und die Bereitschaft, mich als externe Diplomandin zu betreuen.

Bei Herrn Prof. Wunner möchte ich mich für die Übernahme des Koreferats bedanken.

Mein besonderer Dank gilt Dr. Michael Rauch für die Mitbetreuung und das Korrekturlesen meiner Arbeit und dafür, dass er sich immer sehr viel Zeit für die kompetente Beantwortung all meiner Fragen genommen hat.

Allen Institutsangehörigen danke ich für die freundliche Atmosphäre und für interessante Diskussionen, bei denen ich viel lernen konnte. Insbesondere möchte ich meinen Mitdiplomanden für ihre Hilfsbereitschaft und das Beantworten zahlloser technischer Fragen danken.

Herrn Prof. Giessen danke ich dafür, dass er mich ermutigt hat, mir eine externe Diplomarbeit zu suchen, was mir den letzten entscheidenden Anstoß dazu gab.

Meinen Eltern danke ich für ihre Unterstützung während meines Studiums, auch finanzieller Art.

Der Studienstiftung des deutschen Volkes danke ich für mein Stipendium.

Bei Heike und Sönke Nanz möchte ich mich dafür bedanken, dass ich bei ihnen wohnen durfte.

Zu guter Letzt danke ich Sven für seine Liebe und Unterstützung.